QUANTIFICATION OF RESPIRATORY MOTION IN POSITRON EMISSION TOMOGRAPHY FOR PRECISE RADIATION TREATMENT OF LUNG CANCER

QUANTIFICATION OF RESPIRATORY MOTION IN POSITRON EMISSION TOMOGRAPHY FOR PRECISE RADIATION TREATMENT OF LUNG CANCER

BY

CHAD TURNER, B.Sc.

A Thesis Submitted to the Radiation Sciences Graduate Program
and the School of Graduate Studies
of McMaster University
in Partial Fulfillment of the Requirements
for the Degree of
Master of Science

Master of Science (2021) McMaster University

(Radiation Sciences – Medical Physics) Hamilton, Ontario, Canada

TITLE:	Quantification of Respiratory Motion in Positron Emission Tomography for Precise Radiation Treatment of Lung Cancer
AUTHOR:	Chad Turner, B.Sc. (Honours)
	University of Prince Edward Island
SUPERVISOR:	Dr. Roxana Vlad
CO-SUPERVISOR:	Dr. Troy Farncombe
NUMBER OF PAGES:	xiv, 103

Abstract

A well-established method for treating lung cancer is curative-intent radiation therapy (RT). The most significant challenge for RT is to accurately target the lesion volume while avoiding the irradiation of surrounding healthy tissue. Currently at the Juravinski Cancer Centre (JCC), treatment plans for lung cancer patients are completed using fluorodeoxyglucose positron emission tomography (FDG-PET) and four-dimensional computed tomography (4DCT) images. There is no clear protocol, however, to compensate for respiratory motion in PET images and it is not known how lesion volumes generated from PET reflect the true volume. This project evaluated methods to optimize the use of PET images in the radiation treatment planning workflow and quantify the effects of respiratory motion. First, a 4D XCAT digital phantom was used to quantify respiratory motion and its effects on lesion displacement. A CTN physical phantom and 3D-printed irregularly shaped lesion were imaged to determine the accuracy of the PET EDGE automated segmentation algorithm (ASA). Lastly, rigid and deformable image registration techniques were used to propagate the diagnostic PET scan of the irregular lesion to the 4D planning CT. PET EDGE was used to generate target volumes which were then compared to internal target volumes (ITVs) generated from manual contouring of the 4DCT image alone.

We found that lesion displacement due to respiratory motion can be adequately modeled using a moving platform set to oscillate 1 cm and 2 cm for normal and deep breathing, respectively. Optimal target delineation was found when diagnostic PET was propagated to the planning CT using rigid image registration for lesions that experienced 1 cm of oscillatory motion during imaging. In contrast, PET EDGE would overestimate volumes in static cases and underestimate volumes in instances of 2 cm dynamic motion meant to simulate deep breathing.

Acknowledgements

First and foremost, I must thank Dr. Roxana Vlad for your supervision throughout this project. Despite the challenges of completing so much of this research remotely, I always felt supported and confident that we would continue to make progress. Your insight, guidance, and commitment to both my success and the success of our work has been invaluable.

I would like to thank Dr. Troy Farncombe for co-supervising my research, sharing your expertise in PET, and using your logistical skills to coordinate an experiment. Additionally, I must thank Dr. Marcin Wierzbicki for both your work on my committee and your excellent teaching – 778 was truly a fantastic class. To all the technicians at JCC and SJHH, thank you for making my experiments possible and for helping with kindness and enthusiasm.

A big thank you must be extended to the faculty, staff, and students in the Department of Physics and Astronomy. Coming from a small university, it was wonderful to feel the same close-knit atmosphere here at McMaster. I am immensely grateful for this experience.

Paul and Janice, you created a home-away-from-home and treated me like one of your own. My appreciation for you both is boundless. To my friends here at McMaster, thank you for the memories and help along the way, let's stay in touch. Finally, thank you to my friends and family back home for your endless support. The COVID-19 pandemic kept us separated for over a year, yet our relationships never wavered. I can't wait to make up for that lost time together.

Table of Contents

List of Figures

List of Tables

List of Abbreviations

JCC	Juravinski Cancer Centre
SJHH	St. Joseph's Healthcare Hamilton
RT	Radiation Therapy
PET	Positron Emission Tomography
CT	Computed Tomography
FDG	Fluorodeoxyglucose
MIP	Maximum Intensity Projection
NSCLC	Non-Small Cell Lung Cancer
GTV	Gross Tumor Volume
CTV	Clinical Target Volume
ITV	Internal Target Volume
PTV	Planning Target Volume
ASA	Automated Segmentation Algorithm
XCAT	Extended Cardiac-Torso Phantom
CTN	Clinical Trials Network
RIR	Rigid Image Registration
DIR	Deformable Image Registration
DSC	Dice Similarity Coefficient

1 Introduction

1.1 Non-Small Cell Lung Cancer

1.1.1 Statistics and Prognosis

Lung cancer is the second-most diagnosed and deadliest cancer in Canada, with an estimated 29,800 new cases and 21,200 deaths in 2020 alone.[1] These figures represent 13% of the expected 225,800 newly-diagnosed cancer cases and 25.5% of the 83,300 projected cancer deaths in Canada. As the leading cause of death amongst both sexes, lung cancer accounts for 25% of cancer deaths in males and 26% of cancer deaths in females. Although incidence and mortality rates have decreased since the 1990's, lung cancer is still responsible for more deaths than the next three leading causes combined, with colorectal, pancreatic, and breast cancer deaths totaling 20,100.[2]

The prognosis associated with a lung cancer diagnosis is often poor compared to other cancer types. The 5-year net survival rate for lung cancer in Canada is approximately 19% at a confidence interval of 95%.[3] This means that at the time of diagnosis, 19% of patients will survive for at least 5 years. Using the less-common 1-year and 10-year survival rates, lung cancer survival stands at 44% and 13%, respectively.[3] Excluding mesothelioma as it is a cancer of the lung due to asbestos exposure, only esophageal and pancreatic cancers have a lower 5-year survival rate than lung cancer, with rates of 8% and 15%, respectively.[3]

Of the two cancer types, non-small cell (NSCLC) and small-cell lung cancer (SCLC), NSCLC accounts for approximately 9 in 10 lung cancer cases. The statistics presented above describe lung cancer overall.

The choice and effectiveness of a given treatment is reliant on the type of tumor and its progression at diagnosis. Furthermore, understanding of the biology of the disease is paramount, as is the subsequent staging procedure that can be used to assess the optimal treatment for a given patient.

1.1.2 Biology, Risk Factors and Staging

In Canada, 72% of lung cancer cases are linked to tobacco smoke, and 86% of cases are deemed preventable. With cigarette smoking being the leading contributor, other risk factors include second hand smoke, air pollution, occupational exposure to crystalline silica and chrysotile asbestos, radon exposure, poor diet, and genetic markers such as *TP53*.[4] As previously mentioned, the two types of lung cancer are non-small cell lung cancer (NSCLC) and small cell lung cancer (SCLC). Non-small cell lung cancer can be further divided into lung squamous cell carcinoma and lung adenocarcinoma.[5] These subtypes are differentiated based on the origin of the cancer: lung squamous cell carcinoma begins in the flat, thin cells that line the bronchi and are known as squamous cells, whereas lung adenocarcinoma usually starts in the glandular cells on the outer part of the lung. Unfortunately, lung cancer patients typically present with advanced disease which leads to poor prognosis and contributes to the low 5-year survival rate.[5]

Staging of lung cancer is completed using the TNM system, where T represents the size of the tumor, N represents the involvement of lymph nodes, and M describes metastasis, or spreading of the tumor from the primary disease site.[4] The tumor will be classified and staged based on each descriptor combined. Table 1.1 shows a general form of the proposed eighth edition of the TNM Classification for Lung Cancer by the IASLC.[6]

TNM Descriptor		**Description**
T1	T1a(mi)	Minimally invasive adenocarcinoma
	T1a	Tumor ≤ 1cm
	T1b	Tumor > 1cm but ≤ 2 cm
	T1c	Tumor > 2 cm but ≤ 3 cm
T2*	T2a	Tumor > 3cm but ≤ 4 cm
	T2b	Tumor > 4 cm but ≤ 5 cm
T3**		Tumor > 5 cm but ≤ 7 cm
T4***		Tumor > 7 cm

N0		No regional lymph node metastasis
N1		Metastasis in ipsilateral peribronchial and/or ipsilateral hilar lymph nodes and intrapulmonary nodes
N2		Metastasis in ipsilateral mediastinal and/or subcarinal lymph node(s)
N3		Metastasis in contralateral mediastinal, contralateral hilar, ipsilateral or contralateral scalene, or supraclavicular lymph node(s)
M0		No distant metastasis
M1	M1a	Separate tumor nodular(s) in contralateral lobe; tumor with pleural or pericardial nodule(s) or malignant pleural or pericardial effusion
	M1b	Single extrathoracic metastasis
	M1c	Multiple extrathoracic metastasis in ≥ 1 organ

Table 1.1 TNM classification parameters of lung cancer by the IASLC.[6] *T2 classification can also include invasion of visceral pleura, associated with atelectasis or obstructive pneumonitis that extends to hilar region, or involvement of main bronchus without involment of the carnia. **T3 classification can also include tumor nodules in same lobe as primary tumor or invasion of the chest wall, phrenic nerve, or parietal pericardium. ***T4 can also include tumor nodule in separate ipsilateral lobe than primary tumor, or invasion of the diaphragm, mediastinum, heart, great vessels, trachea, recurrent laryngeal nerve, esophagus, vetebral body, and carnia

Using the description of the tumor offered by the TNM classification system, the overall stage of the disease is then presented in roman numerals from stage I to stage IV. Stage IV is the most progressed stage of the disease and is often characterized by metastases within or outside the thoracic cavity. A detailed anatomy of the thoracic cavity is shown in Figure 1.1.[7]

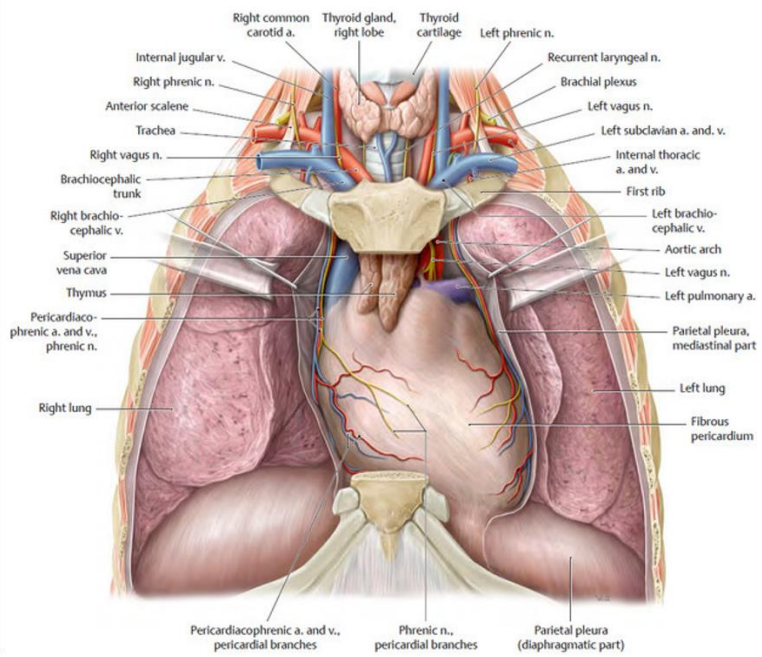

Figure 1.1 Diagram of thoracic cavity.[7]

The most common diagnostic tool that leads to confirmation of NSCLC and the subsequent stage of the disease is fibreoptic bronchoscopy.[8] This procedure uses a thin fibreoptic tube that is passed into the lungs through the nose or mouth of a patient, allowing for the physician to inspect the suspected tumor site. In addition to this procedure, lymph nodes near to the primary disease site are often viewed and evaluated through endobronchial ultrasound (EBUS) or endoscopic ultrasound (EUS). The combination of these diagnostic procedures are usually able to confirm a diagnosis of NSCLC, however it cannot always classify whether it is lung squamous cell carcinoma or lung adenocarcinoma.[8]

Staging can also be completed using positron emission tomography (PET) and computed tomography (CT) imaging.[4] PET involves the injection of the positron emitting source 18-fluorodeoxyglucose (18-FDG) into the patient prior to imaging. This radioactive sugar is up-taken by metabolically active areas to provide functional information at the cellular level. CT is poor at observing microscopic disease spread, however it provides vastly superior resolution and anatomical detail than PET. These two

imaging modalities are often combined into one procedure using a hybrid PET/CT system, thereby combining the functional information provided by PET with the anatomical information provided by CT. The generation of these images can result in changes to any initial staging or treatment plans, and pathology findings with PET can be confirmed through biopsies of the lesion.[4]

Assessment of the mediastinal region is vital to determining the stage and best treatment option for a lung cancer patient.[9] The mediastinum is a section of the thoracic cavity outside of the lungs that contains the heart, thymus gland, parts of the esophagus and trachea, as well as numerous nerves, vessels, and lymph nodes. Presence of tumor in this region indicates an

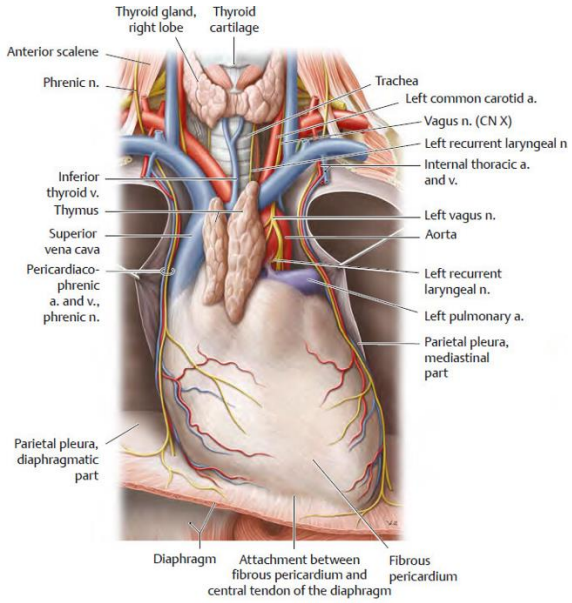

Figure 1.2 Diagram of the mediastinum[7]

increase in likelihood of lung cancer advancing from stage I to the upper stages. Noninvasively, mediastinal lymph node involvement is best distinguished using PET as opposed to CT or MRI.[10] Figure 1.3, for example, demonstrates a case of PET uncovering a cancerous node that was not distinguishable on CT.[11]

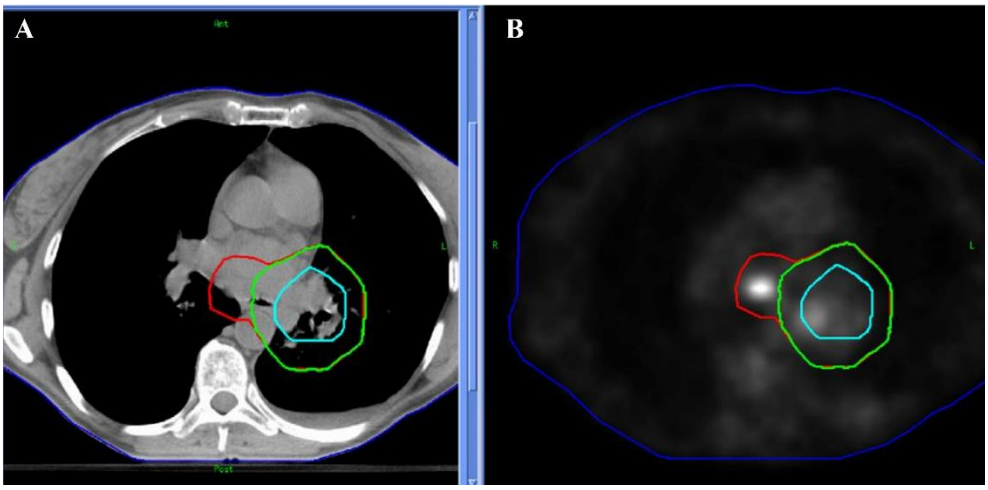

Figure 1.3 Image showing A) CT and B) PET images of a NSCLC treatment plan. Original PTV drawn on CT shown in green contour, with red contour showing extension of PTV after PET showed involvement of a paraesophageal lymph node in the mediastinum.[11]

The usefulness of a medical imaging modality is commonly evaluated by its sensitivity and specificity, where the sensitivity is the true positive rate and the specificity is the true negative rate.[12] The sensitivity and specificity for PET in determining mediastinal lymph node metastasis in lung cancer are 80% and 88%, respectively. This is an improvement over the respective 55% and 81% sensitivity and specificity of CT alone. Using a PET/CT image results in a sensitivity and specificity of 62% and 90%, respectively.[9] Despite the advantages of noninvasive staging, invasive methods are often used to confirm PET/CT findings. The most common invasive technique for mediastinal lymph node staging in lung cancer is cervical mediastinoscopy. This same-day discharge procedure is done under general anesthesia and has a sensitivity and specificity of 78% and 100%, respectively. Newer techniques such as the previously mentioned EBUS and EUS are less invasive and provide more access to regions-of-interest (ROIs) than cervical mediastinoscopy. Both techniques have sensitivity and specificity values of 89% and 100%, respectively.

1.1.3 Treatment

Standard treatment options for non-small cell lung cancer include surgical resection, radiation therapy, chemotherapy, and targeted therapy. For stage I and stage II NSCLC,

surgical resection has been shown to have the highest 5-year survival rates – 60-80% for stage I and 30-50% for stage 2 - following treatment when compared to other modalities. Therefore, for early-stage NSCLC this is the accepted treatment when the tumor is operable.[13] After resection, adjuvant chemotherapy has been shown to be effective with stage II, but not stage I NSCLC patients. Adjuvant radiation therapy is not recommended for early-stage patients who have underwent surgical resection.[14] In the event a patient declines to undergo surgery or is deemed inoperable due to the staging or location of a tumor, curative intent radiation therapy is the primary treatment modality.[13]

Approximately 30% of new NSCLC patients are diagnosed with stage III cancer.[15] Within this advanced stage, treatment options vary depending on the location and operability of the tumor. For resectable stage IIIA NSCLC, the standard treatment is surgery and adjuvant chemotherapy. If there is lymph node involvement, radiation therapy can follow surgical resection with beneficial outcomes.[15] Cancers of this stage that are not surgically operable are often treated with a combination of chemotherapy and radiation therapy, commonly referred to as chemoradiation. Chemoradiation with platinum-based chemotherapy drugs such as cisplatin have been shown to be particularly effective when compared to radiation alone.[15,16] The 5-year survival rate for stage IIIB NSCLC is roughly 26%,[6] and treatment options are based on the patient's performance status and the site of the tumor.[15] Chemotherapy or radiation therapy are the primary treatments, as surgery is not always effective on its own. For curative-intent chemoradiation, a radiation dose of 60-66 Gy is recommended.[17] Patients with a poor prognosis may receive palliative radiation therapy to improve quality of life.[15]

Although not curable, stage IV NSCLC can be treated with both chemotherapy and radiation therapy.[18] Patients with a good performance score, an indicator for their prognosis, are recommended to receive a platinum-based chemotherapy, with the possible addition of a second chemotherapeutic agent, to provide both a survival advantage and to improve quality of life.[18] If the prognosis of the patient is poor, palliative chemotherapy or palliative radiation therapy are used.

Radiation therapy is used across all stages of NSCLC treatment. In stages I and II, it is the primary treatment for patients who cannot or will not undergo surgical resection. For operable stage III cancers, radiation therapy is often used after surgery if there is lymph node involvement. Curative intent radiation therapy or chemoradiation can also be used as primary treatments if the effectiveness of surgery is limited or if the cancer is inoperable. Patients with stage IV NSCLC may receive a combination of chemotherapy and radiation therapy to improve quality of life or for palliative care.

1.2 Radiation Therapy

Radiation therapy is a cancer treatment modality that uses high energy photons or particles such as electrons to eliminate cancer cells effectively and efficiently. Curative, or radical, radiation treatment is delivered with the intent to eliminate an entire tumor volume, whereas palliative radiation treatment is administered to provide pain relief to patients during end-of-life care. The most significant challenge for radiation therapy is to attain the highest probability of cure with the least morbidity, which can only be achieved by precisely targeting the disease and avoiding the irradiation of surrounding healthy tissue.

1.2.1 Radiation Physics – Photon Production

Conventional radiotherapy uses x-rays to kill cells through indirect ionization. These x-rays are generated in a medical linear accelerator, often abbreviated as LINAC. Here, thermionic emission of electrons is first completed through heating of a metal cathode. These electrons then travel along microwaves through an accelerating waveguide where they gain speeds approaching the speed of light, *c*, before being steered onto a heavy-metal x-ray target such as tungsten. As the electrons strike the metal target, electromagnetic interactions with the positive atomic nucleus causes them to decelerate, creating Bremsstrahlung radiation in the form of x-rays. Since the degree of interaction between electrons and positively charged nuclei varies, x-rays leaving the target exist at a spectrum of energies with the maximum x-ray energy equal to the energy of the incident electrons. Typical energies used for conventional radiation are 6, 10, or 18 MV. After

leaving the metal target, x-rays are passed through a conical flattening filter to uniformly distribute the intensity of the beam prior to shaping with collimators. A block diagram of a LINAC is shown in Figure 1.4.[19]

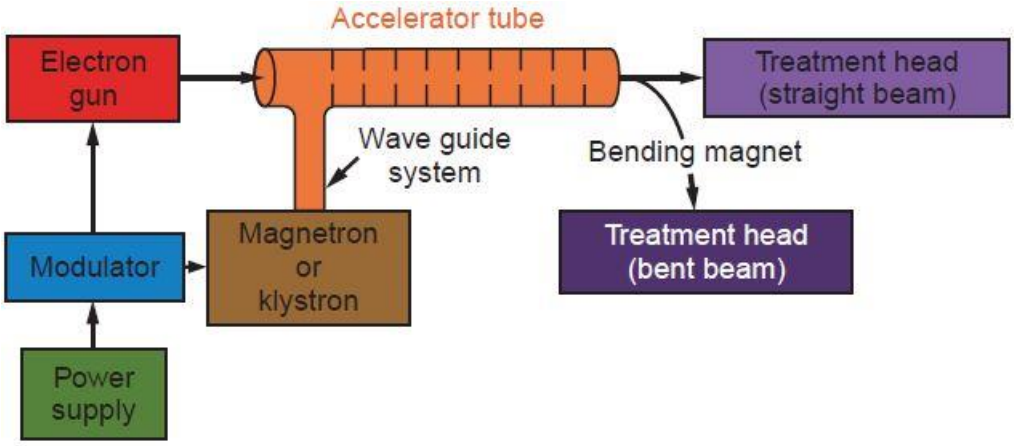

Figure 1.4 Block diagram of a linear accelerator for radiation therapy.[19] Note that the electron target and subsequent flattening filter are located within the treatment head.

1.2.2 Radiation Physics – Photon Interaction

Indirectly ionizing photon beams such as the one produced by a LINAC interact primarily with the flattening filter material, collimators, air molecules, and patient tissue. In each material, x-rays are scattered and absorbed, producing free electrons that are capable of damaging DNA at both target and non-target sites. For radiation therapy, the primary interaction mechanisms of interest include the photoelectric effect, Compton scattering, and pair production.

The photoelectric effect is the process by which an orbital electron of an atom is ejected due to the absorption of a photon with an energy that exceeds the binding energy of that electron. The ejected electron is now referred to as a photoelectron and has a kinetic energy, $E_{kin,ejected}$, equal to

$$E_{kin,ejected} = h\nu - E_{binding} \quad \mathbf{1}$$

where $h\nu$ is the energy of the incoming photon and $E_{binding}$ is the binding energy of the electron. The resulting vacancy in an inner shell of the atom due to the ejection of the

photoelectron means the atom is left in an excited state. To return to the ground state, an electron from a higher shell will fill the vacancy and the atom will emit characteristic x-rays or Auger electrons. The characteristic x-ray or Auger electron will have an energy equal to the difference in energy between the outer shell electron and the inner vacant shell that is filled. The probability of photoelectric absorption is proportional to $1/E^3$ and Z^3, where E is the energy of the incoming photon and Z is the atomic number of the absorber material.

The dominant interaction at therapeutic x-ray energies is Compton scattering. During this process, an incoming photon ejects an electron and is then scattered at reduced energy. Energy and momentum are conserved through the distribution of energy between the photon and electron as well as through the scattering angles of each. The kinetic energy of the ejected electron can be found through the equation

$$E = hv\frac{\alpha(1-cos\phi)}{1+\alpha(1-cos\phi)} \quad \textbf{2}$$

where E is the energy of the electron, hv is the energy of the incident photon, $\alpha = hv/m_0c^2$ where m_0c^2 is the rest mass energy of an electron and equal to 511 keV, and ϕ is the scattering angle of the electron.

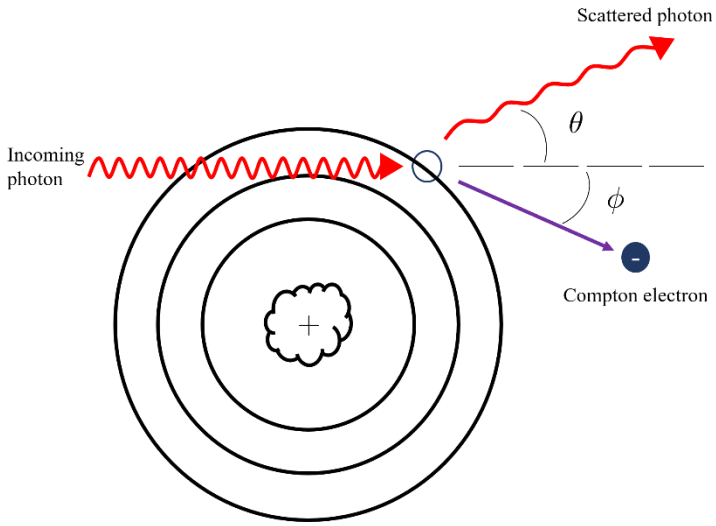

Figure 1.5 Illustration of Compton scattering

The probability of Compton scattering is independent of atomic number, Z, and instead increases with electron density. Furthermore, Compton scattering occurs when there is a large difference between photon and electron binding energies. This is unlike the photoelectric effect, where photoelectric absorption is maximized at photon energies slightly greater than electron binding energies.

The conversion of a photon to an electron-positron pair in the presence of the strong electromagnetic field of a nucleus is known as pair production. With positron and electron rest mass energies of 511 keV, this process has a minimum energy threshold of 1.02 MeV. If a photon with an energy above 1.02 MeV undergoes pair production, the remaining energy is distributed between the electron and positron in the form of kinetic energy. As the positron slows, it will annihilate with a nearby electron, forming two 511 keV photons travelling antiparallel to one another. Interactions through pair production increase with both energy and atomic number, becoming the dominant interaction over Compton scattering at approximately 30 MeV.[20]

In summary, the predominant radiation interactions with matter during radiotherapy are photoelectric absorption, Compton scattering, and pair production. Dominant at energies below approximately 26 keV in water, which simulates soft tissue, photoelectric absorption can only occur during radiation therapy through photons which have lost significant energy after attenuation. Compton scattering dominates between approximately 26 keV and 24 MeV and is therefore the principal interaction mechanism in therapeutic energy ranges of 6-18 MV. Pair production is minimal at lower therapeutic energies of 6 MV but occurs at near equal rates as Compton scattering at 18 MV.[20] A graph of the dominant interaction mechanisms is shown in Figure 1.6.

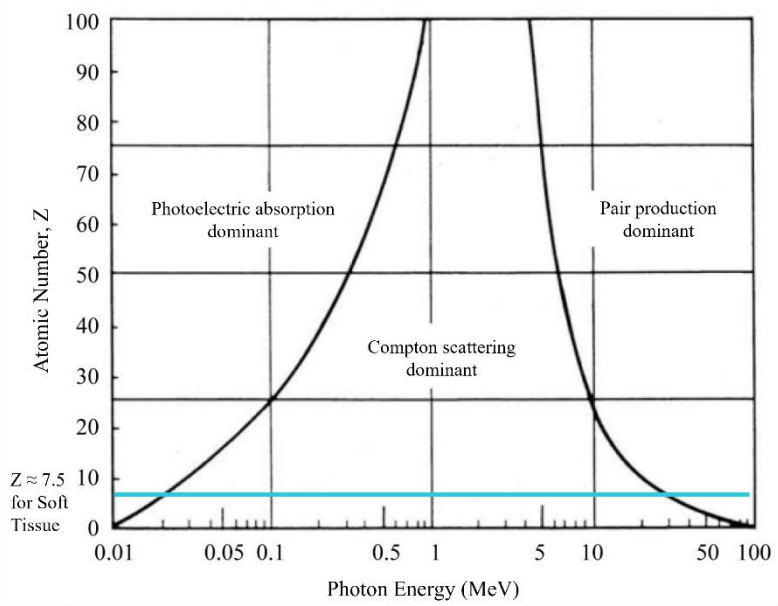

Figure 1.6 Graphical representation of dominant radiation interaction mechanism with respect to atomic number and photon energy. Adapted from Zhang *et al.*[21]

1.2.3 Radiation Biology

The mechanism of interaction with indirectly ionizing forms of radiation such as x-rays begins when the photon transfers its energy to a charged particle such as an electron. This high-energy, fast moving charged particle subsequently deposits its energy through Coulomb interactions with orbital electrons in the surrounding atoms. Ultimately, the primary target of radiation therapy is the DNA of a cancer cell. DNA damage from the energized electrons produced from the initial x-ray interactions occurs through two separate mechanisms: direct action and indirect action. Through direct action, the high energy electron interacts directly with the DNA, causing irreversible damage that leads to cell death. Indirect action, the more common mechanism, results when a high energy electron creates a free radical. Free radicals are highly chemically reactive species characterized by having an unpaired electron in their outermost shell. Due to their reactive nature, they can break bonds and alter the chemical makeup of DNA, eventually leading to cell death. Due to the high concentration of water in the body, hydroxyl radicals are the most common free radicals formed. The processes of direct and indirect action are shown in Figure 1.7.

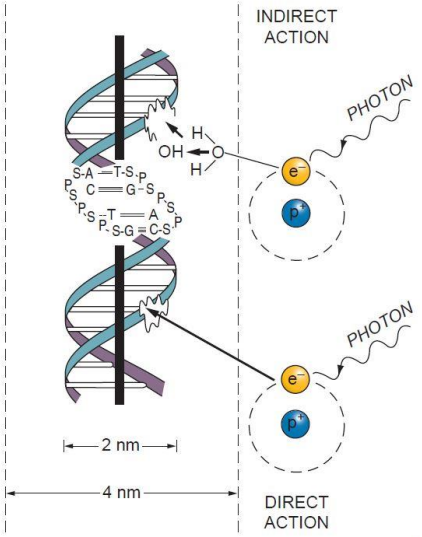

Figure 1.7 DNA damage through indirect and direct action.[22]

1.2.4 Target Definition

Targeting of the tumor volume with the photon beam requires the use of a single or multiple imaging modalities to identify the gross tumor volume as well as surroundings structures such as organs at risk (OARs). Commonly used imaging modalities include computed tomography (CT), magnetic resonance imaging (MRI), and positron emission tomography (PET). Each image can provide different information, whether it be anatomical or functional, to create a 3D representation of the tumor that can be targeted using conformal radiotherapy.

Figure 1.8A and 1.8B show the series of volumes that are defined around the primary volume of the tumor, denoted as the GTV or gross tumor volume, and a representative lung cancer segmentation.[23,24] The GTV margin is first extended to the CTV, or clinical target volume in order to encompass clinical disease spread beyond the main tumor. The internal target volume, or ITV, is an extension of the CTV to account for internal motion of the tumor throughout treatment. Lastly, the planning target volume or PTV is the final margin that is added and accounts for errors in patient setup. In the end, the PTV is the desired volume to be irradiated by the photon beam from the LINAC.

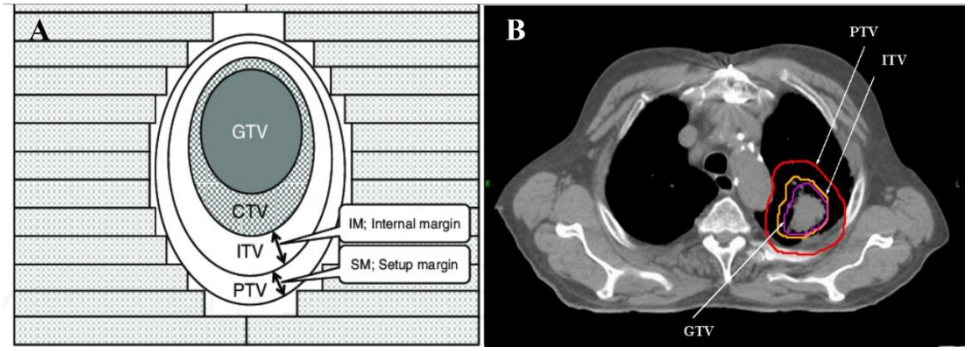

Figure 1.8 A) Outlines of the various tumor and target volumes that encompass the planning target volume (PTV) for conformal radiotherapy[23] and B) representative lung cancer GTV, ITV, and PTV delineations[24]

Multi-leaf collimators (MLCs) imaged as the green rectangles surrounding the PTV in Figure 1.8A, are dynamic, high atomic number metals that shape the photon beam as the x-rays leave the LINAC. By conforming the shape of the radiation beam to the tumor volume, tumor control probability (TCP) is maximized, and normal tissue complication probability (NTCP) is minimized. This concept is shown in Figure 1.9[25], where the therapeutic index is the ratio of TCP to NTCP and should be maximized for best patient outcome.

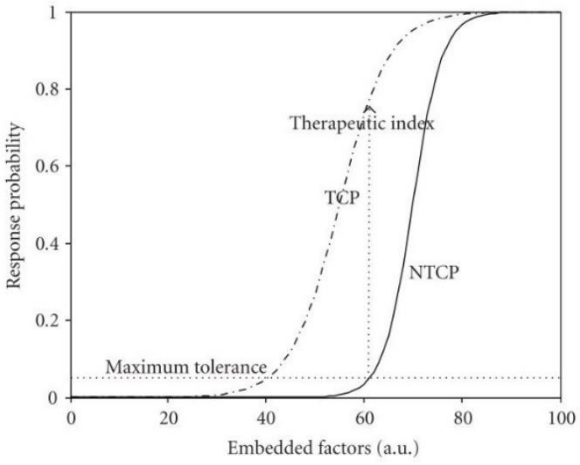

Figure 1.9 Tumor control probability and normal tissue complication probability response curves as a function of various radiotherapy treatment factors. Embedded factors could include dose, biomarkers, or clinical factors. Goal of radiation therapy is to maximize therapeutic index.[25]

1.2.5 Motion Management

In radiation therapy, several challenges must be addressed to ensure that the dose given to the patient is highly conformal to the tumor volume. One of these challenges is motion management, which has received significant attention in recent years. Internal motion due to respiration or blood flow can cause varying degrees of tumor volume displacement. Research has shown that higher biologically effective doses during radiation therapy is associated with both improved local-regional control (LRC) and an increase in survival rates.[26] It is also known, however, that intensifying radiation treatments beyond common 60-66 Gy doses can introduce additional complications due to normal tissue irradiation. High radiation doses and normal tissue irradiation are especially difficult to withstand for patients undergoing concurrent chemotherapy.[26] To increase the dose to the tumor while avoiding dose to healthy tissue, the effects of respiratory motion on the target must be understood. The American Association of Physicists in Medicine (AAPM) report number 91 discusses the challenges and need for managing respiratory motion to deliver precise radiation treatment.[27]

Motion management techniques can be applied both at the planning and delivery stages of radiation therapy to account for emerging errors at each stage due to motion. In the planning stage, 4DCT and hybrid PET/CT scans are used to define target volumes as described in the previous section. During acquisition of a 4DCT slice, image reconstruction algorithms assume constant patient anatomy.[27] Therefore, if significant or irregular motion is present during acquisition, artifacts can be created both within and between slices. When viewing the final image, there may significant blurring or misalignment between structures. Non-gated PET scans produce images that show the average location of a lesion throughout the respiratory cycle and are often blurred. Additionally, patient breathing and positioning can vary between imaging with 4DCT and PET. Each source of error listed above can accumulate when images from multiple modalities are co-registered, or fused. For example, hybrid PET/CT images are acquired in two parts: first, a CT image is acquired with a short acquisition time followed by the PET component that requires two or more minutes. If motion is present, a blurred

distribution of radiopharmaceutical uptake must be registered to a CT image that, due to the short acquisition time, is similar to a static CT acquisition. This creates an opportunity for misalignment by the scanner when displaying the final image. If this PET/CT is then propagated to a 4DCT, there is an additional chance for registration errors due to blurring in the PET image, differences in patient positioning, and differences in acquisition protocols. An example of a misalignment between CT and PET resulting from respiratory motion is shown in Figure 1.10.[28] Here, a CT was acquired separately from a PET/CT and then fused. The compounding of the above errors can result in treatment volumes that are not replications of the real tumor environment. The real tumor environment is also subject to change between treatment planning and delivery, interfractionally, and intrafractionally. These changes could include shrinking, growing, and shifting of the target.

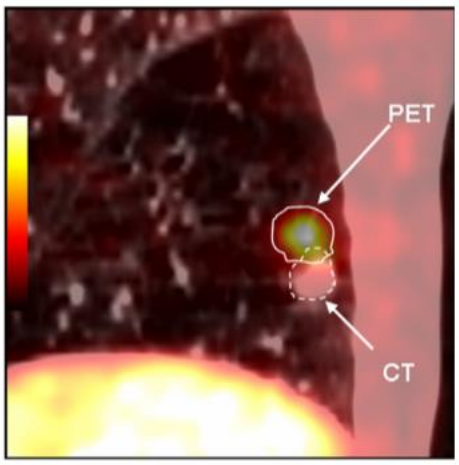

Figure 1.10 Misalignment between PET and CT images as a result of respiratory motion.[28]

As a result of these challenges, displacement of the tumor volume can lead to the irradiation of healthy tissues or organs at risk, as well as decreased dose to the target. Furthermore, there has been found to be significant inter- and intra-physician variation in GTV delineation for lung cancer.[27] This finding encourages the creation of protocols that improve reproducibility and precision of lung cancer treatment plans.

Improvements which account for motion and allow for better targeting can either be made during the treatment planning process or in real time during the radiation treatment itself. The five main techniques used to mitigate the effects of respiratory motion include respiratory gating, breath holds, forced shallow breathing, tumor tracking, and motion encompassing methods. Each method has associated advantages and disadvantages; for example, the Real-Time Position Management Respiratory Gating System by Varian uses an infrared-reflective block that is placed on the patient's chest or abdomen to track inhalation and exhalation. Numerous studies have found that errors due to motion are reduced, however at a cost of an extended treatment time and additional dose errors due to delays between MLCs and the gating system, the dose rate, and the number of beam hold-offs.[29,30] Additionally, there is still considerable research required to correlate internal tumor motion based on external gating devices.[31] Breath holds and forced shallow breathing can also be used to limit the motion of a tumor, however these techniques are often not feasible for patients with cancers of the lung. Emphasis for this project will be on motion encompassing techniques, as this is the method utilized at the Juravinski Cancer Centre (JCC) in Hamilton, Ontario. Here, an internal target volume as described in Section 1.2.4 is defined, and radiation is delivered to entire volume where the tumor is displaced throughout the respiratory cycle. The main challenges with this technique are properly defining the ITV and reducing contouring variation between clinicians. It is believed that better integrating PET into 4DCT treatment planning can address these challenges. First, by fusing PET and 4DCT, healthy and diseased tissue can be distinguished using functional information provided by PET, while overall anatomical accuracy is retained from CT. Since PET is an averaged image over multiple respiratory cycles, the full range of motion of the lesion should be visible and comparable to the maximum intensity projection used to gauge motion extent in 4DCT. Modern treatment planning programs also have automated segmentation algorithms that can quickly define regions-of-interest on PET images, and may reduce contouring variation between clinicians if provided as a starting point. In nuclear medicine, the ROIs of suspected tumors segmented on PET are typically referred to as the total metabolic tumor volume

(TMTV). Since this study is concerned with motion management and the delineation of an ITV, PET EDGE segmentations will be compared to conventional ITVs generated using CT. Despite the promise that PET has in aiding ITV delineation and improving reproducibility, the workflow is susceptible to motion-associated errors outlined above, such as misalignment between PET and CT images. Additionally, it is unknown how volumes delineated from PET contouring algorithms compare with known volumes or those delineated using CT. In this project, we aim to evaluate the performance of PET automated segmentation algorithms to improve this motion encompassing treatment method.

1.2.6 NSCLC Radiation Treatment Planning at Juravinski Cancer Centre

Radiation treatment planning for NSCLC at the Juravinski Cancer Centre begins with the acquisition of an externally gated 4D planning CT. The advantage of 4DCT over conventional 3DCT is the ability to create multiple images throughout the respiratory cycle to aide in the tracking of tumor motion. Prior to image acquisition, patients are positioned on their backs with arms above their head on a flat couch. Various supports can be used to ensure patients are comfortable and can remain still throughout both imaging and the following treatment. Bed position data, supports used, and tattoos are recorded and applied to ensure high positioning reproducibility between imaging and treatment. During imaging at the JCC, 10 binned image sets at equally spaced breathing points are acquired with the aid of a Varian respiratory tracking system. From these images, four new image sets are constructed and exported to the treatment planning software Pinnacle: untagged (average), full-exhale, full-inhale, and a maximum intensity projection (MIP). The untagged image set is an average of the 10 binned CT image sets. Delineation and contouring of organs at risk and structures other than the tumor are done using this image. The ITV is contoured using the MIP, as this represents the entire volume that encompasses the tumor throughout the breathing cycle. This method is also the standard of care for target delineation in lung radiotherapy.[32] The physician will then verify the MIP contour with the full-exhale and full-inhale images to insure the entire target is contoured. Full-exhale for each patient is typically at 0% of their inhale, however

the full-inhale for each patient can vary and is typically around 60% of the maximum filling of the lung. From the ITV contour, the PTV margins are then added to account for errors during patient setup.

In addition to the overall treatment procedure, there are numerous important technical details regarding 4DCT acquisition. Modern CT scans are acquired helically; here, patients move translationally through the CT with the x-ray tube and detector array rotating continuously around them. This process is shown in Figure 1.11.[33] Image reconstruction algorithms can then be used to take the helical projections and convert them to planar images. The pitch factor of the helical scan, which represents the distance

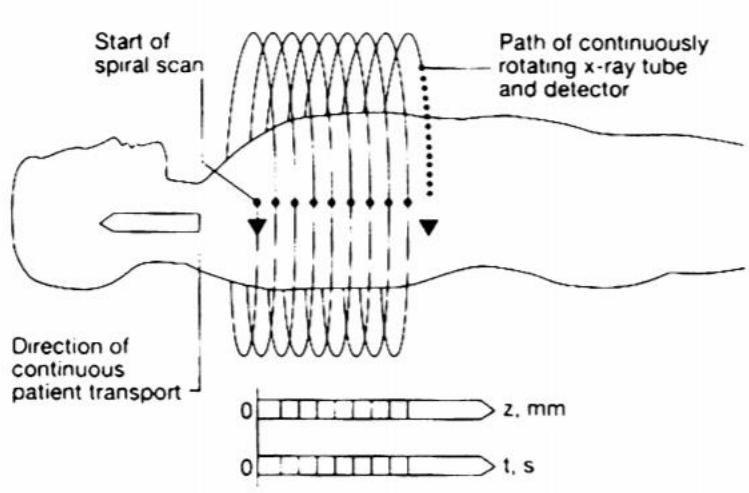

Figure 1.11 Helical CT acquisition[33]

the patient couch travels per gantry rotation divided by the detector collimation, is dependent on the respiratory frequency of the patient.[34] The pitch must be low enough to avoid motion artifacts by ensuring that each volume slice covers at least one respiratory cycle, but high enough such that the scan can be completed within 120 seconds to prevent overheating of the X-ray tube.[34] For reference, an average human respiratory cycle lasts 3-6 seconds, or an average breaths per minute (BPM) of between 10 and 20. As an example, the maximum pitch that can be used for the Philips Brilliance CT Big Bore is given by

$$p_{max} = \left(\frac{t_{rot} \bullet f}{60}\right)\left(1 - \frac{FOV}{2R}\right) \quad \textbf{3}$$

where t_{rot} is the gantry rotation time in seconds, f is the patient's respiratory frequency in BPM, FOV is the field of view in millimeters, and R is the distance from the focus to the CT isocenter.[34] Low pitch helical 4DCT, such as the one used here, benefits in both flexibility and accuracy over traditional cine axial CT. Unfortunately, due to the periodic assumptions from 4D reconstruction algorithms, motion artifacts are more likely to occur in lung cancer patients since poor lung function, difficulty breathing, and concurrent chronic obstructive pulmonary disease (COPD) can lead to irregular breathing patterns.[32] The fast gantry rotation speeds of more modern CT scanners such as the Philips Big Bore and Siemens Somatom can minimize these artifacts, however, due to the faster acquisition time.[32] According to the white paper by Philips Healthcare, the Brilliance CT Big Bore has a gantry rotation time of either 0.44 seconds or 0.5 seconds depending on the breathing rate and associated pitch factor. Nominally, the temporal resolution is equal to half of the rotation time, meaning this CT scanner has a temporal resolution of between 0.22 and 0.25 seconds.[35]

Currently, diagnostic PET/CT images taken at St. Joseph's Healthcare Hamilton are also used to assist in the treatment planning process. These images may be taken months prior to the actual treatment and may or may not have the patient in the same position as in the 4D planning CT and during therapy. During 4DCT imaging and subsequent radiation treatment, the patient is positioned with arms above the head on a flat couch. In the diagnostic PET/CT, however, patients are on a rounded couch and not in treatment position. These differences in position can generate geometric errors. The 3D PET/CT image is then fused with the 4D planning CT on Pinnacle using rigid image registration. On a separate screen, the data from PET can be used not to contour directly, but to help the physician determine the extent of disease spread and the general location of the tumor. By gaining this additional functional information that PET provides, the physician can adjust their contours based on their respective experience. A summary of this procedure is shown below in Figure 1.12.

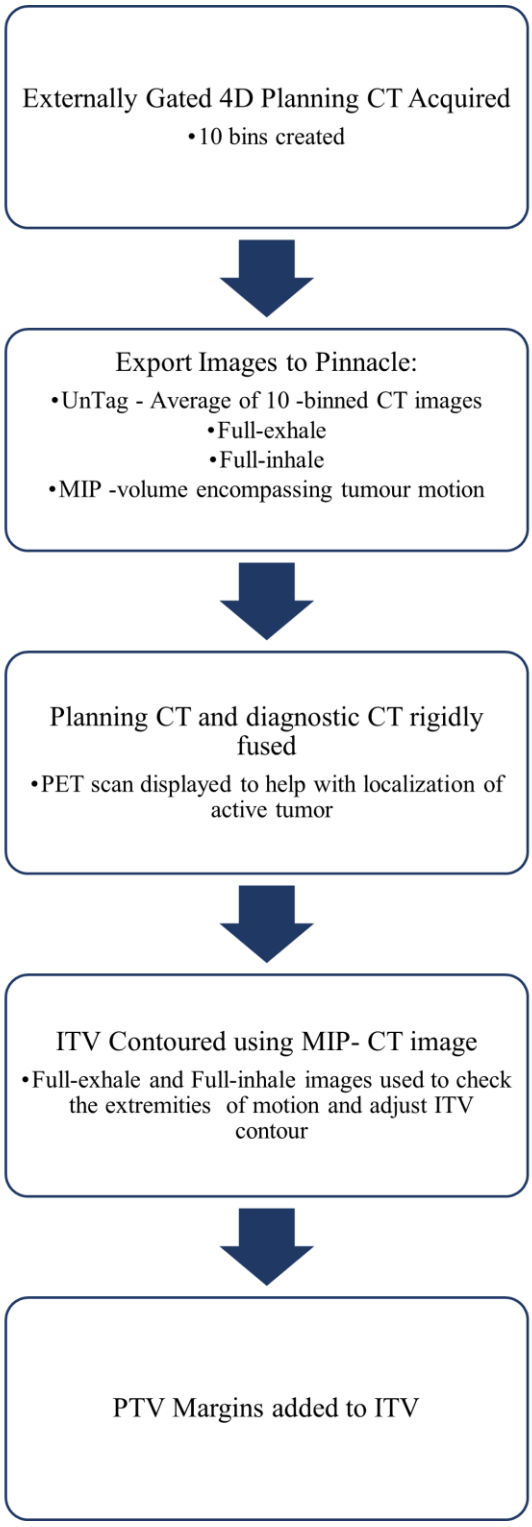

Figure 1.12 Summary of radiation treatment planning process at the Juravinski Cancer Centre in Hamilton, ON, CA.

1.3 Positron Emission Tomography

1.3.1 Working Principles

Positron emission tomography (PET) is a diagnostic nuclear imaging technique that uses radiolabeled, positron-emitting molecular probes to target a biochemical process and create images showing functional aspects of that process. Patients with suspected tumors are first injected with a positron-emitting radionuclide that is designed to be up-taken by specific metabolic processes based on the tumor type. The most common radiopharmaceutical is ^{18}F-fluorodeoxyglucose (18-FDG), which is a radioactive glucose analogue with a substituted fluorine-18 atom. Due to the higher metabolic activity of cancerous cells, uptake of 18-FDG is increased when compared to healthy cells, creating a contrast in activity. As the ^{18}F decays, the released positrons travel until interacting with an electron. This antiparticle-particle interaction results in the conversion of the particle masses to their rest mass energy equivalent through an annihilation event with the release of two 511 keV photons travelling anti-parallel to one another. As this occurs, the patient is positioned on a couch, surrounded by a circular array of scintillation detectors. Coincidence events are analyzed to evaluate whether the detection events correspond to the same annihilation event. This is based on the geometry, energy, and timing of the scintillation events. Figure 1.13 shows a visualization of this process.

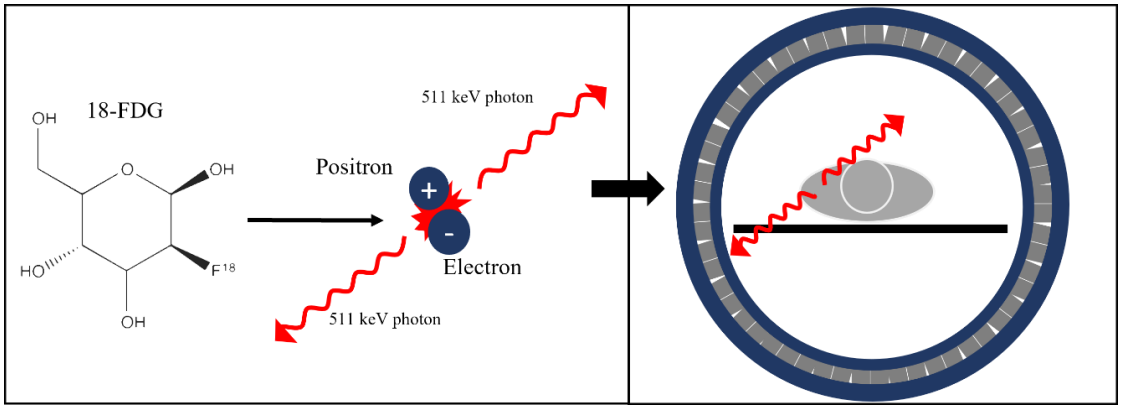

Figure 1.13 Working principle of positron emission tomography. Note that intravenous injection of 18-FDG occurs approximately 1 hour prior to imaging to allow for uptake.

To correct for attenuation of the 511 keV photons, the CT modality of a hybrid PET/CT scanner is used. If the detected events are confirmed to be from the same annihilation event, a unique line of response for the annihilation event is calculated, and a tomographic image is generated. Aside from a true line of response that corresponds to true coincidence event, random and scattered coincidences can also occur due to lost signals or scattered photons. These undesirable coincidence events, along with other inherent limitations of PET, can degrade image quality. For example, spatial resolution is limited by the distance a positron travels before annihilating with an electron. This range is approximately 0.5 mm for ^{18}F, but can be higher for other positron emitting isotopes.[36] Combined with other limiting factors such detector width and photon noncollinearity, PET scanners are typically limited to spatial resolutions between 2 and 5 mm.[36] Breathing artifacts are also created due to respiratory motion since the acquisition time of a PET image is on the order of minutes and cannot be obtained in a single breath hold.[37] If the acquisition time is decreased, motion artifacts can be decreased but this is at the expense of acquiring sufficient count statistics to generate an image.[37] Four dimensional PET/CT technologies exist and allow for gating, however this requires longer acquisition times to generate sufficient count statistics, and it is unclear whether 4D PET/CT is more accurate at delineating lung tumors than 3D PET/CT or 4DCT alone.[37]

1.3.2 Diagnostic Imaging Procedure at St. Joseph's Healthcare Hamilton

Patients with suspected lung cancer undergo first a diagnostic hybrid PET/CT scan using a Discovery MI scanner by GE Healthcare. As a hybrid PET/CT scanner, the Discovery MI has both CT and PET imaging modalities. The CT has a spatial resolution of 0.28 mm, with a x-ray tube rotation speed of between 0.35 s and 1.0 s for helical scans. The PET scanner uses 544 lutetium-based scintillator (LBS) detector blocks with silicon photomultipliers. There are a total of 36 detector rings and 19584 scintillation detector crystals. The spatial resolution varies between 4.00 mm and 4.8 mm, which is notably poorer than the 0.28 mm resolution for the CT portion of the Discovery MI scanner.

The diagnostic PET/CT procedure begins with the patient being administered 18-FDG at an activity of 5 MBq/kg. Imaging is then initiated after a 60-minute uptake period. Most patients are imaged headfirst, supine, with images generated starting at the thighs and moving superiorly. If feasible, the patient is imaged with their arms above their head. This minimizes attenuation artifacts and is also more geometrically aligned with the radiation treatment position. All patients are imaged on curved beds as opposed to an available flat pallet, as it is unknown whether the patient will eventually be receiving radiation treatment.

The duration of the imaging procedure is dependent on the mass of the patients. Patients weighing less than 90 kg are imaged at 2 minutes per bed position, with each bed position being 25 cm, 8 cm of which is overlap between beds. Patients weighing above 90 kg are imaged at 3 minutes per bed position. The total scan time is approximately 30 minutes. The final, ungated PET image is spatially co-registered with the CT image. If radiation treatment is prescribed, the image set is sent to the JCC to be used as described in Section 1.2.6. MotionFree digital respiratory motion management software is available; however, it is not used due to multiple factors including increased image acquisition time and logistical issues. A summary of this imaging procedure is shown in Figure 1.14.

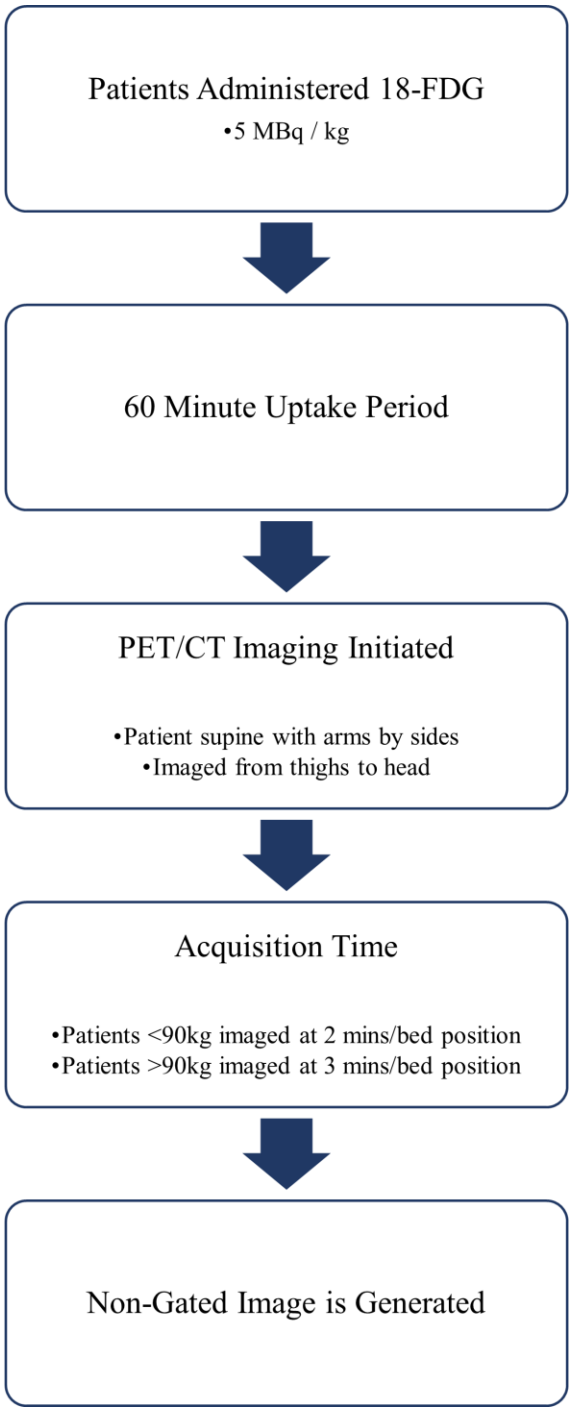

Figure 1.14 Summary of the PET/CT diagnostic imaging procedure at St. Joseph's Healthcare Hamilton in Hamilton, ON, CA.

1.3.3 Potential of PET in NSCLC Radiation Treatment

Segmentation of a GTV for NSCLC patients using CT alone can result in inaccuracies due to poor contrast between healthy tissue and target lesions. As mentioned previously, improper definition of the GTV can lead to the undesired irradiation of healthy tissue or underdosing of the tumor. The implementation of functional imaging modalities such as PET has been used to provide functional information in addition to the anatomical information provided by CT, with the goal of improving radiation treatment outcomes.[38,39] Figure 1.15 shows a lesion that is not visible on CT due to poor contrast but can be easily seen on PET.[40]

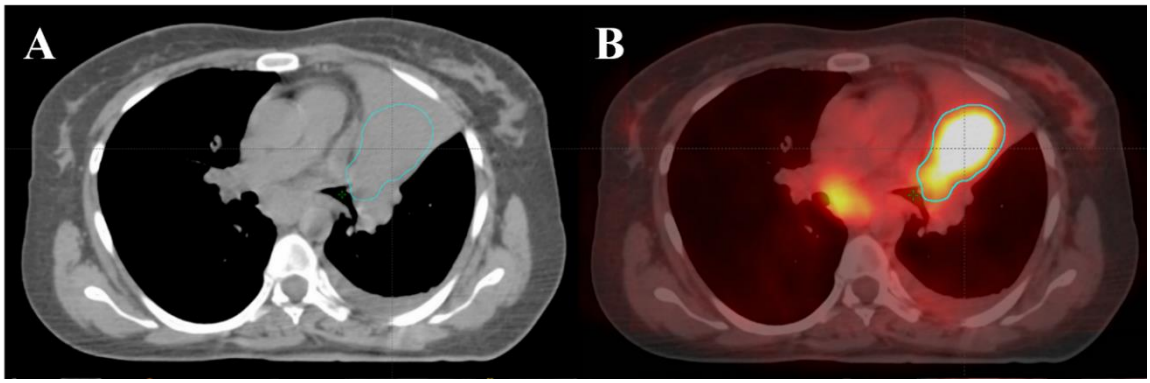

Figure 1.15 Lesion that cannot be seen on A) CT but is easily distinguished on B) fused PET/CT[40]

At the Juravinski Cancer Centre, the role of PET in the radiation treatment process is limited as tumor delineation does not involve direct contouring on the PET image. In patients with poorly defined NSCLC on CT, it has been found that a more consistent GTV can be obtained if the CT images are co-registered, or fused, with FDG-PET images.[10] The study used the coefficient of variation to assess the variability of contouring between physicians, where the coefficient of variation was the standard deviation of the mean GTV volume divided by the mean. With a data set consisting of 30 patients, each physician defined a GTV using the planning CT alone and the planning CT fused with PET/CT scans. Results found that there was a high degree of inter-physician variation when defining the GTV using CT alone even with well-established guidelines.[10] Furthermore, the mean coefficient of variation decreased from 0.34 to 0.22 when

contouring only on CT to contouring with the fused PET/CT image.[10] The study, however, had multiple differences in the treatment planning process when compared to that at JCC. First, fusion was completed based on eight fiducial markers implanted in the patients. Patients also underwent their PET/CT scan on a flat pallet, and in the radiation treatment position.[10] These differences could indicate that a change in JCC procedures could be required to improve variability. A study by Bradley *et al.* evaluated the differences in GTV delineation for 3D conformal radiotherapy of NSCLC using CT and PET/CT images.[41] GTVs were contoured on 24 patient images by two separate physicians: one physician contoured only on the CT image set and the second only used the fused PET/CT images. In total, contouring on PET/CT resulted in changes to 14 out of the 24 patient treatment plans. Eleven of these changes resulted in GTV volume increase from additional tumor detections, and three resulted in GTV volume decreases due to detection of atelectasis. Using additional data from literature, the authors concluded that the precision of GTV coverage would increase in 30-60% of patients who undergo PET simulation prior to NSCLC radiotherapy. In a similar study by Spratt *et al.*, the authors found that contouring on PET/CT resulted in an average decrease in GTV of 10% compared to CT across 11 patients with NSCLC.[42] Furthermore, PET discovered a benign pulmonary process in four of the patients that negatively affected the accuracy of delineation on CT alone. Faria *et al.* also compared target delineation on CT alone versus on co-registered PET/CT.[43] Here, 18 of the 32 patient contours were altered after using PET compared to CT alone. As with the former two studies mentioned, Faria *et al.* stated that although PET changes tumor contours, it remains unknown whether contour changes result in improved patient outcomes or quality of life.[41–43]

With the development of modern treatment planning software, multiple automated segmentation algorithms (ASAs) now exist to assist in the delineation of targets directly on PET/CT images. Threshold algorithms define the tumor border based on an area of tissue with a greater radiotracer uptake than a pre-defined value. Absolute thresholds generate contours around a region where a defined minimum standardized uptake value (SUV) of FDG is exceeded. Percent constant threshold algorithms contour tumors based

on the percentage of maximum activity within the tumor, and adaptive threshold contours are based on the tumor size and ratio of activity in the tumor compared to background levels.[44] Threshold algorithms also operate on a number of assumptions that limit their accuracy: that the true object has a well-defined boundary and uniform uptake near this boundary, background intensity is uniform around the object, noise in the background and in the object is minimal compared to the intensity change at the border, and that resolution is constant near the tumor border.[45] Gradient based ASAs such as PET EDGE, on the other hand, contour tumors based on the rate of change in count levels at the border of the tumor.[44] With this approach, the target does not need to be uniform nor does the activity need to be constant along the border since it is measure the rate of change of the activity. This approach is, however, effected by image noise.[45] Numerous studies comparing threshold and gradient based ASAs concluded that gradient segmentation had superior accuracy and reliability when compared to threshold segmentation.[44,46]

To further integrate the information provided by PET/CT with the 4D planning CT, accurate propagation of the PET/CT image to the 4DCT is required. Rigid registration of the PET/CT image to 4DCT, as used on Pinnacle at JCC, has been found to be insufficient for organs such as the lungs that have large deformation.[47] Alternatively, deformable image registration (DIR) algorithms can be used to fuse images by mapping volume elements from one image to corresponding voxels in another.[48] This is a considerably different approach compared to rigid image registration (RIR), which fuses images through translations and rotations. DIR does have limitations, including the risk of ambiguity of deformation in areas of low tissue contrast due to the large number of degrees of freedom involved with matching voxels.[49] This means they are not as intuitive and are harder to validate than RIR algorithms. Nonetheless, they are more sophisticated and can offer superior registration accuracy. As patients are not always imaged with their arms above their head or on a flat pallet at SJHH, DIR algorithms could be advantageous over RIR algorithms when fusing a PET/CT scan with a 4D planning CT taken in the treatment planning position. Proper propagation of the diagnostic PET/CT to the 4D planning CT coupled with ASAs to provide a starting point

for physicians when delineating the target volume could lead to more precise and effective NSCLC radiation treatment.

1.4 Project Goals

The goal of this project is to propose a better use of diagnostic PET/CT for a more precise delineation of tumors on 4D planning CT images at the JCC. It requires the assessment of numerous stages of the treatment planning process, including:

1. the quantification of respiratory motion in positron emission tomography,
2. evaluating the accuracy of contouring on PET and 4DCT, and
3. the fusion of PET and 4DCT images

This project will use a 4D extended cardiac-torso (XCAT) digital phantom, a Clinical Trials Network (CTN) phantom from the Society of Nuclear Medicine[50], and a custom-made 3D-printed irregularly shaped lesion to evaluate a workflow that improves the integration of PET/CT images in the treatment planning process. The XCAT digital phantom will be used to reproduce realistic respiratory motions and quantify tumor displacement because of breathing. These displacement parameters will be translated to the CTN phantom placed on a moving platform to undergo imaging with the Discovery MI PET/CT scanner at SJHH. Both the physical and digital phantoms provide the ability to assess the motion of an insert with a known volume as it undergoes a simulated respiratory motion. Finally, 4D planning CT and hybrid PET/CT scans of a 3D-printed irregular lesion will be acquired. This lesion will be submerged in a gel and imaged under static and dynamic scenarios. Each of these phantoms have their own advantages: the digital phantom provides a more accurate representation of both anatomy and respiratory motion and can be generated without degradation due to the software and hardware limitations and PET and CT scanners. On the other hand, the physical phantom offers less realistic anatomy and motion but allows for the assessment of image degradation because of PET and CT scanner limitations. Additionally, an irregularly shaped lesion may expose limitations of segmentation or fusion techniques and can provide a better evaluation of the overall workflow. Comparison of known volumes with the volumes

determined by manual contouring and with the PET EDGE gradient-based ASA on the software MIM Maestro can assess the feasibility and accuracy of defining target volumes using PET.

2 Methods

This project is comprised of two parts: a simulation study with the digital XCAT Version 2 phantom, and a verification experiment using a CTN phantom and a 3D-printed irregular lesion. The first part of this section will describe the simulations with the XCAT phantom to quantify realistic breathing motion. The second part will describe the experiments with the CTN phantom and an irregular lesion.

Note that a digital or computational phantom refers to a computer-based anatomical representation of the human body. A physical phantom comprises tissue-equivalent material and can be directly imaged by a medical scanner.

2.1 The 4D XCAT Digital Phantom

In the field of medical physics and radiation sciences, digital phantoms are used for dose determination and replication of imaging and radiotherapy procedures without the expense and radiation safety considerations associated with physical phantoms.[51] Before modern hybrid techniques, digital phantoms belonged to one of two groups based on how they were modelled: voxelized or mathematical. Voxelized phantoms are created from tomographic images of patients and provide excellent three-dimensional anatomical accuracy.[52] Limitations of this method, however, are numerous: structures with dimensions smaller than the voxels base image cannot be accurately delineated, organ surfaces are rough rather than smooth due to the cubic shape of a voxel element, accuracy does not translate well between individuals, and it is challenging to model motion and its effects on a structure.[52,53] Mathematical phantoms, on the other hand, use equations to define the geometry of the various organs and structures within the body. This allows for easy manipulation of the structures, but mathematical phantoms lack anatomical accuracy due to the simple geometric definitions of the organs.[51,53]

Description

The 4D extended cardiac-torso (XCAT) phantom was developed by Segars *et al.* for multimodality imaging research.[53] This hybrid computerized phantom utilizes both

voxelized and mathematical methods described above by mathematically defining structures based on segmented patient data.[53] To create an accurate 3D model of both male and female anatomies, the authors used the Visible Human Male and Female anatomical data sets from the National Library of Medicine in the United States. These high-resolution CT data sets contained transaxial slices across the whole body with 0.33 mm pixel widths for both males and females, and slice thicknesses of 1.0 mm for males and 0.33 mm for females. Organ masses from this data set were then altered slightly to ensure that they were within 5% of the organ masses stated in ICRP Publication 89 – Basic anatomical and physiological data for use in radiological protection.[53,54] The anatomical images were then segmented and each object was defined mathematically using nonuniform rational B-splines (NURBS) or polygon meshes on the patient data obtained above. The use of these mathematically defined organ volumes and structures allows the XCAT to transform and replicate physiological movements while maintaining high degrees of anatomical accuracy.

Respiratory motion is one physiological processes that is modelled by the XCAT and is important for this study. In the first spline-based MCAT, a predecessor the current XCAT, control points on the NURBS surfaces were translated to simulate motion of structures such as the diaphragm. The NURBS surfaces for the lung and body outline were linked to the ribs. The ribs were defined by the short and long axis of the rib as well as the rib tilt angle. Therefore, the lungs and body outline rotates, expands, and contracts according to movement of the ribs. By changing the phantoms over time, the authors created continuous 4D respiratory models.[55] The volumes of lungs during normal respiration follow a volume curve that is shown in Figure 2.1 and approximated by Equation 4.

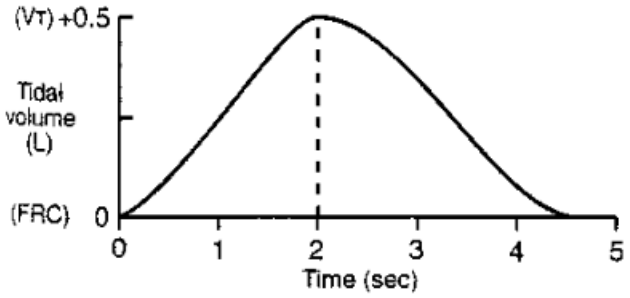

Figure 2.1 XCAT volume curve for normal tidal breathing.[55]

$$V\ t\ = \begin{cases} -250ml\ cos\left(\frac{\pi}{2}t\right) + 250, & 0 \le t \le 2 \\ -250ml\ cos\left(\frac{\pi}{3}(5-t)\right) + 250, & 2 \le t \le 5 \end{cases} \quad \textbf{4}$$

The height of the diaphragm throughout breathing is also set to vary according to the piecewise function shown in Equation 5.[55]

$$\Delta_{diaphragm}(t) = \begin{cases} 0.5cm\ cos\left(\frac{\pi}{2}t\right) + 0.5, & 0 \le t \le 2 \\ 0.5cm\ cos\left(\frac{\pi}{3}(5-t)\right) + 0.5, & 2 \le t \le 5 \end{cases} \quad \textbf{5}$$

Originally based on respiratory gated data from a single patient, the next version of the XCAT analyzed 4D respiratory-gated multislice CT images collected from 20 subjects breathing normally. Each scan comprised 10 frames over the respiratory cycle, with a pixel width and slice thickness of 0.89 mm and 2.5 mm, respectively. The authors altered certain parameters based on observations from these scans: anterior movement of the body, ribcage, and lungs was similar during inhalation, minimal lateral expansion of the lungs was seen, and overall chest expansion was reduced.[56] Respiratory motion parameters for the most recent XCAT version used for this research are based on the older NCAT but have enhanced details and includes motion of pulmonary vessels and muscles.[53] The AP curve determines the upwards and outwards rotation of the ribcage and the forward movement of the diaphragm, and the diaphragm curve determines the inferior contraction of the diaphragm. The standard curves are shown in Figure 2.2 but can be manipulated by the user. Finally, spherical lesions of various sizes can be inserted into the lung and will move according to the respiratory motion.[53]

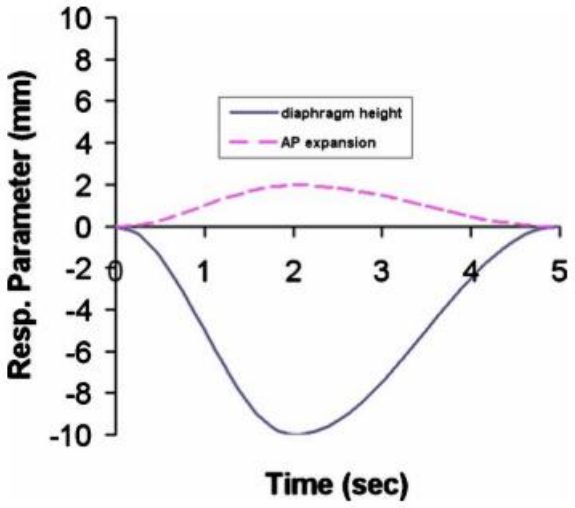

Figure 2.2 Diaphragm and AP curves for the XCAT.[53]

The XCAT has some limitations, such as assuming each tissue is homogenous in composition. Therefore, the vector fields used to characterize the motion cannot account for any differences that may result from the interaction of heterogeneous tissues. Finally, as the data from the Visible Human dataset did not reflect the average height and weight of a male or female, the authors used the features of the NURBS surfaces to convert the default phantom to reflect a 50th percentile American male and female in both height and weight.[53]

Workflow

Eleven image sets of a phantom were first generated over one respiratory cycle. Ten of these image sets are snapshots of a specific respiratory cycle phase, and the eleventh is an average of the previous ten sets. Independent simulations were then run for multiple spherical lesions inserted at various locations throughout both lungs. The displacements of the spherical lesions were measured using ImageJ. Finally, the imaging software package AMIDE was used to measure the volumes of the target on the average image set and the volume of simulated lesions on maximum intensity projection images that were manually created in ImageJ.

2.1.1 Phantom and Lesion Generation

Phantom Generation

A wide variety of customizable parameters can be chosen within the input file for the XCAT phantom to suit the user's needs and meet the research goals. The phantom was first generated with special consideration to parameters concerning the lungs and diaphragm to study the effects of respiratory motion on lesion displacement. The time over which the phantom was generated and the output resolution were chosen based on several considerations and compromises discussed below. All other parameters such as the size of various anatomical structures and motion of the heart were left at their typical values as determined by the authors' methods described in Section 2.1 for males. The remainder of this section will state and explain the tunable parameters and the numerical value associated with these in the input file.

For the phantom to display both respiratory and heart motions, the motion_option parameter was set to 2. Apart from expansion and contraction of the diaphragm and volume change in the lungs, respiratory motion also influences the motions of nearby organs. Heart motions include both the beating and translations of the heart while it beats. The alter_lung_dens parameter was set to 1 to account for the change in lung density with respiratory motion as opposed to remaining constant. The length of the respiratory cycle was kept at its default value of 5 seconds by setting resp_cycle = 5, with the phantom generation beginning at full exhale by having the resp_start_ph_index set to 0. The maximum diaphragm motion as well as the maximum anterior-posterior expansion of the chest were dependent on which of two scenarios were being studied. First, for a normal breathing scenario, the max_diaphragm_motion parameter was set to 2.0 cm and the max_AP_exp parameter was set to 1.2 cm. These were default values listed for the program. A second study was completed to observe changes in patients with more deep or exaggerated breathing. Here, the values for the maximum diaphragm motion and maximum AP expansion were set to 3.0 cm and 1.8 cm, respectively. The value for the maximum diaphragm motion was based on a study by Liao *et al.*[57] and the AP value was

chosen to maintain the same ratio of diaphragm to AP motion as in the normal breathing scenario.

Parameter	Input File Value	Function
motion_option	2	Exhibit respiratory, heart, and nearby organ motions
alter_lung_dens	1	Change lung density as respiration progresses
resp_cycle	5	Length of respiratory cycle in seconds
resp_start_ph_index	0	Begin respiratory cycle at full exhale
max_diaphragm_motion	2 (normal breathing), 3 (deep breathing)	Diaphragm displacement in centimetres
max_AP_exp	1.2 (normal breathing), 1.8 (deep breathing)	AP chest expansion in centimetres

Table 2.1 Input file parameters for XCAT phantom generation. Deep breathing values were chosen based on the study by Liao *et al*.[57]

Despite the accuracy and customizability of the XCAT, there are a few limitations with the chosen parameters above. The phantom will exhibit a regular motion throughout the respiratory cycle that is equivalent to a patient whose breathing is perfectly consistent throughout imaging, which is unlikely for a patient with lesions in the lung. While the average respiratory cycle across all populations is approximately 5 seconds, this value can vary between patients depending on factors ranging from stress levels to detriment from COPD or cancer itself.

Output Specifications	Value
Phantom generation length	5 seconds
Number of image sets	10
Time per image set	0.5 seconds
Inhalation state image sets	0%, 22%, 44%, 66%, 88%
Exhalation state image sets	8%, 27%, 45%, 63%, 82%
Average image	Yes – generated during simulation
Maximum Intensity Projections	No – generated manually
Voxel dimensions	2 mm x 2 mm x 2 mm
Subvoxel index	3 (27 subvoxels per voxel)

Table 2.2 Output specifications for XCAT phantom generation.

The output specifications for the phantom, as shown in Table 2.2, were based on storage limitations, computation time, resolutions of CT and PET scanners, and current NSCLC treatment protocols at JCC. The time-per-image set of 0.5 seconds is approximately equal to the temporal resolution of modern 4DCT scanners. Also, 10 image sets is the number of image sets used to create the average (UnTagged) CT image at JCC and is within the 8-16 image set range recommended by the authors to create a "good" averaged image with the XCAT. The inhalation and exhalation state image sets are analogous to the binned image sets acquired during conventional 4DCT. The exact phases cannot be chosen manually, but are based on the time per image set, the total number of image sets, the respiratory cycle length, and the default respiratory curve defined by the authors. A subvoxel index of 3 was chosen to improve subsequent calculations. The voxel dimensions of 2 mm x 2 mm x 2 mm were chosen as they are roughly equal to the average of PET and CT voxel sizes. For example, the Discovery MI PET/CT scanner voxel dimensions for CT are 1.4 mm x 1.4 mm x 2.8 mm and 2.7 mm x 2.7 mm x 2.8 mm for PET. Additionally, choosing voxels smaller than 2 mm would increase computation time and storage requirements.

Spherical Lesion Generation

Spherical lesions are generated as separate images that are then fused with the original phantom. The lesions are generated using the same parameters used for the phantom creation. Therefore, the lesions will be affected by the breathing motion according to the anatomical location in the phantom. The user choses the diameter of the lesion, and the x, y, and z pixel coordinates are selected from the phantom. To determine the dependence on lesion displacement within different lung regions, both the left and right lung were divided into five sections: Low, Low/Mid, Mid, Mid/Upper, and Upper. Each region, therefore, corresponds to 20% of the lung in the SI direction; for example, a low lesion corresponds to the lowest 20% of the lung, and an upper lesion corresponds to the top 20% of the lung. Figure 2.3 depicts the breakdown of the lung regions and shows sample lesions in the low and upper regions in the XCAT phantom.

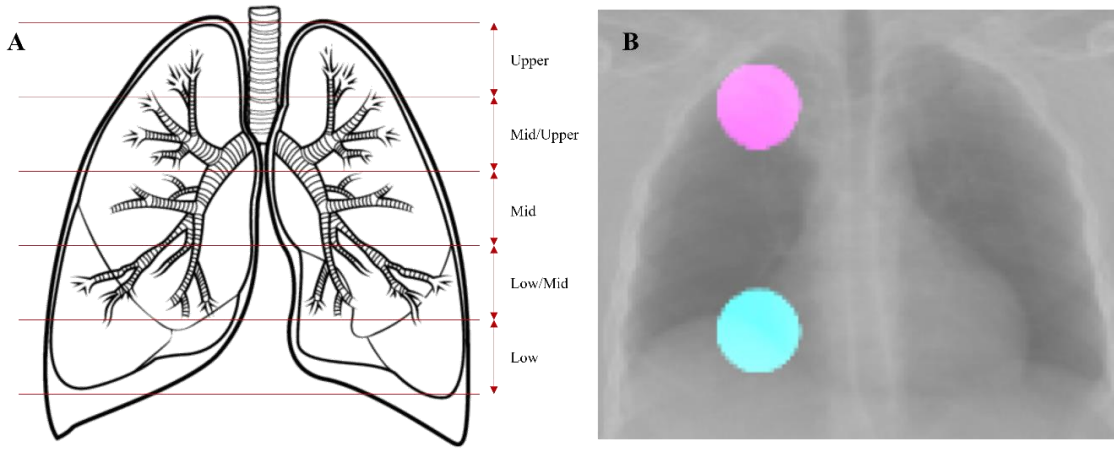

Figure 2.3 A) Division of the lungs into five different regions to assess the movement of lesions as a function of location and B) Sample low (cyan) and upper (magenta) 40 mm right lung lesions in the XCAT

In this work, 20 lesions were generated and underwent simulations for both the regular and deep breathing scenarios. Ten lesions were generated for each lung: five with 40 mm diameter and five with 50 mm diameter. Each simulation required a lesion placed in one of the five designated regions in either the left or right lung. This lesion would then undergo both normal and deep breathing simulations. Overall, 40 simulations tested

every combination of lung, lesion diameter, lesion location, and breathing scenario. Table 2.3 shows a sample of a single simulation and its parameters.

Lung	Region	Lesion Diameter	Breathing Scenario
Left	Low	40 mm	Normal

Table 2.3 Sample XCAT simulation with a spherical lesion.

The lesion placement within each of the five SI regions was generally consistent, with each lesion being placed posteriorly in the lung and close to the mediastinal region, as shown in Figure 2.4. In this region, contrast resolution with CT alone is likely poor due to nearby structures with similar attenuation coefficients as the lesion. Therefore, it is in areas such as these where the functional information provided by PET may be of the greatest utility.

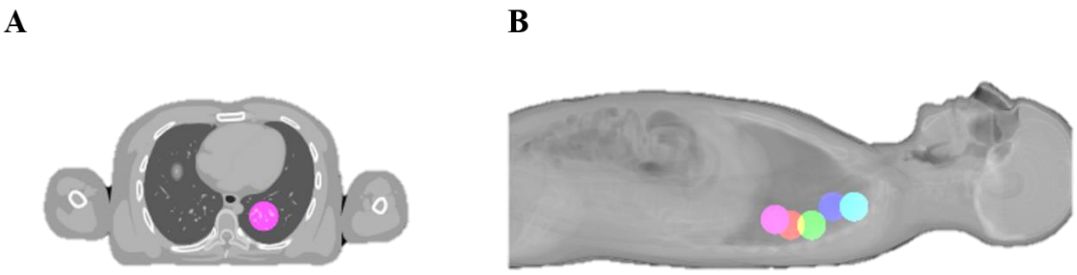

Figure 2.4 Sample image showing locations of lesions in the left lung. Image A shows a transverse slice, and image B shows the 3D volume with the location of each 40 mm lesion.

2.1.2 ImageJ Analysis

ImageJ[58] was used to determine the displacement of the lesion throughout the respiratory cycle. First, the phantom and image sets from one inhalation stage are imported into ImageJ. Then, three different image sets were merged using the Merge Channels feature: the phantom, the 0% inhalation stage of the lesion, and one of the 22%, 44%, 66%, and 88% inhalation stages. This feature creates a composite of each respective plane of the two image sets. Each of the stages was colour-coded to keep a clear distinction between the 0% inhalation lesion, the higher inhalation stage lesion, and the overlap area. The slices were then stacked to create a 3D volume using the 3D Project feature in ImageJ.

The displacement of the higher inhalation stage lesion from the original location during full exhale could be measured in the superior-inferior, anterior-posterior, and left-right dimensions using the voxel dimensions, as outlined in Figure 2.5.

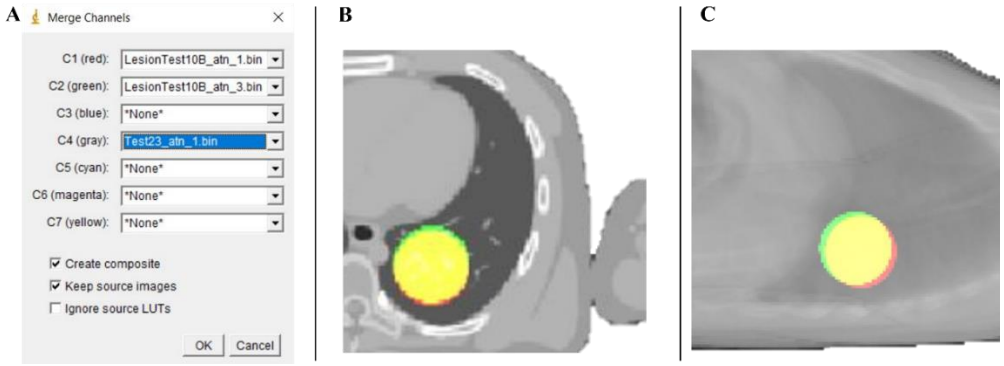

Figure 2.5 ImageJ analysis procedure of a 50 mm lesion in the lower left lung. Red regions of the lesion correspond to the full exhale position, and the green region corresponds to the lesion position at 66% inhale. The yellow region is the overlap of the two positions.

In addition to recording displacements in the AP, SI, and LR directions, the magnitude of the vector defining the motion of a lesion in three dimensions, v, could be calculated as

$$v = \sqrt{dAP^2 + dSI^2 + dLR^2} \quad \textbf{6}$$

where dAP, dSI, and dLR are the displacements in the AP, SI, and LR directions.[59] The purpose of calculating this metric is to translate XCAT findings to experiments with physical phantoms. Unlike the XCAT, the physical phantom movement is limited by the one-dimensional movement of the moving platform. Since AP, SI, and LR motion cannot all be translated to the moving platform, calculating the magnitude of the XCAT lesion displacement vector provides us with a one-dimensional value that could be a realistic parameter for the physical phantom displacement.

After displacement analysis, a series of maximum intensity projection image sets were created to simulate the treatment planning procedure at the JCC. The MIP equivalent images were denoted as MIP 44%, MIP 66%, and MIP 88%. Each of the MIPs resulted from the addition of two image sets: the 0% inhale image set and either the 44%, 66%, or 88% inhale image sets. For example, MIP 44% results from the addition of the

0% inhale image set and the 44% inhale image set. At the JCC, the MIPs are created on the summation of all phases to represent the entire lesion excursion.

In this work we created three different MIP images to observe differences in total volume encompassed by a lesion at multiple points in the respiratory cycle. If a patient's breathing is inconsistent in that it is either deeper or shallower than on average, multiple MIPs can estimate the difference in healthy tissue that may be irradiated. For example, a MIP created at 44% of a maximum inhalation of the XCAT phantom could best represent tumor motion in a patient with shallow breathing. If this patient occasionally breathed deeply, a MIP representing 88% maximum inhalation may be more representative of a tumor's entire excursion. The XCAT generated the average lesion image set to represent the equivalent of an average CT (UnTagged) image and it was not further manipulated. This averaged image is generated with 10 static image sets over a 5-second respiratory cycle. The average and MIP images were saved as Analyze files and the software AMIDE was used to evaluate lesion volumes.

2.1.3 AMIDE Analysis

The XCAT outputs volumes of lesions generated during each inhalation phase, however it cannot calculate volumes for the MIP image sets since they are constructed manually. To assess the effects of respiratory motion on the apparent lesion volumes for these image sets, the program AMIDE was used. AMIDE is a free, open-source medical image data examiner with several useful features including displaying multiple data sets and creating regions-of-interest for volumetric measurements.[60] An outline of the volume calculation procedure is shown in Figure 2.6. Note that the apparent lesion volume describes lesion volumes calculated from an image set and can differ from the true lesion volume. The deep breathing phantom was generated as described in Section 2.1.1, with a maximum diaphragm motion of 3 cm and maximum AP chest expansion of 1.8 cm.

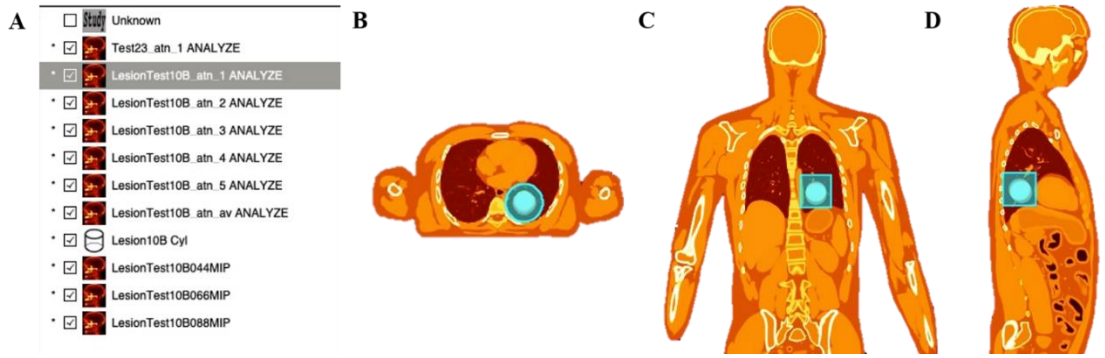

Figure 2.6 AMIDE analysis process for volumetric measurements. A) data set menu B) transverse view C) coronal view D) sagittal view of phantom with lower left lung lesion. Teal-coloured elliptical cylinder is a custom ROI that encompasses lesion volume.

Lesion volumes were calculated from the 0%, 22%, 44%, 66%, and 88% inhalation phases, the average lesion image set, and MIP 44%, MIP 66% and MIP 88% image sets. To complete these calculations, an elliptical cylinder ROI that encompassed the entire lesion volume was created. Since AMIDE calculates the volume for each data set individually, the voxel intensities from the phantom do not contribute to the lesion volume since the lesions are generated in a separate simulation. The subsequent volume calculation does not calculate the volume of the elliptical cylinder, but rather only voxels above a predefined threshold. The only voxels with nonzero values here are those belonging to the lesion and therefore means the lesion volume can be calculated accurately despite an elliptical ROI that is not completely conformal. Initial volume calculations on AMIDE set to calculate voxels with values above 0 yielded lesion volumes that exceeded the lesion volumes shown in the output log of XCAT simulations at each inhalation phase. This is likely because AMIDE completes calculations based on voxel intensities, whereas XCAT volume calculations are calculated independent of the voxel. To solve this discrepancy in the AMIDE application, a threshold was introduced to consider only voxels with an intensity value above 0.015 in the volume calculation. This resulted in an agreement of 0.2% between the XCAT volumes for single inhalation phases and AMIDE volumes.

2.2 CTN Physical Phantom

The physical phantom used for this project was the oncology simulator PET/CT phantom created by the Clinical Trials Network of the Society of Nuclear Medicine and Molecular Imaging.[50] The phantom was placed on a moving platform to simulate a linear respiratory motion and scanned using the Discovery MI hybrid PET/CT scanner by General Electric. Users can adjust the platform oscillation between 1, 2, and 3 cm motion in the SI direction and the period of oscillation. The platform is shown in Figure 2.7.

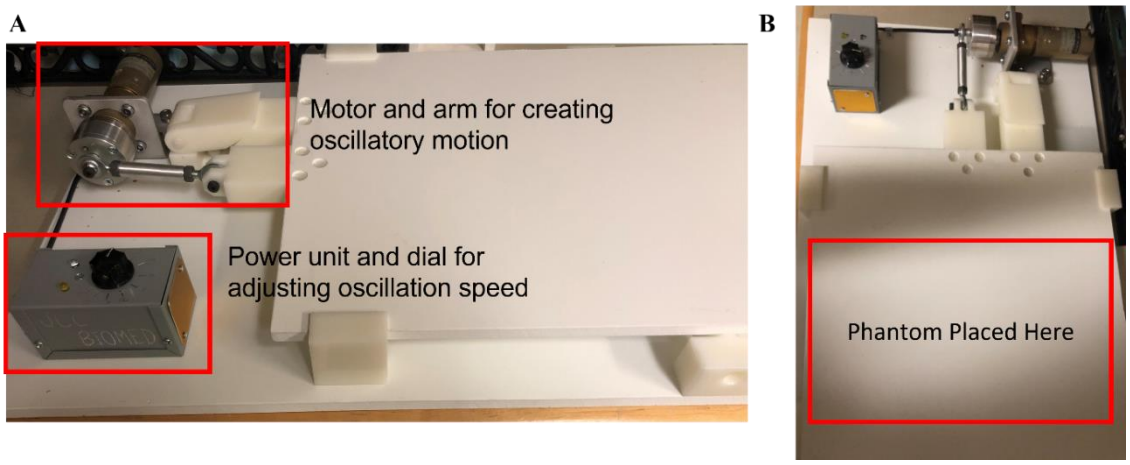

Figure 2.7 An A) full view and B) overhead view of the moving platform used to simulate respiratory motion.

The CTN phantom, shown in Figure 2.8, is an anthropomorphic chest phantom with two heterogenous lungs. The phantom contains spherical lesions ranging from 7 mm to 37 mm in diameter, some of which are placed in the lung and others in homogenous regions. The movement of spherical inserts in an inhomogeneous environment can challenge automated segmentation algorithms such as PET EDGE, making insert borders less distinct.

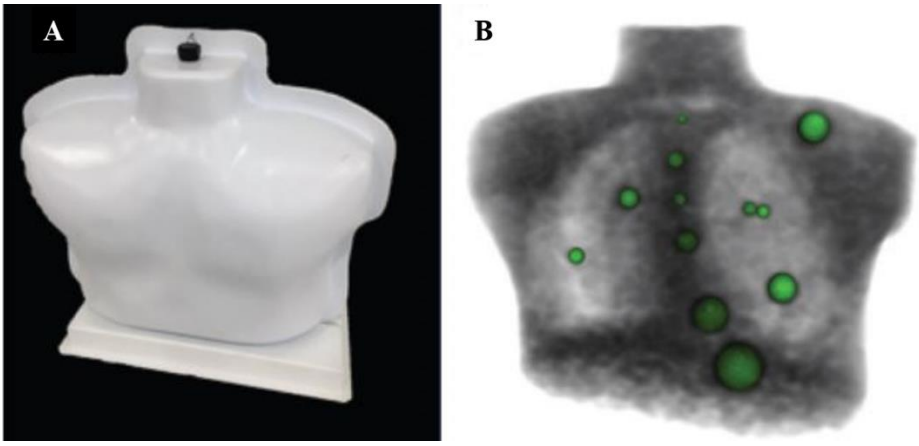

Figure 2.8 The clinical trials network phantom showing A) an external view and B) an internal view with lesions highlighted in green.[61]

2.2.1 PET/CT of CTN Phantom

The CTN phantom was scanned twice using the PET/CT scanner at SJHH. First, a static image was acquired, followed by the dynamic image where the phantom was placed on a platform oscillating at 2 cm continuously in the SI direction. A fluorine-18 dose of 15 mCi and 14.81 mCi, respectively, was administered to the phantom for the static and dynamic imaging procedures. The 2 cm oscillation corresponds to a deep breathing patient.

After the imaging procedure, the scans were analyzed using the software MIM Maestro Version 7.0.3. The static and dynamic techniques resulted in three image sets: CT only, PET with attenuation correction, and a fused PET/CT image. The gradient-based automated segmentation algorithm PET EDGE created regions-of-interest (ROIs) on fused PET/CT images for three separate lesions. This gradient-based ASA calculated tumor borders based on the rate-of-change of the standardized uptake value (SUV) in a PET image, as discussed in Section 1.3.3. The lesions chosen for contouring were the 37 mm lesion in the lower abdomen, the 22 mm lesion in the upper left shoulder, and the 22 mm lesion in the left lung. The ROIs were created on both the static and dynamic image sets to determine the accuracy of volume determination using this technique. The diameter and volume of each ROI were calculated separately and compared to the known sphere dimensions and between static and dynamic image sets.

2.3 3D-Printed Irregular Lesion

In addition, a 3D-printed model of an irregular lesion was created and imaged. This irregular lesion provides two advantages over conventional, regular shapes found within the CTN phantom. First, real lung lesions do not typically conform to regular shapes and second, an irregular shape provides a greater challenge for segmentation algorithms.

2.3.1 Creation and Specifications of the Irregular Lesion

The lesion was designed using Blender Version 2.93[62] and printed using an Ultimaker 2+ 3D printer. A hollow design was chosen to be filled with water for CT experiments and 18-FDG solution for PET studies. The lesion could not be produced in a single piece as the Ultimaker printer needed to generate internal support structures during printing. These support structures are irremovable and decrease the volume of liquid that could be added to the lesion. To solve this problem, the lesion was printed in two halves which were then glued together and sealed with a liquid rubber sealant. The design from Blender, the printed product, and the final sealed are shown in Figure 2.9.

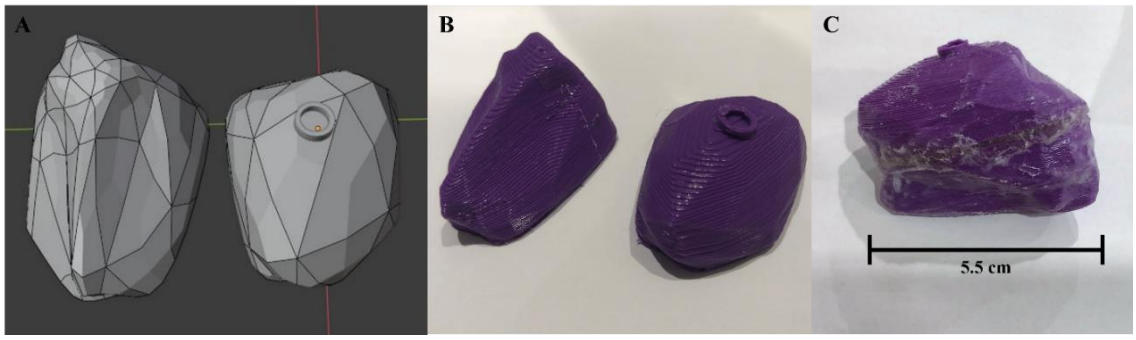

Figure 2.9 Development of 3D printed irregular lesion showing A) pre-print design in Blender B) initial print job and C) sealed, hollow lesion on a support structure.

Due to its irregular shape, the external volume of the 3D printed lesion was determined using the water displacement method. First, 125.0 ml of water was measured using a graduated cylinder with an uncertainty rating of ± 1 ml per 100 ml at a water temperature of 20 °C. This water was then poured into a beaker where the hollow lesion was submerged. The elevated water meniscus was marked and, after removing the lesion, water was added until the volume reached the marked meniscus level. The now greater

volume of water was measured using the same graduated cylinder and was determined to be approximately 172.1 ml. Accounting for the propagation of errors as water was measured in the graduated cylinder, the external volume of the lesion was determined to be approximately 47.1 ± 3.0 ml. By filling the lesion with water, the internal volume was found to be 32.0 ± 0.3 mL.

2.3.2 4DCT of Irregular Lesion

The lesion was first filled with water and submerged in approximately 800 mL of aloe gel before scanning. The gel was chosen to approximate the attenuation coefficient of water and act as a suspension medium for the lesion. The container was then placed on the same dynamic platform used for the CTN phantom experiment. Radiopaque beads were placed on the container to assist with alignment, ensure reproducibility for future scans, and as a reference on CT images. A photo of the setup is shown in Figure 2.10.

Figure 2.10 4DCT setup for imaging of irregular lesion. Note the device highlighted by the red square is the reflective block of the Varian Real-Time Position Management Respiratory Gating System. This device tracked the oscillation of the moving platform for the temporal component of 4DCT.

Images were acquired on a Siemens SOMATOM Definition AS using the 4DCT chest imaging protocol. The moving platform oscillation period was set to 5 seconds to simulate an average respiratory rate, with oscillation being tracked through the Varian

Real-Time Position Management Respiratory Gating System. In total, 10 binned image sets were acquired to generate an average image set and MIP for both 1 cm and 2 cm platform oscillations.

Analysis was completed using the MIM Maestro software package. The 2D brush tool created ITV contours on a static image set, 1 cm MIP, and 2 cm MIP. Due to the hollow nature of the lesion, both external and internal volumes were contoured. Internal volumes will be compared with volumes generated by contouring PET images. To accurately contour ITVs based on the internal volume in the presence of motion blurring on MIPs, the external contour was contracted by 0.3 cm as this was the thickness of the lesion walls measured on CT. The volumes of three internal ITV contours were then compared.

2.3.3 PET/CT of Irregular Lesion

The PET/CT data acquisition took place at St. Joseph's Healthcare Hamilton using GE's Discovery MI PET/CT scanner. The 32 mL internal volume of the lesion was filled with 1.8 MBq of 18-FDG immediately before imaging and then submerged in the same container used with the 4DCT scan. Effort was made to ensure comparable orientation in the gel by comparing to external markers and photos taken during the 4DCT scan setup. No background radiotracer was introduced to the gel. Following the procedure for chest imaging, three separate scans were acquired: static, 1 cm dynamic oscillation, and 2 cm dynamic oscillation. These are the same imaging scenarios used for 4DCT, and the oscillation period of the moving platform remained at 5 seconds. Although patient imaging is usually done with a curved couch, the phantom here was placed on a flat pallet. Again, all movement was in the SI direction as the moving platform could not replicate AP and LR motion. The PET scanner required two minutes of detection time to generate an image with a field of view of approximately 25 cm. As with the CTN phantom, each imaging scenario resulted in three image sets: CT only, PET, and a fused PET/CT image. An image of the phantom setup is shown in Figure 2.11.

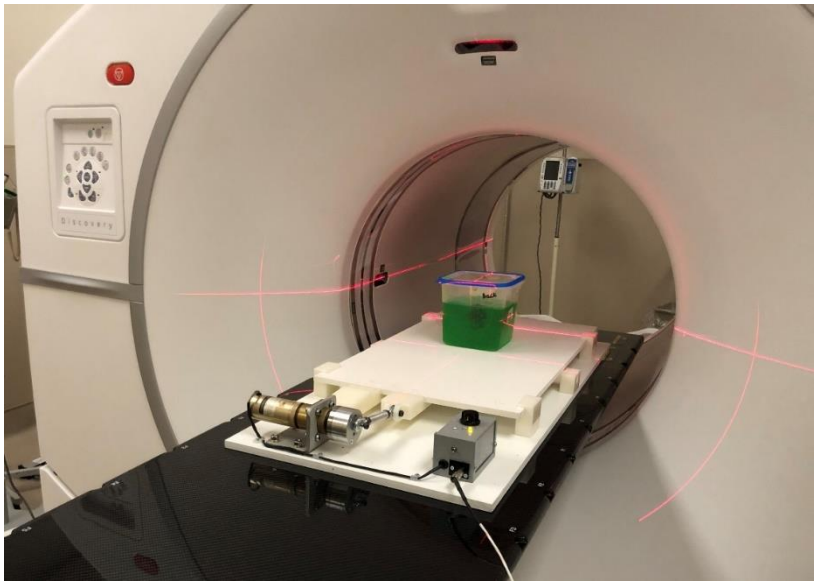

Figure 2.11 PET/CT setup of irregular lesion scan

2.3.4 Fused PET/4DCT of Irregular Lesion

Static and dynamic PET images were fused with their corresponding static and dynamic 4DCT images using two different methods on MIM Maestro: rigid image registration (RIR), and deformable image registration (DIR). Rigid and deformable image registration was done using the *4D CT – Max IP and Avg IP – Optional Diagnostic PET/CT Registration* automated workflow on MIM. This requires the user first to assign diagnostic CT, diagnostic PET, planning CT, and 4DCT images. Here, the planning CT was the MIP and the 4DCT images were the individual binned phases. The program first rigidly fused the diagnostic CT to the planning CT image. MIM rigidly registers images through the maximization of the mutual information (MI) metric. This metric is based on overlapping voxels of similar intensities between the two images and involves calculations of joint entropy between volumes. Since MIM is commercial software, specific details about its algorithms are not readily available; however, the general mathematical discussion about mutual information and joint entropy can be discussed. First, assume there are two random variables, A and B, with marginal probability distributions $p_A(a)$ and $p_B(b)$. Their individual entropies are then $H(A)$ and $H(B)$ and their joint entropy is expressed as $H(A,B)$.[63]

$$H(A) = -\sum_{a} p_A(a) \log p_A(a) \quad \textbf{7}$$

$$H(B) = -\sum_{b} p_B(b) \log p_B(b) \quad \textbf{8}$$

$$H(A,B) = -\sum_{a,b} p_{A,B}(a,b) \log p_{A,B}(a,b) \quad \textbf{9}$$

The MI is then

$$I(A,B) = H(A) + H(B) - H(A,B) \quad \textbf{10}$$

MIM rigidly fuses two images through an algorithm that completes a series of rotations and translations until MI is maximized.[64]

Upon manual verification of the registration, the diagnostic PET is then propagated to the planning CT. In this work, the option to create a deformable image registration was selected even after a successful rigid registration to test the functionality of the DIR algorithm. The VoxAlign Deformation Engine® by MIM requires first a rigidly fused image and uses freeform transformation and a multi-resolution approach.[65,66] Using the multi-resolution approach, the algorithm starts at a course resolution to account for gross differences from the rigid registration. The resolution is then continually increased to look at smaller local differences. This method allows for accurate deformation of larger anatomical discrepancies, such as a patient that is positioned with arms by their side for one image and with their arms above their head for the second.[65] Unlike the rigid registration algorithm that uses mutual information as a metric to evaluate the accuracy of registration, the DIR algorithm uses an intensity-based sum of squared difference metric.[66] Minimization of this method indicates better performance. Once an initial deformed image is created, the RegRefine® tool is used to evaluate the quality of the deformation and create new conditions for additional attempts at DIR. Here, a window can be adjusted which allows the user to view both the primary and secondary data sets after the initial rigid registration. This original rigid registration can then be manipulated and links between the primary and secondary images can be "locked" and used as a new initial condition in the subsequent deformation attempt. By

providing these locked points, the following deformable registrations can be improved. This process is repeated until the user determines that the deformed image is acceptable.[66]

After image fusion, PET EDGE was used to create ten ROIs on both the RIR and DIR images. To generate these contours, the user defines a starting point near the center of the lesion and extends this point to the border to provide a starting point for the algorithm. As the point extends, multiple axes are produces that define an ellipsoid as the initial bounded area. If the tumor is not an ellipsoid, the above technique is repeated multiple times by adding to the initial contour. As previously mentioned, this gradient-based algorithm calculates spatial derivatives along the tumor boundary and determines the tumor edge based on both the derivatives and continuity of the edge.[44] The average volume from these ROIs was compared to both the known internal volume of the lesion and the volume determined from 4DCT contouring. Dice similarity coefficients (DSC) were calculated to compare each of the ROIs to the ITV volume created on the 4DCT. Each fusion technique was compared to determine the optimal workflow for accurately fusing PET to 4D planning CT and delineating internal target volumes. The DSC is given by the expression

$$D = \frac{2 * \ |X| \cap |Y|}{|X| + |Y|} \qquad \textbf{11}$$

where X and Y are two separate data sets, or in this case, ROIs. The DSC's values range between 0 and 1, where 1 indicates complete overlap between two ROIs and 0 represents zero overlap. Thus, higher Dice similarity coefficient values demonstrate high similarity and lower DSCs indicate low similarity.

3 Results and Discussion

3.1 XCAT Digital Phantom Results

XCAT simulations allowed for quantifying the effects of respiratory motion on lung lesion displacement for both normal and deep breathing amplitudes in the SI, AP, and LR directions. It also allowed for demonstration of lesion motion effects on the average image (UnTagged) used for contouring organs-at-risk and MIP images used to create the ITV in radiotherapy.

3.1.1 Lesion Displacement

Displacements of lesions in the AP, SI, and LR directions were measured using ImageJ as described in Section 2.1.2.

LR Displacement

A displacement in the left-right direction was only observed in a single lesion test. This is likely because the XCAT creators observed minimal to no lateral expansion of respiratory structures when studying clinical images.[56] In a study similar to this, Geramifar *et al*. also did not observe LR displacement in XCAT simulations and claimed it was due to negligible displacement.[67] Lung tumor motion has been shown to vary widely on an individual basis. Overall, lung tumors appear to move less in the LR direction than in the SI or AP directions. Displacement in the left-right direction has been reported as ranging between 0 mm and 13 mm, with greater mean displacements in the middle and lower regions of the lung.[27] The lack of lateral motion of spherical inserts may be considered a limitation of the XCAT.

SI & AP Displacement

Superior-inferior and anterior-posterior movements were observed for lesions throughout both lungs. Figure 3.1 compares normal and deep breathing lesion displacement in the SI direction for five different locations of 40 mm lesions in the right lung. Deep breathing caused increased displacements for low and low/mid lesions but did

not affect lesions in the upper 60% of the lung. The upper lesions showed no displacement for normal or deep breathing amplitudes.

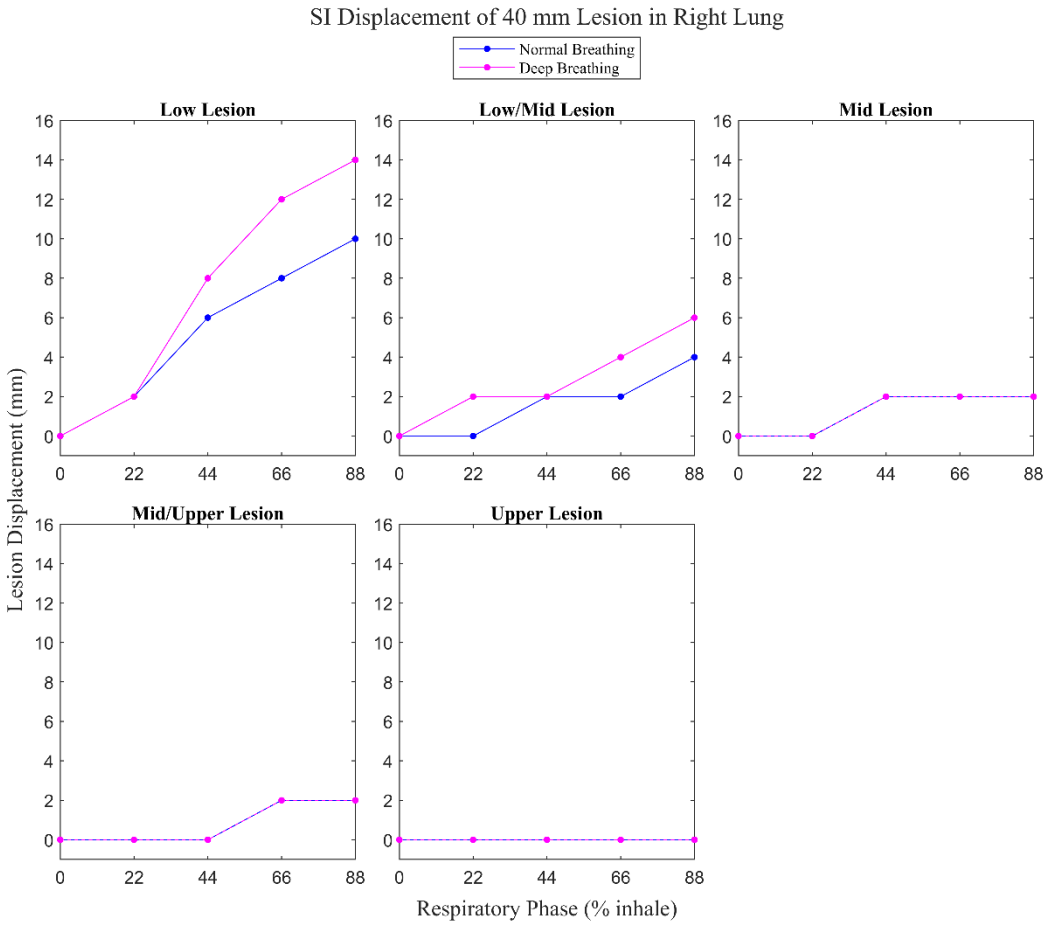

Figure 3.1 Plot showing the displacement of a 40 mm lesion from the full exhale position in the right lung as a function of the respiratory phase of the phantom. Data is shown for lesions in five separate locations, ranging from lower to upper lung regions.

Lesions in the left lung followed similar SI displacement trends but at reduced magnitude for both normal and deep breathing amplitudes. This is likely due to the presence of the heart, which reduces expansion volume for the left lung. Zero displacements were observed for upper lesions in the left lung as well. This data is displayed in Figure 3.2.

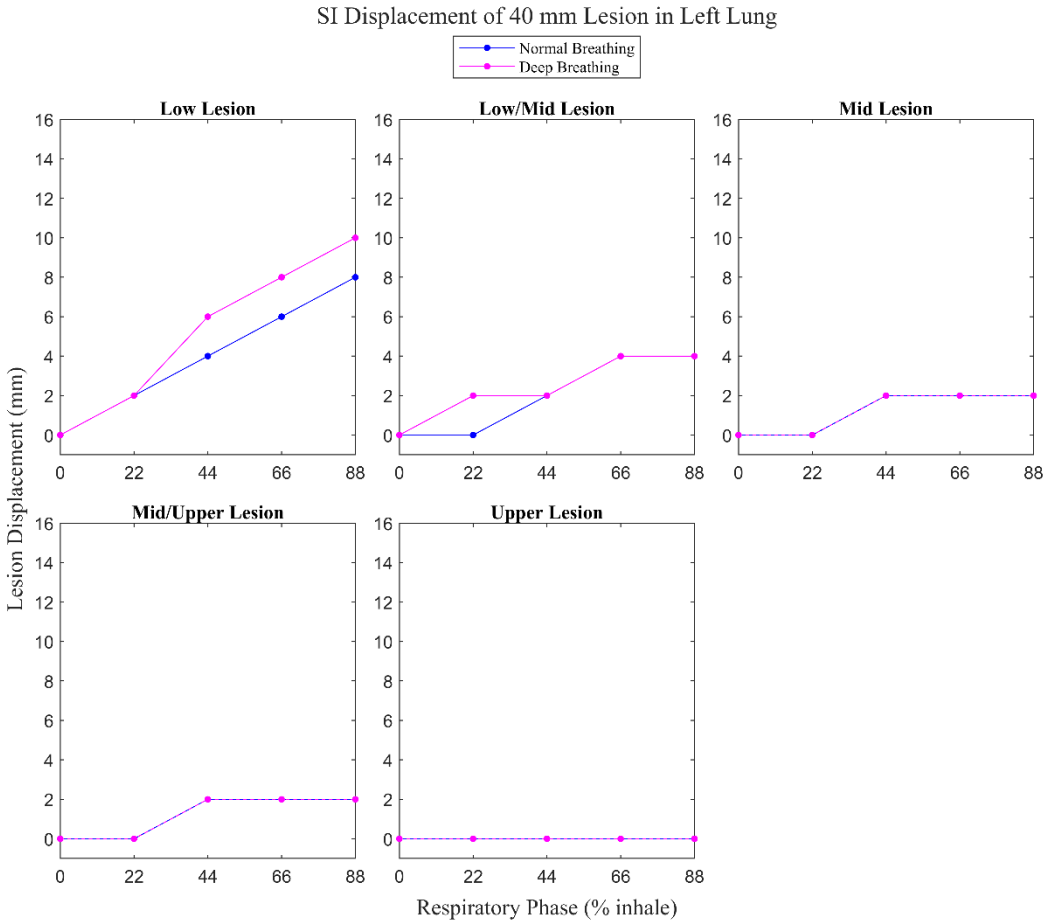

Figure 3.2 Plot showing the inferior displacement of a 40 mm lesion from the full exhale position in the left lung as a function of the respiratory phase of the phantom. Data is shown for lesions in five separate locations, ranging from lower to upper lung regions.

Displacements in the anterior-posterior direction are shown in Figure 3.3 for the right lung. Here, AP displacements follow similar trends as in the SI direction; namely, displacement is greatest for lesions placed lower in the lung and deep breathing increases movement. Nonzero displacements are observed in each lesion location. However, AP displacement is less dependent on location in the lung than SI displacement.

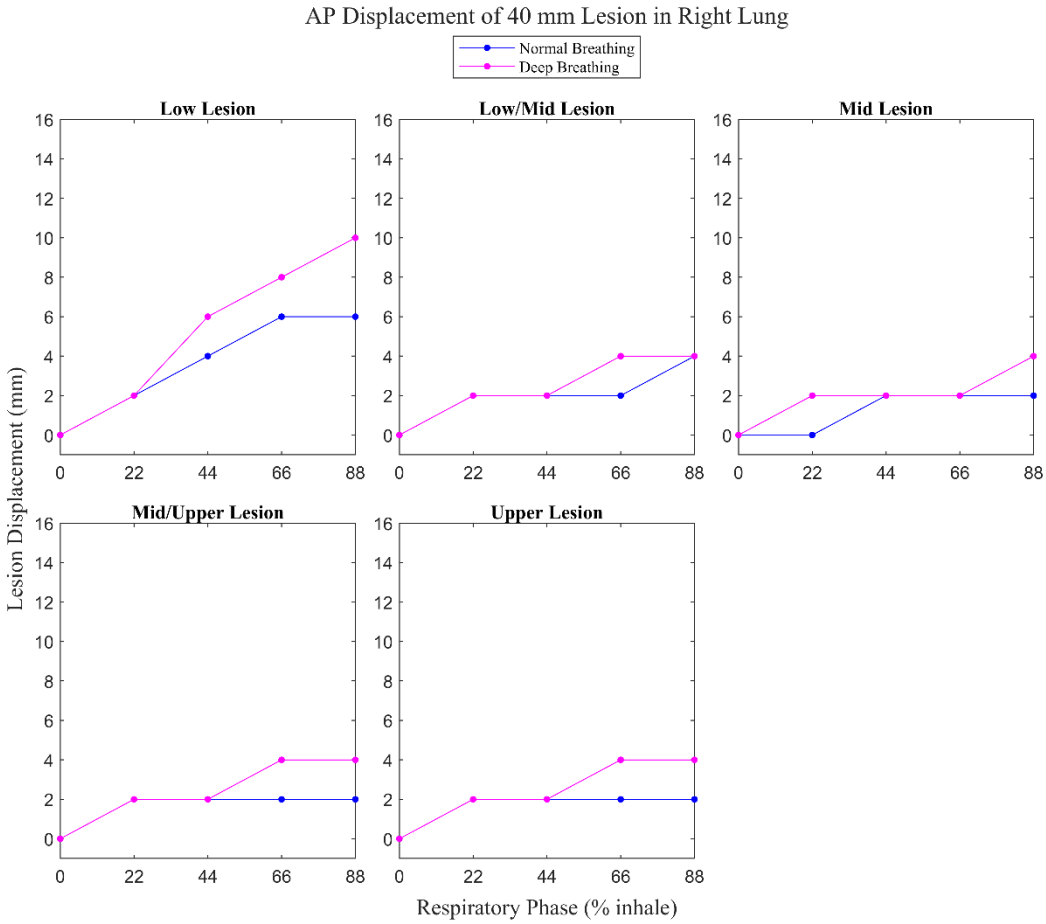

Figure 3.3 AP displacement of a 40 mm lesion from full exhale position in the right lung. Data is shown for lesions in five separate locations, ranging from lower to upper lung regions.

Left-lung lesions generally experienced reduced displacements in the AP direction compared to lesions in the right lung. This is the same trend seen with SI displacements, and is also likely due to the presence of the heart. Again, deep breathing resulted in increased displacement versus normal breathing amplitude. All lesions in the upper 80% of the lung experienced similar AP displacements, indicating the relative independence of lesion location. This data is shown in Figure 3.4.

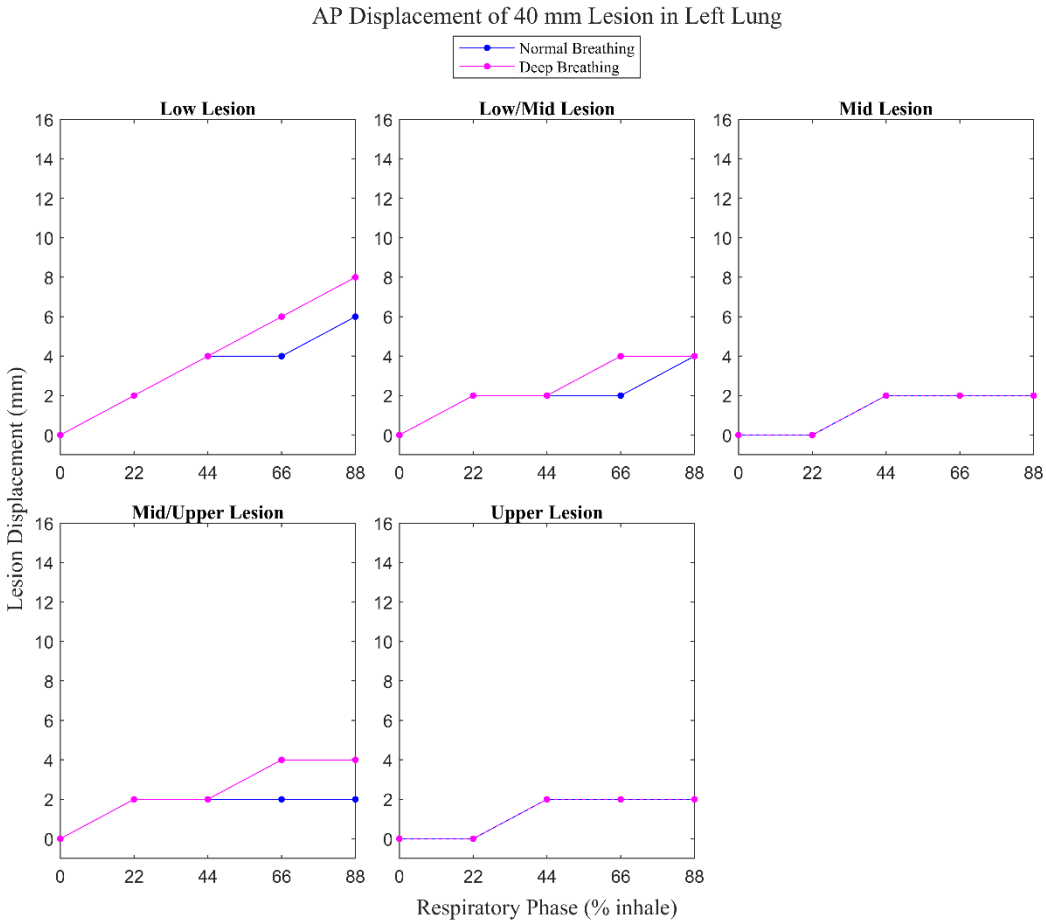

Figure 3.4 AP displacement of a 40 mm lesion from full exhale position in the left lung. Data is shown for lesions in five separate locations, ranging from lower to upper lung regions.

Figure 3.5 depicts the maximum displacement seen in the AP and SI directions across different locations in the right lung under normal and deep breathing conditions, respectively. As expected, these values correspond with the maximum inhalation phases generated by the XCAT. These graphs show that tumor location determines the degree of displacement experienced by a tumor. This is particularly evident in the SI direction, where displacement decreases by 10 mm from the lower to upper regions of the lung during normal breathing. During deep breathing, this difference between the lower to upper regions of the lung is 14 mm. The AP displacement is less dependent of tumor location. The displacement decreases by 4 mm from the lower to upper regions of the

lung for normal breathing, whereas the AP displacement decreases by 6 mm from the lower to upper lung regions during deep breathing.

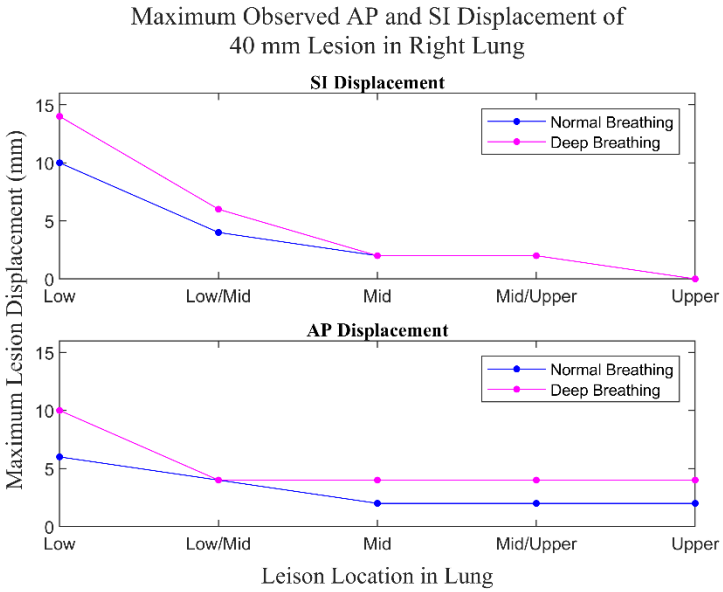

Figure 3.5 Maximum displacement from full exhale position observed in the SI and AP directions of 40 mm lesions across five different locations in the right lung.

There are fewer differences between maximum AP and SI displacement in the left lung, as shown in Figure 3.6. Differences between normal and deep breathing are also diminished when compared to the right lung. Overall, this data suggests that lesions in the right lung are more susceptible to respiratory motion than lesions in the left lung.

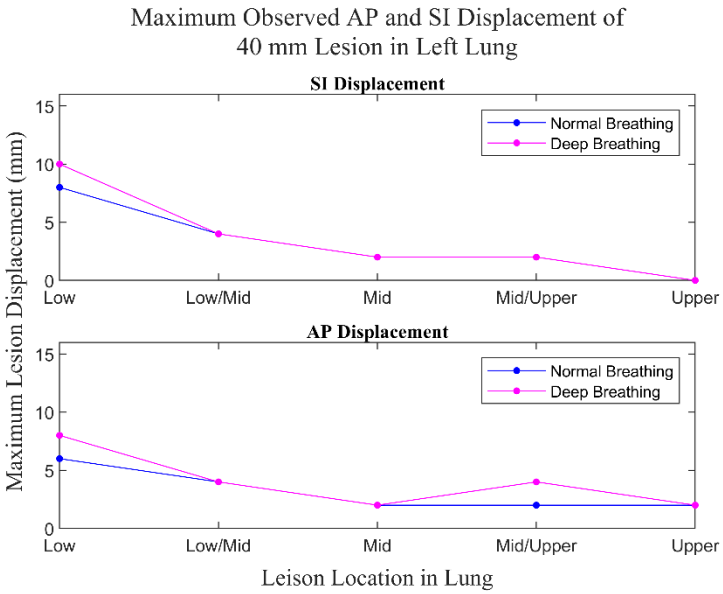

Figure 3.6 Maximum displacement from full exhale position observed in the SI and AP directions of 40 mm lesions across five different locations in the left lung.

Simulations were repeated with lesion diameters being increased from 40 mm to 50 mm. Apart from the overall decrease in displacement with a 50 mm lesion, the trends mirror the results from the 40 mm lesion tests. The decrease in displacement suggests that large lesions will experience less displacement, whereas smaller lesions will have larger displacements. The corresponding figures for the 50 mm lesion can be found in Appendix A.

Figures 3.7 and 3.8 include displacement data across all respiratory cycles for both 40 mm and 50 mm lesions. The boxplots show that the lowest placed lesions experienced the largest motion overall. The median SI displacement in a low lesion during normal and deep breathing was 6 mm and 8 mm, respectively. Median values for low/mid, mid, mid/upper, and upper lesions were equal for the normal and deep breathing simulations. Median AP displacements in a low lesion during normal and deep breathing were 4 mm and 5 mm, respectively. For both normal and deep breathing, the median displacement values were equal at all other lesion locations. However, larger displacements were observed in the deep breathing simulation.

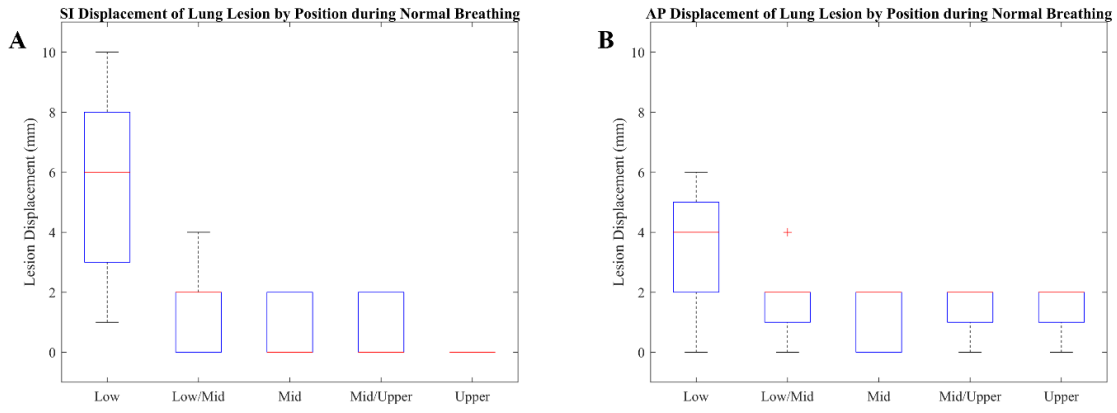

Figure 3.7 Combined data for A) SI and B) AP displacement across all respiratory phases for both 40 mm and 50 mm lesion during normal breathing. The red line represents the median value, the blue box represents the 25th-75th quartile values, the red cross represents outlier values and the black line shows the range of data.

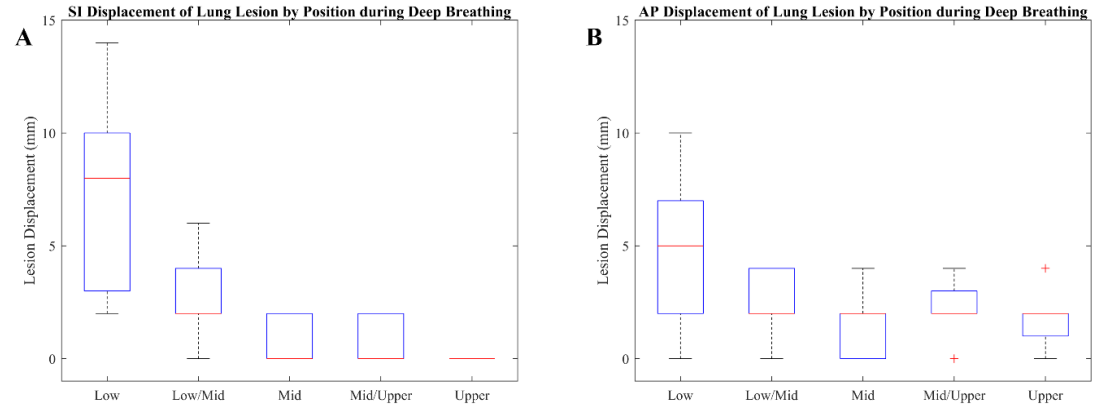

Figure 3.8 Combined data for A) SI and B) AP displacement across all respiratory phases for both 40 mm and 50 mm lesion during deep breathing. The red line represents the median value, the blue box represents 25th-75th quartile values, the red cross represents outlier values and the black line shows the range of data.

Overall, results from the XCAT simulations show that lesion displacement in the SI direction is highly dependent on the vertical tumor location in the lung, ranging from 14 mm inferior displacement in the lower lung to no displacement for lesions in the upper lung. AP displacement does not vary according to vertical tumor location to the same magnitude as SI displacement, however lower lesions do show more than double the displacement than lesions in the upper 60% of the lung during normal and deep breathing. As expected, the greatest displacements were observed at the highest

respiratory phase of 88% inhalation. Lesions in the mid to upper regions often showed no increase in displacement in either the AP or SI directions at inhalation phases below 44%. This suggests that towards later inhalation phases, the largest lesion movements occur in the lower portions of the lungs. Table 3.1 shows data from three studies cited by AAPM Task Group 76 in which the authors determined lung tumor motion in SI, AP, and LR dimensions.[27]

Study	Number of Patients	Mean SI Displacement (mm)	Mean AP Displacement (mm)	Mean LR Displacement (mm)
Seppenwoolde et al.[68]	20	5.8 (0-25)	2.5 (0-8)	1.5 (0-3)
Ekberg et al.[69]	20	3.9 (0-12)	2.4 (0-5)	2.4 (0-5)
Erridge et al.[70]	25	12.5 (6-34)	9.4 (5-22)	7.3 (3-12)
XCAT Normal Breathing	20	2.7 (0-10)	2.9 (2-6)	0 (0-0)
XCAT Deep Breathing	20	3.5 (0-14)	4 (2-10)	0 (0-2)

Table 3.1 Mean lung tumor-motion in SI, AP, and LR dimensions and (minimum-maximum) values across three studies with different patient cohorts.

As evident from Table 3.1, there exists significant variation in the degree of tumor motion between patients. The displacement values from the XCAT simulations are most similar to the results by Seppenwoolde *et al*. and Ekberg *et al*. when omitting movement in the left-right dimension. The mean tumor diameter in the study by Ekbert *et al*. was 47 mm, which could be reason for the general agreement with the 40 mm and 50 mm lesions simulated in this project. Although the upper range of displacement found in the study by Seppenwoolde *et al*. was 25 mm, more than double any displacement value found in the XCAT during normal breathing. The second-highest displacement value was 13.1 mm which is approximately equal to the SI displacement of the 40 mm lesion during deep breathing. Relatively large differences in displacements between XCAT simulations and results from Erridge *et al*. may be explained by differences in lesion sizes. In the study by Erridge, 40% of patients had stage I lung cancer, corresponding to maximum lesion diameters of 30 mm. These smaller lesions likely experienced larger displacements than

the 40- and 50-mm lesions in XCAT simulations. For all three studies, the largest displacement was recorded in the SI direction.

In contrast with XCAT simulations, the three studies found a higher mean displacement in the SI direction than in the AP or LR directions. In addition, two of the three studies specified that tumors located in the lower or middle of the lung experienced more displacement than those in the upper lung, as found with the XCAT.[68,70] Based on the larger displacement of the 40 mm lesion compared to the 50 mm lesion and the effects of location, it can be reasonably presumed that smaller lesions located lower in the lung will experience greater displacement, predominantly in the SI direction.

The magnitude of the vector defined by the motion in the AP, SI, and LR dimensions provides additional insight into the displacement of lesions, as described in Section 2.1.2. Figures 3.9 and 3.10 show the vector displacement of 40 mm lesions during normal and deep breathing in the right and left lungs, respectively. The results suggest that a lesion will likely be displaced less than 1 cm due to respiratory motion unless the lesion is in the bottom 20% of the lung. Data for 50 mm lesions show mirrored trends and can be found in Appendix A.

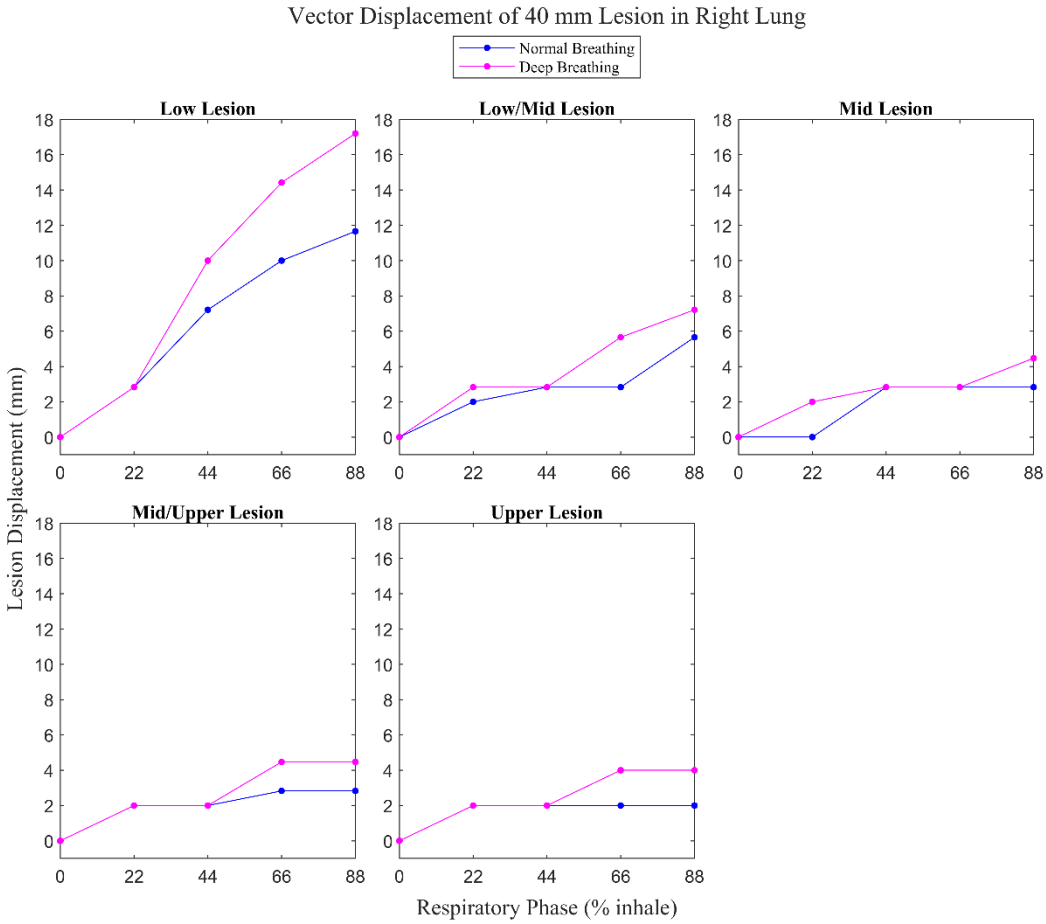

Figure 3.9 Vector displacements of 40 mm lesions in the right lung as a function of the respiratory phase.

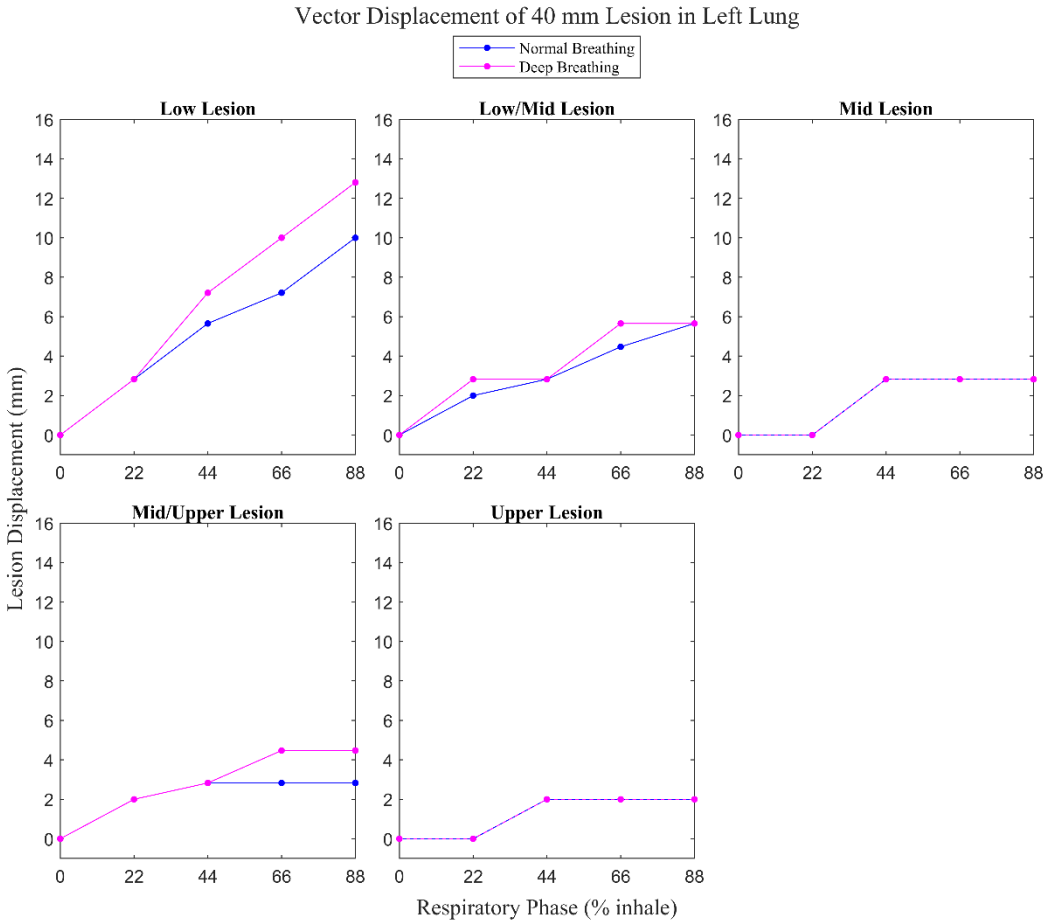

Figure 3.10 Vector displacements of 40 mm lesions in the left lung as a function of respiratory phase.

The moving platform used with the physical phantoms can oscillate 1-, 2-, and 3-cm in the SI direction. The XCAT simulations generally agree with the literature and demonstrate that lesions will not experience a displacement larger than 1 cm unless they are located in the lower 20% of either lung and are 40-50 mm or smaller in diameter. A choice of 1 cm of oscillation for the moving platform provides a realistic simulation of breathing motion for a physical phantom that is limited to movement in one dimension. A 2-cm oscillation can be useful to simulate patients with deep breathing and lesions approximately 40 mm in diameter or less.

3.1.2 Lesion Volumes

From the XCAT simulations, the location of a lesion and the inhalation stage at which an image is generated can significantly influence the determination of lesion volume to be irradiated in radiotherapy (RT) treatment planning (TP). Therefore, it is important to quantify how tumor displacement can lead to a larger ITV. Figure 3.11 shows a visual example comparing volumes of an average image and MIPs at 44%, 66%, and 88% inhale generated using the XCAT phantom.

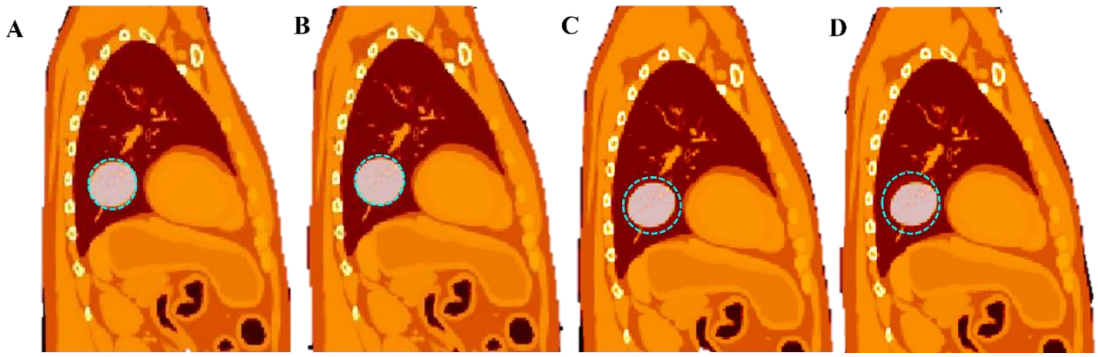

Figure 3.11 Sagittal view of a lesion in the lower left lung with image types A) Average B) MIP 44% C) MIP 66% and D) MIP 88%. ROI contours are shown in cyan.

The volume of a perfectly spherical lesion with a radius of 20 mm equals approximately 33.5 mL. Given that each XCAT image set is generated over 0.5 seconds, the volume output by the XCAT for a spherical lesion in a single image set is slightly larger due to motion during the 0.5 s period. Because of this, the XCAT calculated the average volume for the sphere across a static image set to be 35.3 ± 0.1 mL during normal breathing. Given that the temporal resolution of a 4DCT image set is approximately equal to that of the XCAT, it is reasonable to compare this value to calculated average and MIP volumes. Furthermore, comparisons can be made between average XCAT image sets and images generated on ungated PET/CT. During PET imaging, the patient is breathing freely throughout the several-minute acquisition time. This generates an image set that shows the average distribution of the radiotracer during multiple breathing cycles. Therefore, ITV volumes calculated from an average XCAT image set should reflect the volumes obtained from a PET scan.

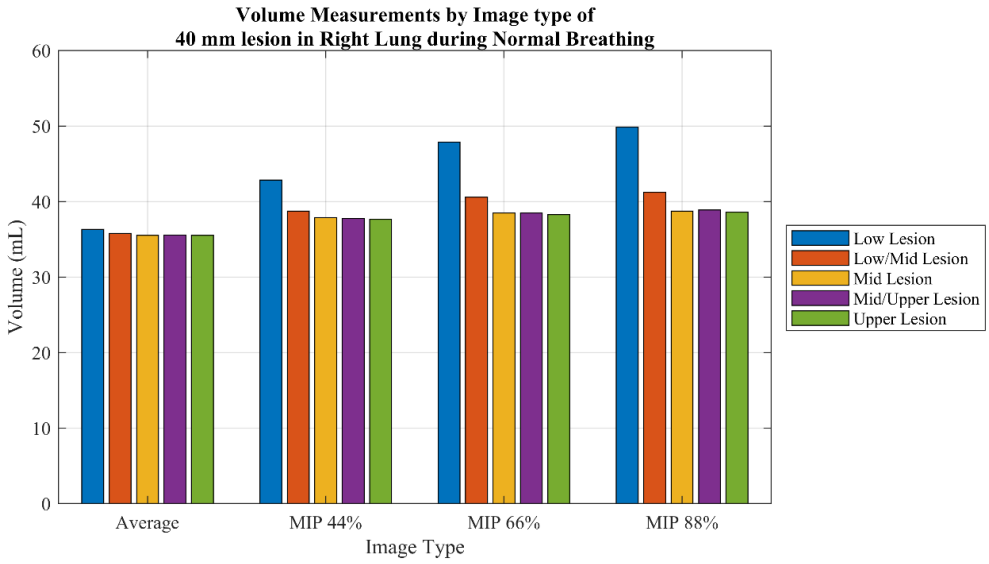

Figure 3.12 Average and MIP image set volume measurements for a 40 mm lesion in the right lung during normal breathing.

As shown by Figure 3.12, an image of a 40 mm lesion in the right lung averaged over an entire respiratory cycle will result in a calculated volume slightly larger than the volume calculated using a static image set. There is a significant increase in volume for lesions in the lowest 20% of the lung. Here, the lesion volume calculated for the MIP 88% image set is 49.8 mL compared to 36.3 mL in the average image set. Since the MIP 88% image set would be used to create an ITV there is a 37% increase in the irradiation volume for this situation compared with the average image set. However, lesions in the upper 60% of the lung show less increase in the potential irradiated volume. A mid-right lung lesion, for example, shows a volume increase of 9% between an average image set and MIP at 88% inhale.

Deep breathing results in an increase in apparent volumes, which corresponds to an increased ITV size in RT-TP, for all average and MIP image sets when compared to normal breathing. The increase in volume is significant for lesions in the lower 20% of the right lung, with volume increasing by 55% between the average and MIP 88% image sets, compared to an 11% increase when comparing the same image types for a mid-right lung lesion. These results are displayed in Figure 3.13, and indicate that low lesions, for

example, were 12% larger during deep breathing than normal breathing for the MIP 88% image set.

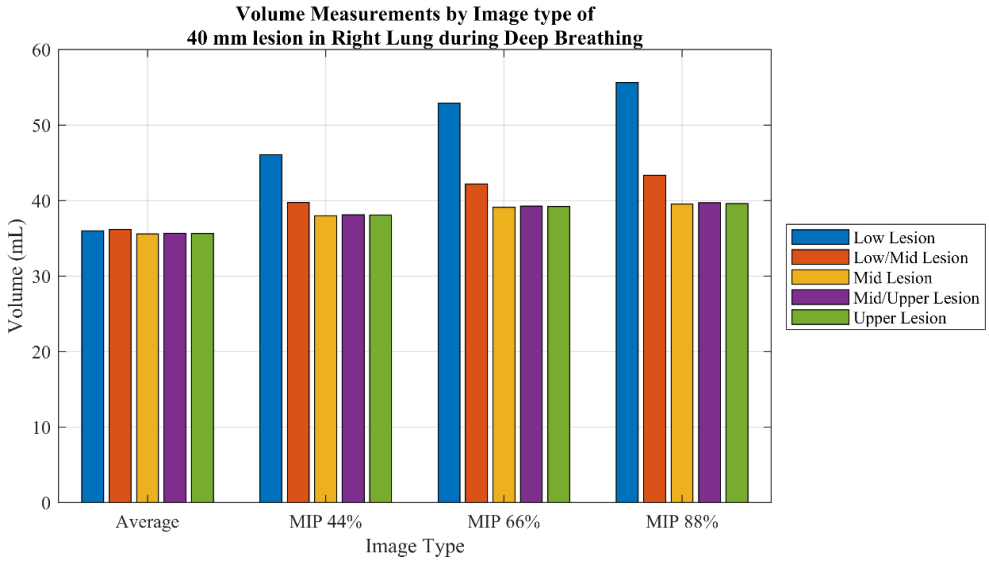

Figure 3.13 Average and MIP image set volume measurements for a 40 mm lesion in the right lung during deep breathing.

Figures 3.14 and 3.15 show average and MIP volume measurements for 50 mm right lung lesions during normal and deep breathing, respectively. Volume differences between lower and upper lung lesions are smaller than for the 40 mm volumes measured above. This aligns with lesion displacement data in the previous section which showed decreased displacement for larger lesions. For example, in the MIP 88% image set, a 40 mm low right lung lesion had a volume 29% larger than a 40 mm mid lung lesion in the same image set. In contrast, only a 23% increase in volume was observed between low and mid 50 mL lesions. During deep breathing, volume increases between low and mid lesions were 41% and 33%% for 40 mm and 50 mm lesions, respectively.

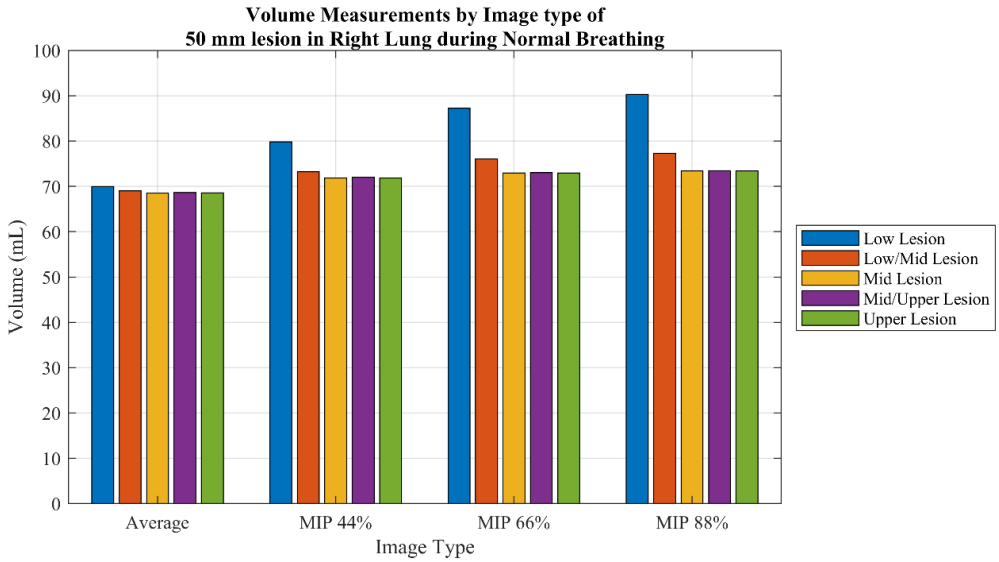

Figure 3.14 Average and MIP image set volume measurements for a 50 mm lesion in the right lung during normal breathing.

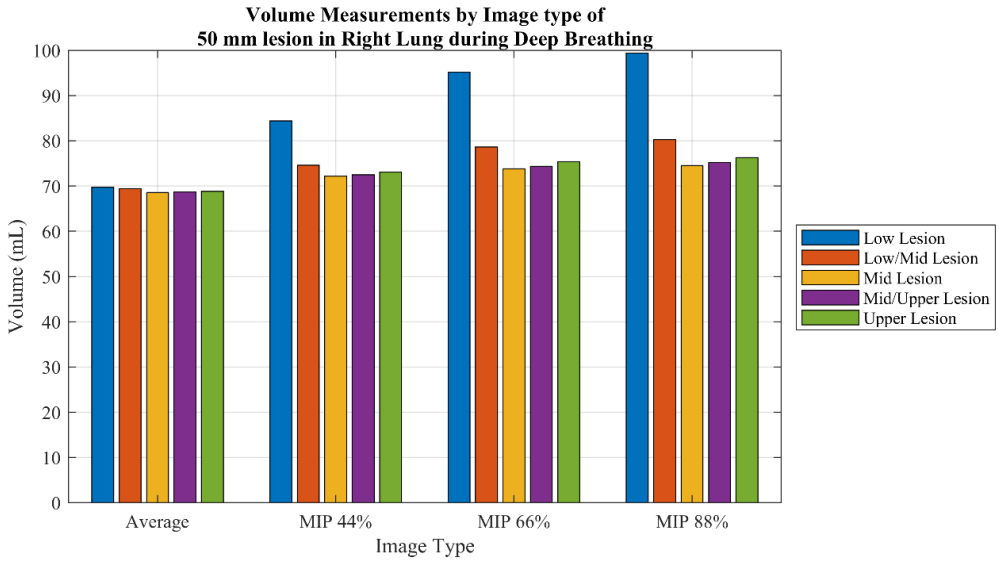

Figure 3.15 Average and MIP image set volume measurements for a 50 mm lesion in the right lung during deep breathing.

Volume measurements for 40 mm left lung lesions are shown in Figures 3.16 and 3.17. The low lesion had the most significant increases in volume during normal breathing and is 30% larger in the MIP 88% than in the average image set. A mid-left lung lesion experienced a volume increase of 9% between average and MIP 88% image

sets. As expected, deep breathing causes further volume increases; here, the low lesion is 7% larger than during normal breathing in the MIP 88% image set. Data for 50 mm left lung lesions is similar to those seen in right lesions and can be found in Appendix B. Overall, apparent lesion volume increases were smaller in the left lung than in the right lung.

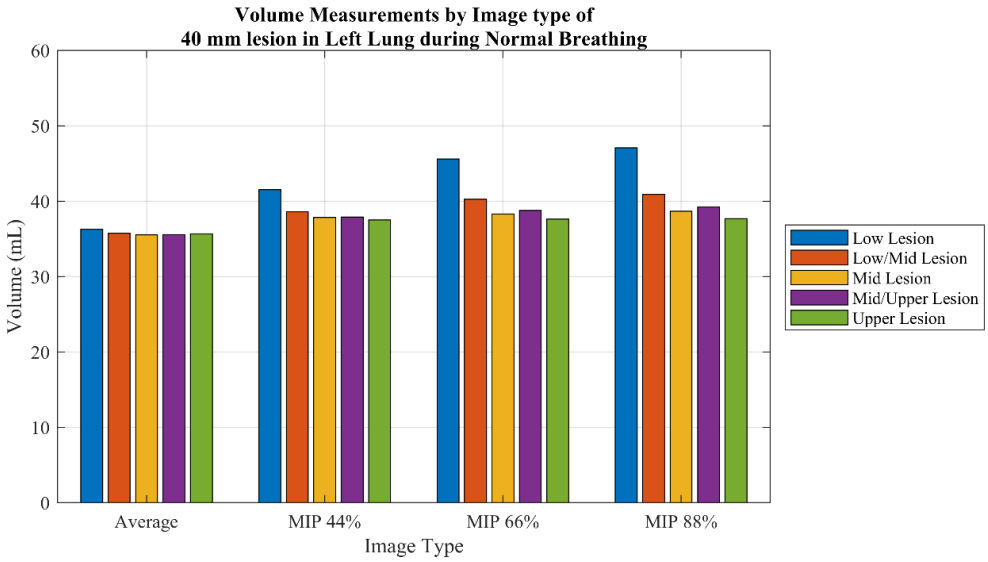

Figure 3.16 Average and MIP image set volume measurements for a 40 mm lesion in the left lung during normal breathing.

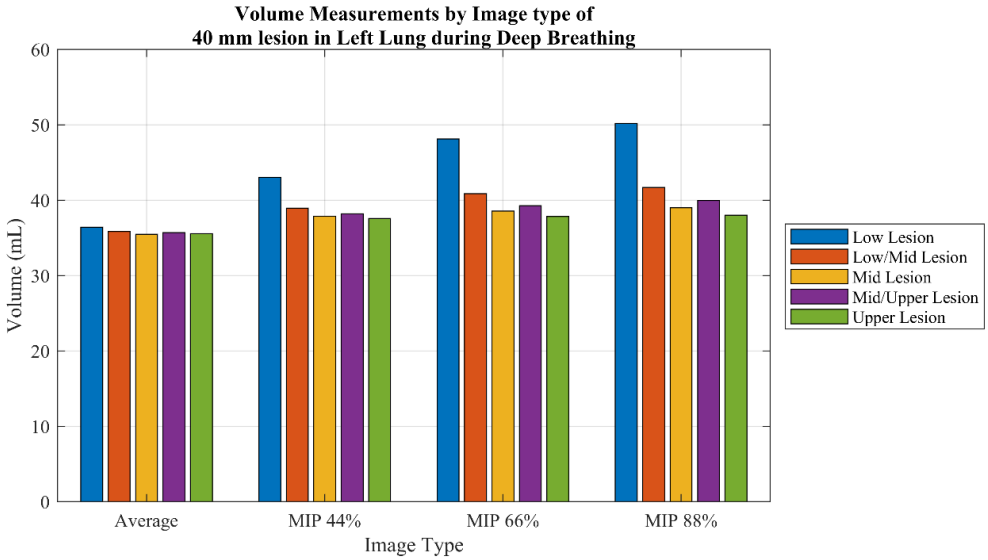

Figure 3.17 Average and MIP image set volume measurements for a 40 mm lesion in the left lung during normal breathing.

Comparison of average and maximum intensity projection image sets generated by the XCAT provide insight into how tumor displacement can cause an increase in the ITV volumes based on tumor location. Since the XCAT represents ideal data from a healthy patient (i.e., is capable of a normal full inhalation), the generation of MIPs at different inhalation phases can suggest potential volume changes of lesions from patients with various conditions based on their breathing capability. For example, if a patient struggles to breathe deeply, they may only reach 44% of their maximum lung capacity. Conversely, for a patient whose tumor does not cause significant breathing detriment and can reach full inhalation relative to the healthy population, their MIP may better reflect the XCAT MIP at 88% inhalation.

3.1.3 XCAT Summary – Translation to Physical Phantoms

The XCAT digital phantom provided an anatomically and kinematically accurate insight into lung lesion displacement during both normal and deep breathing. It allowed for the quantification of lesion displacement in three dimensions and the quantification of lesion volumes in PET and CT images that are key to RT-TP. The SI lesion displacement is highly dependent on the vertical positioning of the lesion in the lung. Lesions in the lower

20% of both the left and right lung are subject to roughly twice as large of displacements in the SI direction compared to lesions in the upper 80% of the lung. AP displacements were more significant in the lower 20% of the lung and had less dependence on vertical positioning in the upper 80%. These maximum displacements could result in a MIP image set showing a volume increase of 55% compared to an average image set if a patient can inhale fully and a volume 66% larger than the known lesion volume. Overall, lesion displacements are most significant in the lower regions of the lung. Lower lesions, therefore, suggest the need for considering larger ITVs in these regions compared with the upper lung.

Proper implementation of PET/CT into radiation treatment of lung cancer requires understanding how volumes determined from PET compare to volumes of interest from 4DCT. If PET and automated segmentation algorithms are used to improve radiation treatment accuracy, lesion volumes from PET images alone must reflect volumes delineated from maximum intensity projections on 4DCT. From the XCAT simulations, 2 cm displacement when simulating lesion movement on PET and 4DCT scanners is sufficient for modelling deep breathing or displacements of small lesions in the lower lung. A moving platform set to oscillate 1 cm can accurately reflect average motion for 40-50 mm lesions.

3.2 CTN Phantom Results

The CTN anthropomorphic phantom underwent PET/CT imaging to study how simulated respiratory motion affects volume determination. After scanning, the image data sets were imported into MIM Maestro. The CTN phantom images for the static and dynamic scans are shown in Figures 3.18 and 3.19, respectively.

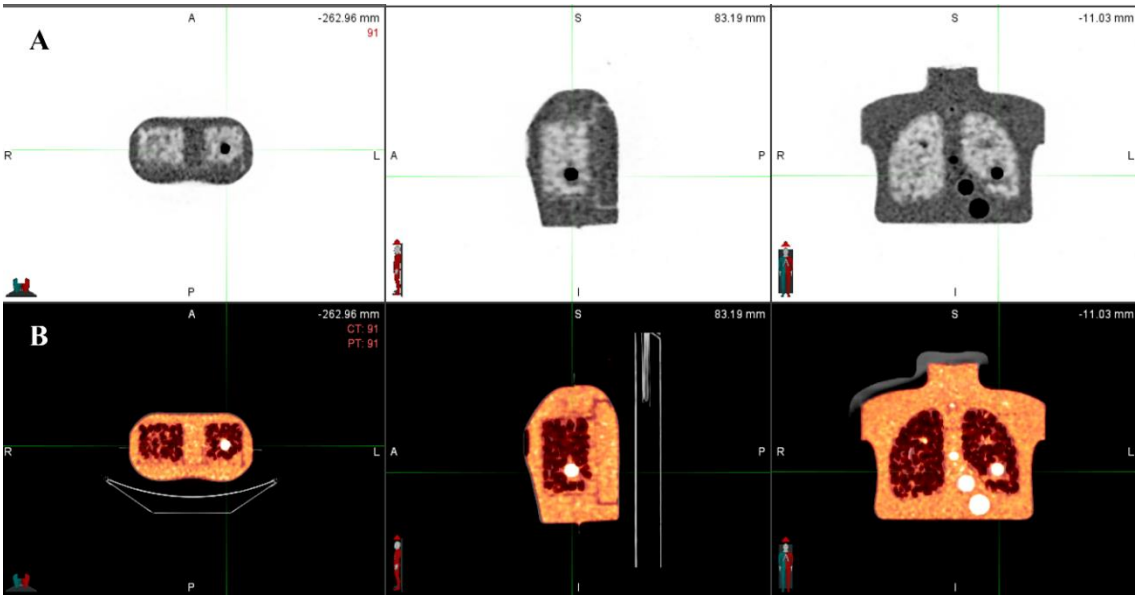

Figure 3.18 Resulting images from static CTN phantom scan showing A) PET and B) PET/CT fused images.

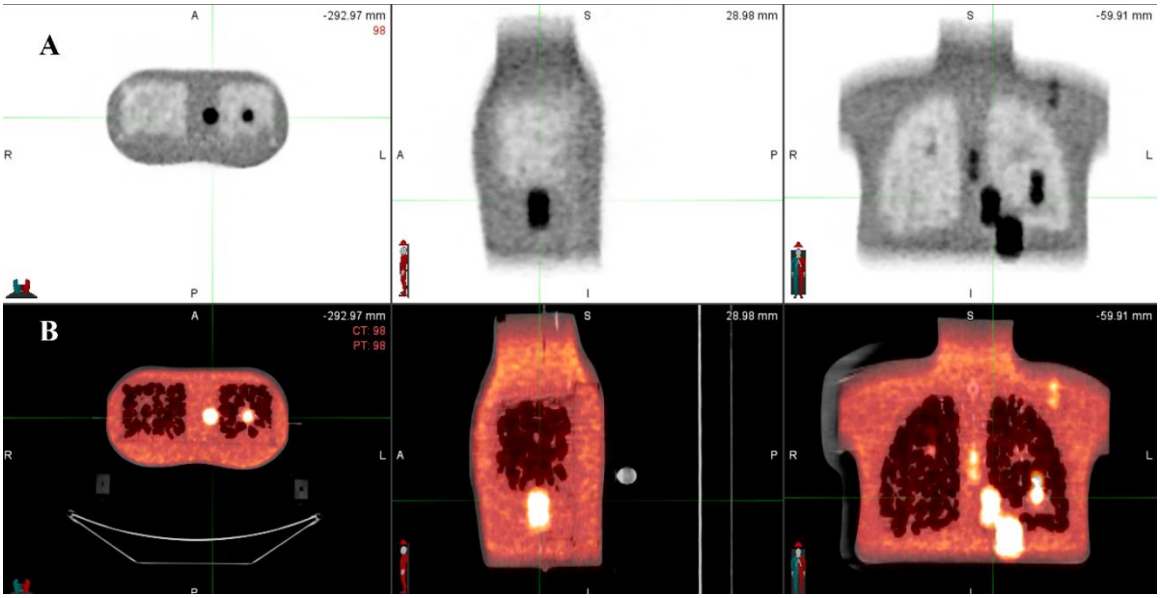

Figure 3.19 Resulting images from dynamic 2 cm CTN phantom scan showing A) PET and B) PET/CT fused images.

Compared to the static images, the dynamic images show considerable blurring of the lesion volumes due to the 2 cm oscillatory motion and lack of gating. Many lesions appear to double in size, while two separate lesions in the abdomen appear to merge. This

blurring is not as apparent in a single slice in the transverse view due to the lack of motion in the AP direction. Figure 3.20 compares the average calculated volumes by image type, static and dynamic motion, with the actual spherical lesion volumes. PET EDGE overestimates the spherical volume for both the static and dynamic scenarios, as seen in Figures 3.20 and 3.21. When a lesion is placed in a heterogeneous environment, motion blurring appears to alter the performance of the ASA. This is clear in the dynamic scenario as the calculated volume is 16% smaller than when the background is homogenous. Here, we define a heterogenous environment as having multiple materials with different attenuation coefficients.

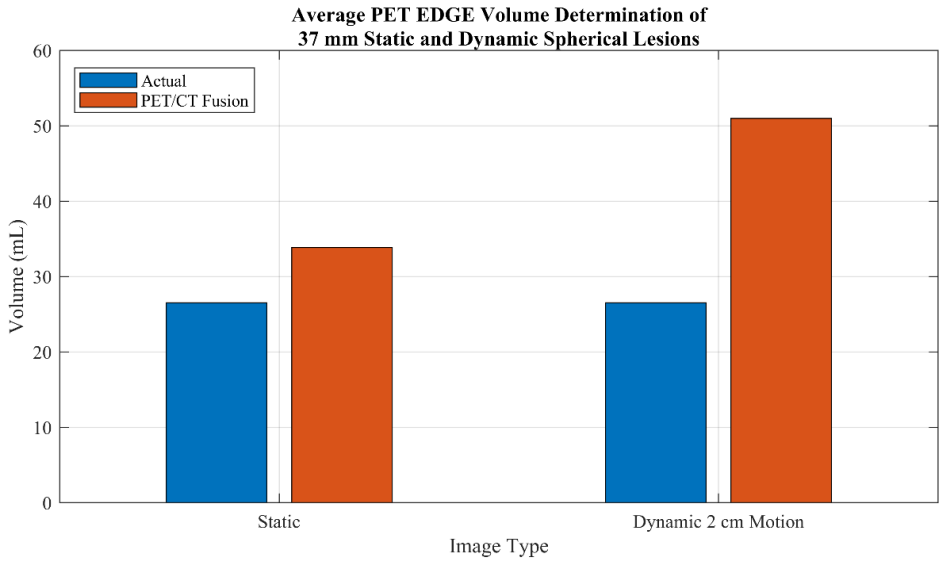

Figure 3.20 Comparison of actual and calculated volumes of a static and dynamic 37 mm spherical lesion using PET EDGE

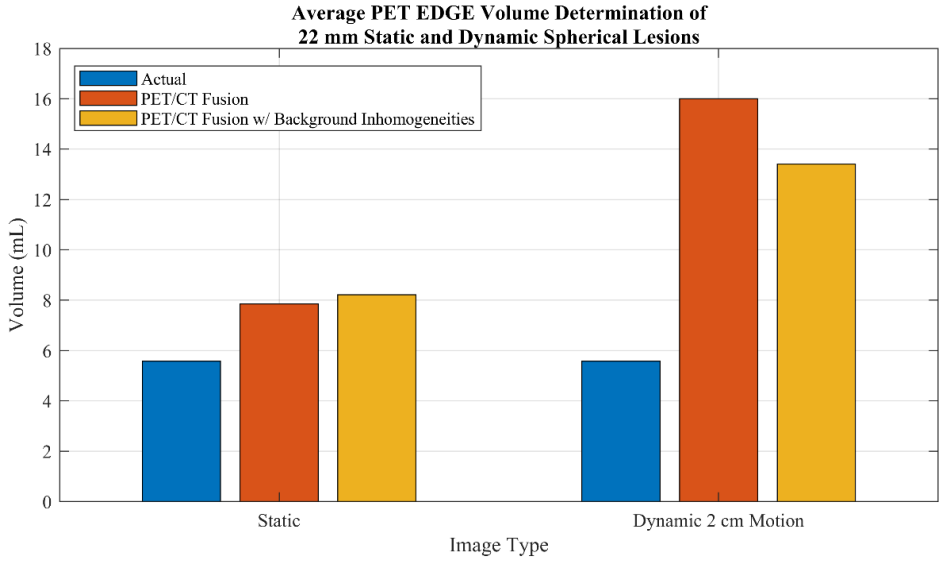

Figure 3.21 Comparison of actual and calculated volumes of a static and dynamic 22 mm spherical lesion using PET EDGE. Background inhomogeneities can be seen in Figures 3.18B and 3.19B in the lung region.

Tables 3.2 summarizes data for the static and dynamic scenarios. Comparisons are made by calculating the percent change between PET EDGE and the known diameter and volumes of the spherical inserts. Clearly, PET EDGE significantly overestimated spherical insert diameters and volumes. Some degree of overestimation is expected due to the increased voxel size and limited spatial resolution of PET compared to CT; nonetheless, these results show poor performance. In the literature, Werner-Wasik *et al.* used sphere phantoms and Monte Carlo PET phantoms of the thorax to evaluate the gradient segmentation technique in MIM. For spheres greater than 20 mm in diameter, PET EDGE overestimated volumes by 4.19%, and overestimated volumes by 8.15% for spheres less than 20 mm in diameter. For digital phantoms, the gradient-based algorithm overestimated volumes by 10.99%. Despite these overestimations, the gradient technique outperformed threshold-based segmentations.[44] A study by Mikell *et al.* compared PET EDGE segmentations of phantoms and patient hepatic tumors to morphological segmentations (MS) completed on CT or MRI. Here, PET EDGE overestimated phantom segmentation volumes by approximately 9% compared to MS but outperformed threshold segmentations. For patient tumors less than 200 cm^3 in volume, PET EDGE also generated volumes larger than those found through MS.[71] Most recently, Fedrigo *et al.*

tested the accuracy of the newer PET EDGE+ gradient segmentation algorithm on ten clinical lymphoma tumors simulated using the XCAT. PET EDGE+ overestimated the total metabolic tumor volume (TMTV) with a percent bias of between 11.9% and 26.3%. The authors suggest that a fixed-edge threshold method was better for delineating TMTV and that PET EDGE+ overestimated tumor volume but was preferable for calculating consistent activity values.[72] Based on these studies, the results presented in this work still show significant overestimation but convey validity in the tendency of PET EDGE to overestimate lesion volumes.

Image Set	**Δ Diameter (vs Actual)**	**Δ Volume (vs Actual)**
37 mm Static	8%	28%
22 mm Static	12%	41%
22 mm Static (w/ background)	14%	46%
37 mm Dynamic	24%	93%
22 mm Dynamic	42%	185%
22 mm Dynamic (w/ background)	34%	139%

Table 3.2 Comparisons between PET EDGE and known diameters and volumes of the spherical inserts.

3.3 Irregular Lesion Results

The 3D-printed irregular lesion underwent 4DCT and PET/CT imaging to quantify the effects of simulated respiratory motion on volume determination and PET EDGE reproducibility. All scans were acquired using the designated 4DCT and PET/CT protocols for lung imaging. The results will be presented in three parts: 4DCT analysis, PET/CT analysis, and fused PET/4DCT analysis.

3.3.1 4DCT Analysis

MIM Maestro was used to analyze the 4DCT images after acquisition. First, ITV contours were created for the external surface of the irregular lesion. External surface contours on MIP image sets were then contracted to create corresponding ITV contours

for the internal surfaces of the lesion. The internal surface contours are shown in Figure 3.22.

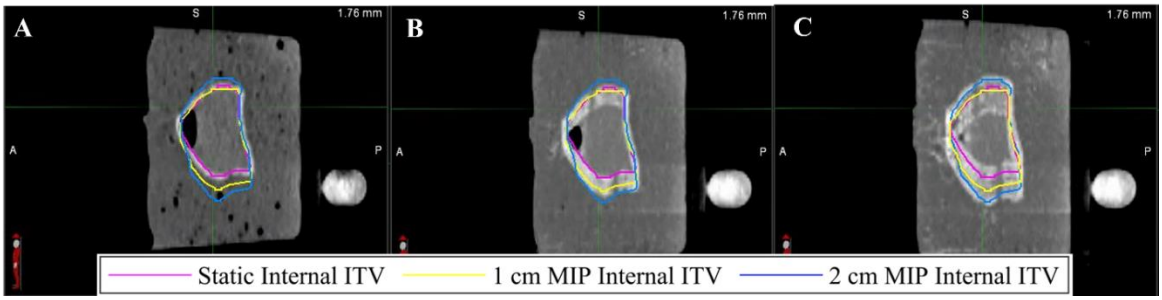

Figure 3.22 Overlay of Static, 1 cm MIP, and 2 cm MIP ITV internal surface contours on A) Static, B) 1 cm MIP, and C) 2 cm MIP scans. Note that an air bubble was in the lesion due to incomplete filling with water.

The corresponding volume calculations for each of the above contours are displayed in Figure 3.23. Here, similar trends are observed as with the XCAT and PET/CT phantoms: there is a reasonable agreement between known and static lesion volumes and increasing disparity as respiration progresses or phantom movement is introduced. For internal surfaces, a 1% volume increase is seen between the static ITV and the known volume of 32.0 mL and can be contributed to CT resolution and contouring accuracy. Volumes calculated from 1 cm MIP and 2 cm MIP contours show respective 30% and 56% volume increases compared to the known volume.

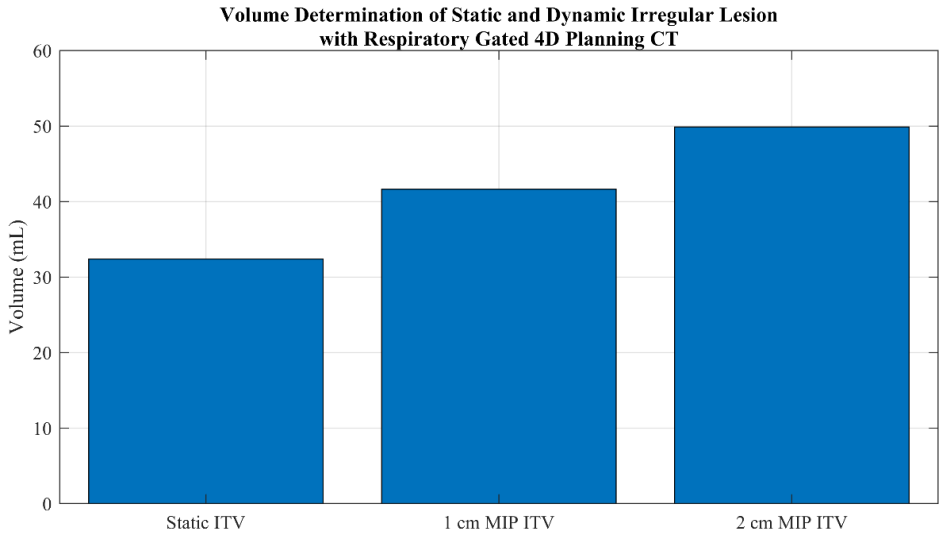

Figure 3.23 Internal volumes of the irregular lesion calculated from ITV contours

While external surface measurements provide additional data points into the effects of motion on ITV segmentation, comparisons between 4DCT and PET require the use of the internal surface volumes only. This is because the volume of radiopharmaceutical used corresponds to the internal volume of the sphere. Additionally, it should be reminded that, based on XCAT findings, 1 cm dynamic motion best corresponds to anthropomorphic lesion displacement, whereas 2 cm motion data findings correspond to cases of deep breathing and lower lung placement of lesions smaller than roughly 40 mm.

3.3.2 PET/CT Analysis

The irregular lesion was filled with 32 mL of 18-FDG solution with an activity of 1.8 MBq before undergoing imaging procedures at SJHH. The resulting scans were then analyzed using the PET EDGE automated segmentation algorithm on MIM Maestro. Figure 3.24 A, B, and C shows resulting lesion segmentations on PET/CT. Note that in Figure 3.24C, an air bubble from the aloe gel appears to merge with the superior surface of the lesion. This likely caused error in the subsequent co-registration with 4DCT. Unlike the 4DCT image, however, there were no observable air bubbles present in the lesion due to precise filling with 18-FDG solution.

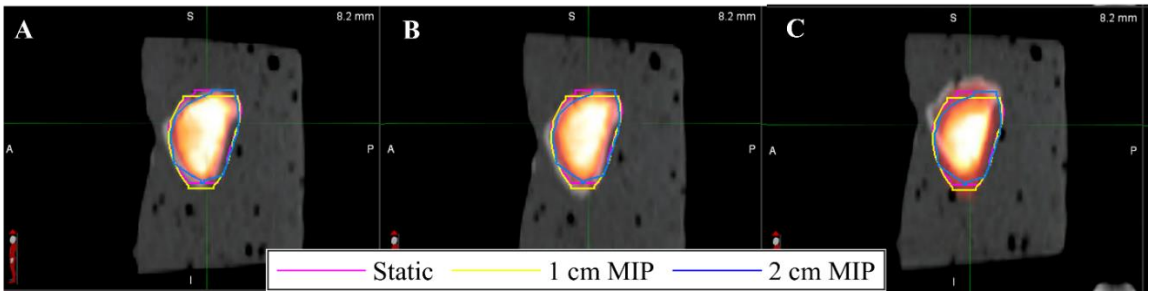

Figure 3.24 Segmentations generated using PET EDGE on A) Static, B) 1 cm dynamic, and C) 2 cm dynamic PET/CT scans.

On each scan, the PET EDGE algorithm was used to create 10 ROIs for volume and reproducibility analysis. Table 3.3 compares the average volume determined from the 10 ROIs on each of the static and dynamic scans to the volume determined from 4DCT. Compared to 4DCT segmentation, the PET EDGE algorithm overestimates volume for the static imaging scenario. Here, the fused PET/CT segmentation was, on average, 42% larger than the 4DCT estimated ITV volume. For the 1 cm dynamic scan it was 11% larger, the 2 cm dynamic scan resulted in a PET EDGE volume that was 12% smaller than the 4DCT ITV.

Image Set	**Δ Volume (PET EDGE vs 4DCT ITV)**
Static	42%
Dynamic 1 cm Motion	11%
Dynamic 2 cm Motion	-12%

Table 3.3 Comparison between volumes calculated from PET EDGE and 4DCT ITV contours for static and dynamic scans.

With 4DCT, the expected increase in internal target volume with increased motion was confirmed and quantified. A noticeable discrepancy between PET and 4DCT findings, however, is the decrease in apparent volume when the PET EDGE algorithm is used to segment a moving lesion. Here, the long acquisition time for PET results in a blurring of radioactive distribution. A region of higher activity is seen in the center of the lesion where the probability of finding radiotracer throughout the respiratory cycle is highest. At either end of the oscillation range of the lesion, the presence of radiotracer is periodic rather than constant and causes blurring around the lesion borders in the final

image set. A smaller volume, therefore, is likely calculated by PET EDGE due to the high SUV gradient between regions of constant and periodic activity. This concept is illustrated in Figure 3.25 and can be seen by comparing Figure 3.24A with Figure 3.24B and C.

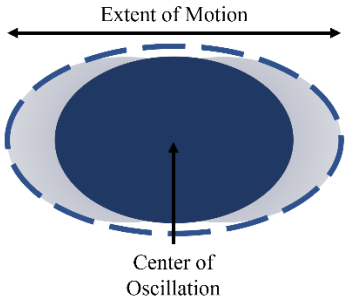

Figure 3.25 Depiction of the motion blurring effect. Darker mass represents the region always populated by lesion mass and shaded regions represent areas affected by the oscillation blurring of the FDG in the lesion.

Despite inaccuracies due to motion artifacts described above, the PET EDGE algorithm showed high reproducibility when calculating volumes. For each of the static and dynamic scans, volume measurements were taken from the 10 ROIs created on the fused PET/CT scans. Figure 3.26 displays this data as a boxplot, where smaller interquartile ranges indicate high reproducibility. As expected, reproducibility is best for static lesions and is reduced as more motion is introduced and the algorithm is further challenged.

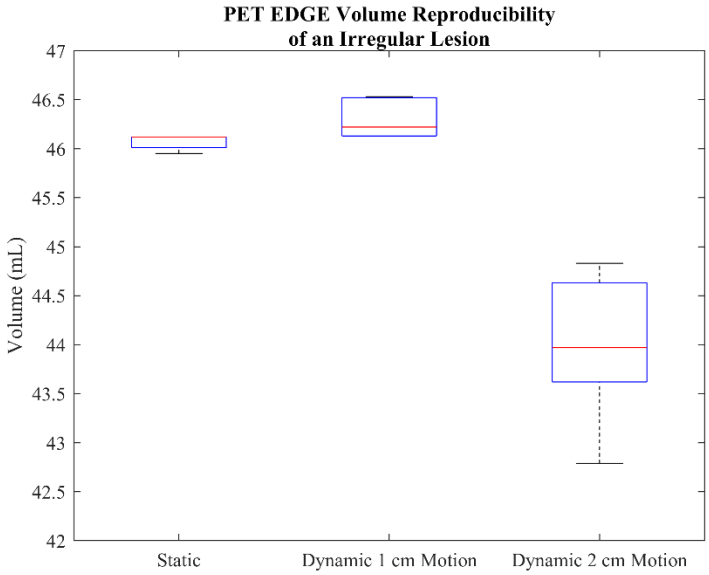

Figure 3.26 Reproducibility of volume calculations using PET EDGE for static and dynamic motion scans

In addition to evaluating the reproducibility of volume determination, the overlap of each of the 10 ROIs was evaluated using Dice similarity coefficients. Reproducibility was highest for the static and 1 cm dynamic motion scenarios, with slightly lower reproducibility for the 2 cm dynamic motion scenario. In combination with the volume reproducibility data, it can be stated that PET EDGE provided highly similar and reproducible contours, however the introduction of movement led to a decrease in expected volume due to the probabilistic nature of an averaged PET image.

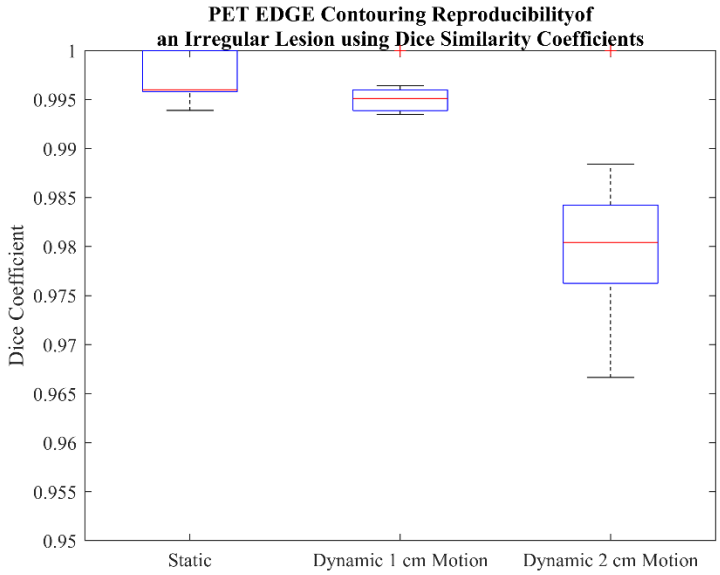

Figure 3.27 Boxplots demonstrating the reproducibility of PET EDGE contouring by measuring Dice coefficient of 10 repeated contours for static and dynamic motion scans

Unpublished data by Cappelletto[73] shows how inter-physician contouring variation can be decreased by providing a computer-generated contour as a starting point. First, segmentations generated using PET EDGE were compared to clinical ITVs generated by radiation oncologists (RO) for 25 patients with lung cancer. DSC values in Figure 3.28 show that overlap between clinical and PET EDGE contours varied from less than 10% to approximately 90%. Two radiation oncologists were then provided with PET EDGE contours and asked to recreate a clinical ITV using the computer-generated contour as a starting point. Similarity between the PET EDGE contour and the adapted contour by the ROs was higher than when no computer-generated contour was provided to them. Comparison between adapted contours from both radiation oncologists show high DSC values, suggesting that providing a computer-generated contour as a starting point can improve contouring reproducibility between clinicians.

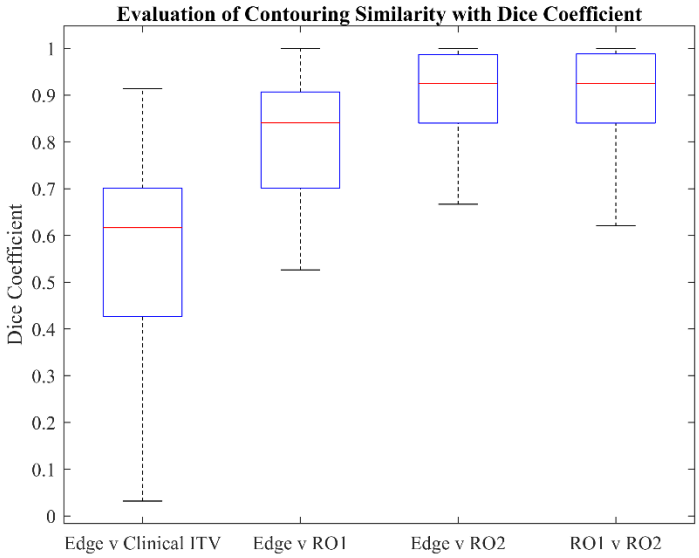

Figure 3.28 Similarity between ITVs generated with and without a PET EDGE contour as a starting point.[73]

3.3.3 Fused PET/4DCT Analysis

PET/CT images were fused to corresponding 4DCT images using two separate methods in MIM: rigid image registration (RIR) and deformable image registration (DIR). Rigid and deformable registrations were completed using the *4D CT – Max IP and Avg IP – Optional Diagnostic PET/CT Registration* workflow in MIM. The PET EDGE algorithm was used to contour the irregularly shaped lesion on the propagated PET images for the static, 1 cm dynamic, and 2 cm dynamic scans. Volumes from PET EDGE segmentations were compared to those generated on 4DCT to determine the accuracy of each segmentation method.

Static

Sample slices of PET and 4DCT fused images are shown in Figure 3.29. Here, the diagnostic CT was first propagated to the planning CT, followed by propagation of PET to the planning CT. The presence of the air bubble is solely from the 4DCT scan and not the PET/CT scan. It is possible that the deformation algorithm attempted to alter the PET distribution to account for changes between the diagnostic and planning CT images as a result of the air bubble; however, locks were implemented using RegRefine® to attempt

to avoid this during the deformation process. Composites generated using RIR appear to align best with the known shape of the irregular lesion as outlined by 4DCT. The image generated through deformable registration shows blurred radioactive distribution outside of the lesion volume.

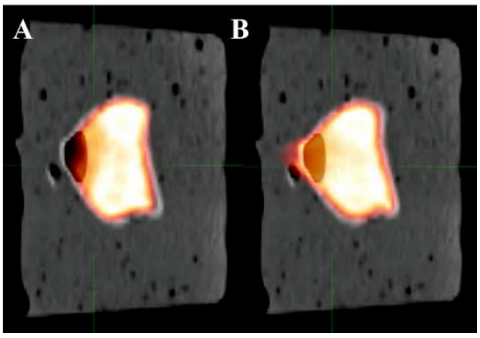

Figure 3.29 Static PET/4DCT images (PET/CT propagated to 4DCT MIP) of an irregular lesion fused using A) rigid image registration and B) deformable image registration

PET EDGE was used to generate ten contours on each of the two fused images. Dice coefficients showed that reproducibility of the ASA was high for both fused images. This metric, however, differs from ITV volume accuracy: a contour can be easily reproduced but not represent a realistic ITV volume. Volumes were calculated on the fused images using PET EDGE and compared to the 4DCT estimated ITV.

Fusion Method	**Δ Volume (PET EDGE vs 4DCT ITV)**
Rigid Image Registration	44%
Deformable Image Registration	52%

Table 3.4 Comparison of static lesion volumes generated from 4DCT and PET EDGE. PET EDGE used on images generated after using rigid and deformable image registration methods.

In addition to accurate volume determination, contours generated by PET must show high overlap with the "gold standard" ITV generated from 4DCT. To measure overlap between PET EDGE and the 4DCT ITV, Dice coefficients were calculated for the ten ITVs in fused PET/4DCT images.

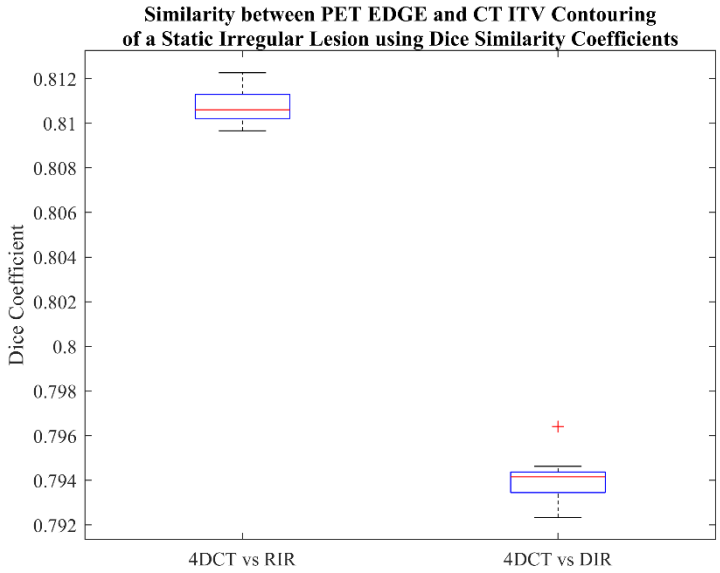

Figure 3.30 Contouring similarity between PET EDGE and 4DCT ITV contours for both fusion methods. The irregular lesion is static during imaging. The red cross represents an outlier value.

1 cm Dynamic Motion

The introduction of 1 cm oscillatory motion during imaging results in increased blurring around the perimeter of the irregular lesion on PET and the appearance of multiple lesion borders on the MIP generated from 4DCT. Due to the short acquisition time of approximately 0.5 seconds for each slice, the diagnostic CT scan appears static. As a result, boundary determination when registering the static image to the blurred MIP from 4DCT is more complex than the static imaging experiment. For instance, rigid and deformable image registration algorithms must extend the volume of the diagnostic CT image to propagate the PET image to the planning CT properly. It is clear from Figure 3.31B that deformable image registration performed poorly compared to RIR when fusing PET with the planning CT. There is significant blurring around the perimeter of the lesion and the general shape of the radioactive distribution is changed. The radioactive distribution in the rigidly registered image appears more uniformly distributed.

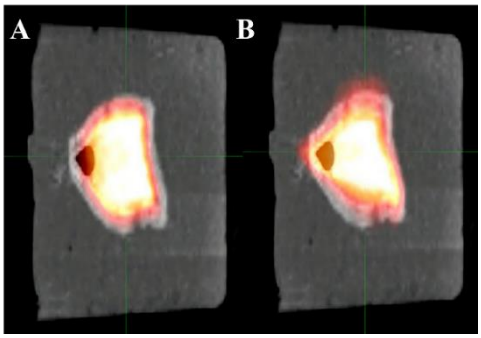

Figure 3.31 PET/4DCT images (PET/CT propagated to 4DCT MIP) of an irregular lesion fused using A) rigid image registration and B) deformable image registration. Lesion oscillated 1 cm during image acquisition.

The blurring of the radioactive distribution resulted in volumes that were in better agreement with the 4DCT ITV. This again suggests that minor image blurring due to respiratory motion is well managed by PET EDGE and may prevent the overestimation of the ITV.

Fusion Method	**Δ Volume (PET EDGE vs 4DCT ITV)**
Rigid Image Registration	11%
Deformable Image Registration	11%

Table 3.5 Comparison of lesion volumes generated from 4DCT and PET EDGE with 1 cm of dynamic motion during image acquisition.

Overlap between 4DCT and PET EDGE contours is improved with 1 cm dynamic motion compared to the static scenario. On average, ASA contours on the rigidly registered image is in 90% agreement with the 4DCT ITV, whereas overlap on the deformably registered image remains at approximately 80%.

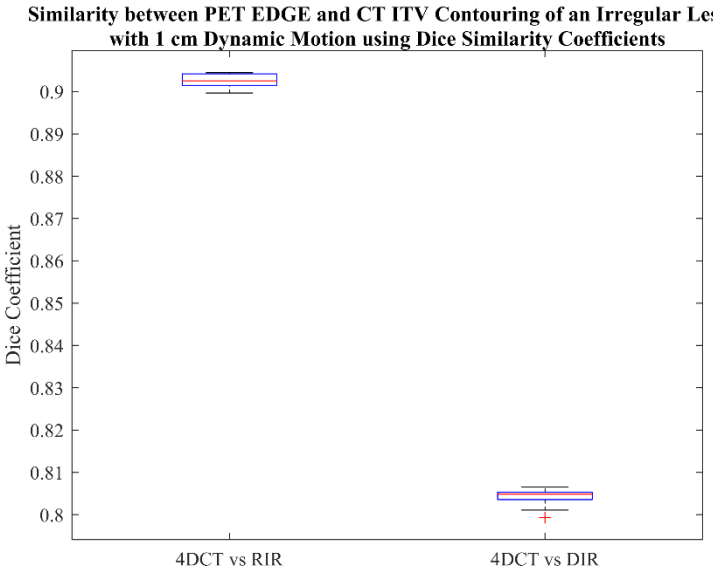

Figure 3.32 Contouring similarity between PET EDGE and 4DCT ITV contours for both fusion methods with 1 cm of dynamic motion during imaging.

2 cm Dynamic Motion

Simulation of deep breathing with 2 cm oscillatory motion resulted in a significant blurring of the radioactive distribution in PET. Challenges noted in the 1 cm dynamic motion discussion, including boundary determination and propagation of the diagnostic CT to planning CT are greater, as illustrated in Figure 3.33. Performance of the deformable image registration algorithm was poor. As a result, both the apparent shape and radiotracer distribution do not reflect the true lesion shape.

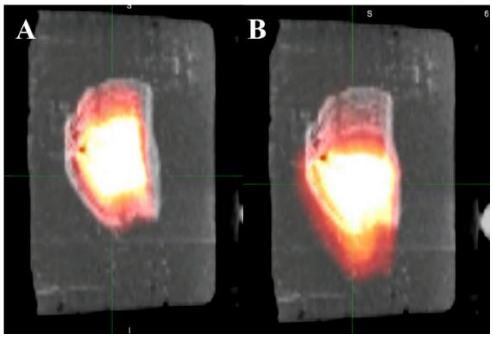

Figure 3.33 PET/4DCT images (PET/CT propagated to 4DCT MIP) of an irregular lesion fused using A) rigid image registration and B) deformable image registration. Lesion oscillated 2 cm during image acquisition.

The 2 cm of oscillatory motion resulted in PET EDGE contours that were smaller than the manually generated 4DCT ITV when images were fused using RIR. This was discussed in Section 3.3.2 on how motion effects the hybrid PET/CT images alone. The segmentation generated on the deformably registered image, however, was 49% larger than the 4DCT ITV. This severe deviation from other trends demonstrates that DIR can be unpredictable and stresses the importance of verifying fused images in a clinical setting.

Fusion Method	**Δ Volume (PET EDGE vs 4DCT ITV)**
Rigid Image Registration	-11%
Deformable Image Registration	49%

Table 3.6 Comparison of lesion volumes generated from 4DCT and PET EDGE for 2 cm of dynamic motion during image acquisition.

PET EDGE contours generated using the rigidly registered image are in 80% agreement with the 4DCT ITV. DIR performance declined significantly, as seen in Figure 3.34.

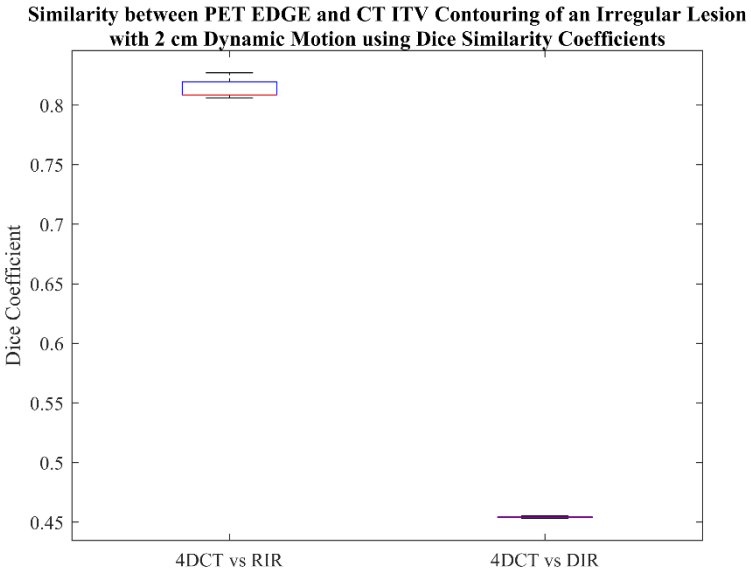

Figure 3.34 Contouring similarity between PET EDGE and 4DCT ITV contours for both fusion methods. Irregular lesion had 2 cm of dynamic motion during imaging.

4 Conclusion

In this work we evaluated methods to improve the integration of PET/CT in radiation treatment planning for lung cancer. First, a 4D XCAT digital anthropomorphic phantom was used to quantify lung lesion displacement caused by respiratory motion. Maximum intensity projections created at various stages of the respiratory cycle showed how ITV estimated volumes change based on lesion location and breathing amplitude. Next, a physical phantom from the Clinical Trials Network was imaged in static and 2 cm of dynamic motion on a moving platform. The resulting images demonstrated the accuracy of the PET EDGE ASA at determining the diameter and volume of known spheres. Finally, a 3D-printed irregularly shaped lesion was created and scanned using 4D planning CT and diagnostic PET/CT protocols for chest imaging. For each modality, a static, 1 cm dynamic, and 2 cm dynamic scans were taken to model lesion displacement from normal and deep breathing, respectively. After separately analyzing 4DCT and diagnostic PET/CT images, the two image sets were fused using rigid and deformable image registration on MIM Maestro. Segmentations generated using PET EDGE were evaluated for reproducibility and accuracy compared to ITVs generated on 4DCT.

XCAT simulations showed that SI displacement of lung lesions was highly dependent on their location within the lung. Lesions placed in the lower 20% of the lung were subject to approximately double the displacement compared to lesions in the upper 80% of the lung. In contrast, AP displacement was less dependent on lesion location. Displacement was highest for lesions in the right lung, and it was demonstrated that in both lungs, 40 mm lesions experienced greater displacement than 50 mm lesions. Volume calculations comparing true lesion volume and internal target volumes show that MIPs generated during deep breathing could result in ITVs 66% larger than the known GTV. Vector displacement calculations were used to determine the amplitude of the moving platform for experiments with the physical phantoms should be set to oscillate 1 cm to simulate displacements during normal breathing and 2 cm to simulate deep breathing.

CTN phantom results established that the PET EDGE algorithm overestimates known volumes during static imaging. With 2 cm dynamic motion, apparent lesion volumes calculated with PET EDGE doubled for the 37 mm lesion and tripled for the 22 mm lesion versus no motion.

The overestimation of internal target volumes generated by PET EDGE was also observed during static imaging of the irregular lesion. On the diagnostic PET/CT, the calculated volume was 44% larger than the ITV determined using 4DCT contouring alone. PET EDGE contour generation after fusion of PET and 4DCT using RIR and DIR resulted in volumes 44%, and 52% larger than the 4DCT ITV. The introduction of 1 cm oscillatory motion during imaging resulted in PET EDGE segmented volumes that were 11% larger than the corresponding 4DCT ITV for all fused images. Deep breathing simulation caused significant motion blurring and resulted in poor registration between PET and 4DCT using DIR and PET EDGE volumes 49% larger than the ITV generated on 4DCT. In contrast, RIR resulted in PET EDGE volumes that were slightly smaller than the 4DCT ITV.

PET EDGE is a highly reproducible, easy-to-use automated segmentation algorithm. Optimization of PET data in the RT planning process for lung cancer may be accomplished if clinicians are first provided with a contour generated automatically on a rigidly fused PET/4DCT image set. It is recommended, however, that clinicians are informed of PET EDGE performance patterns observed in this study: first, lesions located in the middle and upper regions of the lung are likely subject to minimal displacement due to respiratory motion. In these cases, PET EDGE can be expected to overestimate lesion volumes by upwards of 44%. PET EDGE contours generated for lesions in the lower lung, that are often subject to roughly 10 mm of displacement, are most similar to optimal ITVs generated by 4DCT. Finally, for lesions that are displaced more than 20 mm, PET EDGE will begin to underestimate the size of the target volume.

Bibliography

1. Canada S. Release notice - Canadian Cancer Statistics: A 2020 special report on lung cancer. *Heal Promot Chronic Dis Prev Canada*. 2020;40(10):325-325. doi:10.24095/hpcdp.40.10.05

2. Brenner DR, Weir HK, Demers AA, et al. Projected estimates of cancer in Canada in 2020. *Can Med Assoc J*. 2020;192(9):E199-E205. doi:10.1503/cmaj.191292

3. Ellison LF. Progress in net cancer survival in Canada over 20 years. *Heal reports*. 2018;29(9):10-18.

4. Molina JR, Yang P, Cassivi SD, Schild SE, Adjei AA. Non-small cell lung cancer: Epidemiology, risk factors, treatment, and survivorship. *Mayo Clin Proc*. 2008;83(5):584-594. doi:10.4065/83.5.584

5. Lim RJ, Liu B, Krysan K, Dubinett SM. Lung Cancer and Immunity Markers. *Cancer Epidemiol Biomarkers Prev*. 2020;29(12):2423-2430. doi:10.1158/1055-9965.epi-20-0716

6. Goldstraw P, Chansky K, Crowley J, et al. The IASLC lung cancer staging project: Proposals for revision of the TNM stage groupings in the forthcoming (eighth) edition of the TNM Classification for lung cancer. *J Thorac Oncol*. 2016;11(1):39-51. doi:10.1016/j.jtho.2015.09.009

7. Gilroy A, MacPherson B, Schunke M, et al. *Atlas of Anatomy*. 4th ed. Thieme; 2020.

8. Postmus PE, Kerr KM, Oudkerk M, et al. Early and locally advanced non-small-cell lung cancer (NSCLC): ESMO Clinical Practice Guidelines for diagnosis, treatment and follow-up. *Ann Oncol*. 2017;28(Supplement 4):iv1-iv21. doi:10.1093/annonc/mdx222

9. Gelberg J, Grondin S, Tremblay A. Mediastinal staging for lung cancer. *Can Respir J*. 2014;21(3):159-161. doi:10.1155/2014/890108

10. Caldwell CB, Mah K, Ung YC, et al. Observer variation in contouring gross tumor volume in patients with poorly defined non-small-cell lung tumors on CT: The impact of 18FDG-hybrid PET fusion. *Int J Radiat Oncol Biol Phys*. 2001;51(4):923-931. doi:10.1016/S0360-3016(01)01722-9

11. Greco C, Rosenzweig K, Cascini GL, Tamburrini O. Current status of PET/CT for tumour volume definition in radiotherapy treatment planning for non-small cell lung cancer (NSCLC). *Lung Cancer*. 2007;57(2):125-134. doi:10.1016/j.lungcan.2007.03.020

12. Filleron T. Comparing sensitivity and specificity of medical imaging tests when verification bias is present: The concept of relative diagnostic accuracy. *Eur J Radiol*. 2018;98(August 2017):32-35. doi:10.1016/j.ejrad.2017.10.022

13. Howington JA, Blum MG, Chang AC, Balekian AA, Murthy SC. Treatment of stage I and II non-small cell lung cancer: Diagnosis and management of lung cancer, 3rd ed: American college of chest physicians evidence-based clinical practice guidelines. *Chest*. 2013;143(5 SUPPL):e278S-e313S. doi:10.1378/chest.12-2359

14. Burdett S, Parmar M, Stewart L, Souhami R. Postoperative radiotherapy in non-small cell lung cancer: systematic review and meta-analysis of individual patient data from nine randomised controlled trials. *Lancet*. 1998;352.

15. Lemjabbar-Alaoui H, Hassan OUI, Yang YW, Buchanan P. Lung cancer: Biology and treatment options. *Biochim Biophys Acta - Rev Cancer*. 2015;1856(2):189-210. doi:10.1016/j.bbcan.2015.08.002

16. Kaderbhaï CG, Coudert B, Bertaut A, et al. Outcomes of concurrent radiotherapy with weekly docetaxel and platinum-based chemotherapy in stage III non-small-cell lung cancer. *Cancer/Radiotherapie*. 2020;24(4):279-287. doi:10.1016/j.canrad.2019.09.009

17. Ramnath N, Dilling TJ, Harris LJ, et al. Treatment of stage III non-small cell lung cancer: Diagnosis and management of lung cancer, 3rd ed: American college of chest physicians evidence-based clinical practice guidelines. *Chest*. 2013;143(5 SUPPL):e314S-e340S. doi:10.1378/chest.12-2360

18. Socinski MA, Evans T, Gettinger S, et al. Treatment of stage IV non-small cell lung cancer: Diagnosis and management of lung cancer, 3rd ed: American college of chest physicians evidence-based clinical practice guidelines. *Chest*. 2013;143(5 SUPPL):e341S-e368S. doi:10.1378/chest.12-2361

19. Khan F, Gibbons J. *The Physics of Radiation Therapy*. 5th ed. Lippincott Williams & Wilkins; 2014.

20. Johns HE, Cunningham JR. *The Physics of Radiology*. 4th ed. Charles C Thomas; 1983.

21. Zhang Q, Wang X, Sun Q, et al. Investigation and Application of High Megavoltage X-Ray Imaging Mode in Radiotherapy. *Int J Med Physics, Clin Eng Radiat Oncol*. 2016;05(01):42-50. doi:10.4236/ijmpcero.2016.51005

22. Hall EJ, Giaccia AJ. *Radiobiology for the Radiologist*. 7th ed. Lippincott Williams & Wilkins; 2012.

23. Ichiji K, Homma N, Sakai M, Abe M. A Respiratory Motion Prediction Based on Time-Variant Seasonal Autoregressive Model for Real-Time Image-Guided Radiotherapy. In: *Frontiers in Radiation Oncology*. ; 2013.

24. Song Y, Huang X, Mueller B, Mychalczak B. Phase impact factor: a novel parameter for determining optimal CT phase in 4D radiation therapy treatment planning for mobile lung cancer. In: *Medical Imaging 2008: Visualization, Image-Guided Procedures, and Modeling,*. Vol 6918. Proceedings of SPIE; 2008:69181D. doi:10.1117/12.770968

25. El Naqa I, Spencer SJ, Almiron Bonnin D, Deasy JO, Bradley JD. Bioinformatics methods for learning radiation-induced lung inflammation from heterogeneous retrospective and prospective data. *J Biomed Biotechnol*. 2009;2009. doi:10.1155/2009/892863

26. Machtay M, Bae K, Movsas B, et al. Higher Biologically Effective Dose of Radiotherapy is Associated with Improved Ooutcomes for Locally Advanced Non – Small Cell Lung Carcinoma Treated with Chemoradiation : An Analysis of the Radiation Therapy Oncology Group. *Int J Radiat Oncol Biol Phys*. 2012;82(1):425-434. doi:10.1016/j.ijrobp.2010.09.004

27. Keall PJ, Mageras GS, Balter JM, et al. *The Management of Respiratory Motion in Radiation Oncology Report of AAPM Task Group 76*. Vol 33.; 2006. doi:10.1118/1.2349696

28. Bettinardi V, Picchio M, Di Muzio N, Gilardi MC. Motion management in positron emission tomography/computed tomography for radiation treatment planning. *Semin Nucl Med*. 2012;42(5):289-307. doi:10.1053/j.semnuclmed.2012.04.001

29. Duan J, Shen S, Fiveash JB, Brezovich IA, Popple RA, Pareek PN. Dosimetric effect of

respiration-gated beam on IMRT delivery. *Med Phys*. 2003;30(8). doi:10.1118/1.1592017

30. Rouabhi O, Gross B, Bayouth J, Xia J. The Dosimetric and Temporal Effects of Therapy in Patients With Lung Cancer. *Technol Cancer Res Treat*. 2019;18:1-8. doi:10.1177/1533033818816072

31. Li G, Huang H, Chen Q, et al. Characterization of optical-surface-imaging-based spirometry for respiratory surrogating in radiotherapy. *Med Phys*. 2016;43(3):1348-1360. doi:10.1118/1.4941951

32. Vergalasova I, Cai J. A modern review of the uncertainties in volumetric imaging of respiratory-induced target motion in lung radiotherapy. *Med Phys*. 2020;47(10):e988-e1008. doi:10.1002/mp.14312

33. Brink JA, Heiken JP, Wang G, McEnery KW, Schlueter FJ, Vannier MW. Helical CT: principles and technical considerations. *Radiographics*. 1994;14(4):887-893. doi:10.1148/radiographics.14.4.7938775

34. Hilgers G, Nuver T, Minken A. Helical 4D CT pitch management for the Brilliance CT Big Bore in clinical practice. *J Appl Clin Med Phys*. 2015;16(3):389-398. doi:10.1120/jacmp.v16i3.5111

35. Philips. *Respiratory Motion Management for CT*.; 2013.

36. Moses WW. Fundamental limits of spatial resolution in PET. *Nucl Instruments Methods Phys Res Sect A Accel Spectrometers, Detect Assoc Equip*. 2011;648(SUPPL. 1):S236-S240. doi:10.1016/j.nima.2010.11.092

37. Frood R, Prestwich R, Tsoumpas C, Murray P, Franks K, Scarsbrook A. Effectiveness of Respiratory-gated Positron Emission Tomography/Computed Tomography for Radiotherapy Planning in Patients with Lung Carcinoma – A Systematic Review. *Clin Oncol*. 2018;30(4):225-232. doi:10.1016/j.clon.2018.01.005

38. MacManus M, Nestle U, Rosenzweig KE, et al. Use of PET and PET/CT for Radiation Therapy Planning: IAEA expert report 2006-2007. *Radiother Oncol*. 2009;91(1):85-94. doi:10.1016/j.radonc.2008.11.008

39. Thorwarth D, Beyer T, Boellaard R, et al. Integration der FDG-PET/CT-Bildgebung in die

Planung der externen Strahlentherapie - Technische Aspekte und Empfehlungen zur methodischen Annäherung. *NuklearMedizin*. 2012;51(4):140-153. doi:10.3413/Nukmed-0455-11-12

40. Gill BS, Pai SS, McKenzie S, Beriwal S. Utility of PET for radiotherapy treatment planning. *PET Clin*. 2015;10(4):541-554. doi:10.1016/j.cpet.2015.05.002

41. Bradley J, Thorstad WL, Mutic S, et al. Impact of FDG-PET on radiation therapy volume delineation in non-small-cell lung cancer. *Int J Radiat Oncol Biol Phys*. 2004;59(1):78-86. doi:10.1016/j.ijrobp.2003.10.044

42. Spratt DE, Diaz R, McElmurray J, et al. Impact of FDG PET/CT on delineation of the gross tumor volume for radiation planning in non-small-cell lung cancer. *Clin Nucl Med*. 2010;35(4):237-243. doi:10.1097/RLU.0b013e3181d18eb0

43. Faria SL, Menard S, Devic S, et al. Impact of FDG-PET/CT on Radiotherapy Volume Delineation in Non-Small-Cell Lung Cancer and Correlation of Imaging Stage With Pathologic Findings. *Int J Radiat Oncol Biol Phys*. 2008;70(4):1035-1038. doi:10.1016/j.ijrobp.2007.07.2379

44. Werner-Wasik M, Nelson AD, Choi W, et al. What is the best way to contour lung tumors on PET scans? Multiobserver validation of a gradient-based method using a NSCLC digital PET phantom. *Int J Radiat Oncol Biol Phys*. 2012;82(3):1164-1171. doi:10.1016/j.ijrobp.2010.12.055

45. Hatt M, Lee JA, Schmidtlein CR, Lu W, Jeraj R. Classification and evaluation strategies of auto-segmentation approaches for PET : Report of AAPM task group No . 211.

46. Sridhar P, Mercier G, Tan J, Truong MT, Daly B, Subramaniam RM. FDG PET metabolic tumor volume segmentation and pathologic volume of primary human solid tumors. *Am J Roentgenol*. 2014;202(5):1114-1119. doi:10.2214/AJR.13.11456

47. Al-Mayah A, Moseley J, Velec M, Hunter S, Brock K. Deformable image registration of heterogeneous human lung incorporating the bronchial tree. *Med Phys*. 2010;37(9):4560-4571. doi:10.1118/1.3471020

48. Fortin D, Basran PS, Berrang T, Peterson D, Wai ES. Deformable versus rigid registration

of PET/CT images for radiation treatment planning of head and neck and lung cancer patients: A retrospective dosimetric comparison. *Radiat Oncol*. 2014;9(1):1-7. doi:10.1186/1748-717X-9-50

49. Brock KK, Mutic S, McNutt TR, Li H, Kessler ML. Use of image registration and fusion algorithms and techniques in radiotherapy: Report of the AAPM Radiation Therapy Committee Task Group No. 132: Report. *Med Phys*. 2017;44(7):e43-e76. doi:10.1002/mp.12256

50. Sunderland JJ, Christian PE. Quantitative PET/CT scanner performance characterization based upon the society of nuclear medicine and molecular imaging clinical trials network oncology clinical simulator phantom. *J Nucl Med*. 2015;56(1):145-152. doi:10.2967/jnumed.114.148056

51. Xu XG. An exponential growth of computational phantom research in radiation protection, imaging, and radiotherapy: A review of the fifty-year history. *Phys Med Biol*. 2014;59(18). doi:10.1088/0031-9155/59/18/R233

52. Caon M. Voxel-based computational models of real human anatomy: A review. *Radiat Environ Biophys*. 2004;42(4):229-235. doi:10.1007/s00411-003-0221-8

53. Segars WP, Sturgeon G, Mendonca S, Grimes J, Tsui BMW. 4D XCAT phantom for multimodality imaging research. *Med Phys*. 2010;37(9):4902-4915. doi:10.1118/1.3480985

54. *ICRP Publication 89 Basic Anatomical and Physiological Data for Use in Radiological Protection: Reference Values*. Vol 32.; 2002.

55. Segars WP, Lalush DS, Tsui BMW. Modeling respiratory mechanics in the MCAT and spline-based MCAT phantoms. *IEEE Trans Nucl Sci*. 2001;48(1 I):89-97. doi:10.1109/23.910837

56. Segars WP, Mori S, Chen GTY, Tsui BMW. Modeling respiratory motion variations in the 4D NCAT phantom. *IEEE Nucl Sci Symp Conf Rec*. 2007;4:2677-2679. doi:10.1109/NSSMIC.2007.4436697

57. Liao AH, Chuang HC, Shih MC, et al. Development of an in vitro diaphragm motion

reproduction system. *Phys Medica*. 2017;39:39-49. doi:10.1016/j.ejmp.2017.06.017

58. Abràmoff MD, Magalhães PJ, Ram SJ. Image processing with imageJ. *Biophotonics Int*. 2004;11(7):36-41. doi:10.1201/9781420005615.ax4

59. Liu HH, Balter P, Tutt T, et al. Assessing Respiration-Induced Tumor Motion and Internal Target Volume Using Four-Dimensional Computed Tomography for Radiotherapy of Lung Cancer. *Int J Radiat Oncol Biol Phys*. 2007;68(2):531-540. doi:10.1016/j.ijrobp.2006.12.066

60. Loening AM, Gambhir SS. AMIDE: A Free Software Tool for Multimodality Medical Image Analysis. *Mol Imaging*. 2003;2(3):131-137. doi:10.1162/153535003322556877

61. Sunderland JJ. Clinical Trials Network Launching PET Phantom Program for Compliance with New Joint Commission Requirements. *Pathways Clin Trials Netw Newsl*. 2018;(June):1-2.

62. Hess R. *Blender Foundations*. Elsevier; 2010.

63. Maes F, Collignon A, Vandermeulen D, Marchal G, Suetens P. Multimodality Image Registration by Maximization of Mutual Information. *IEEE Trans Med Imaging*. 1997;16(2):187-198.

64. MIM Maestro® User Guide. *MIM Softw Inc*. Published online 2020.

65. Piper J, Nelson A, Harper J. Deformable Image Registration in MIM Maestro ® Evaluation and Description. *MIM Softw Inc White Pap*. Published online 2013.

66. Johnson PB, Padgett KR, Chen KL, Dogan N. Evaluation of the tool “Reg Refine” for user-guided deformable image registration. *J Appl Clin Med Phys*. 2016;17(3):158-170. doi:10.1120/jacmp.v17i3.6025

67. Geramifar P, Zafarghandi MS, Ghafarian P, Rahmim A, Ay MR. Respiratory-induced errors in tumor quantification and delineation in ct attenuation-corrected PET images: Effects of tumor size, tumor location, and respiratory trace: A simulation study using the 4D XCAT phantom. *Mol Imaging Biol*. 2013;15(6):655-665. doi:10.1007/s11307-013-0656-5

68. Seppenwoolde Y, Shirato H, Kei Kitamura, et al. Precise and Real-Time Measurement of 3D Tumor Motion in Lung Due to Breathing and Heartbeat, Measured During Radiotherapy. *Int J Radiat Oncol Biol Phys*. 2002;53(4):822-834.

69. Ekberg L, Holmberg O, Wittgren L, Bjelkengren G, Landberg T. What margins should be added to the clinical target volume in radiotherapy treatment planning for lung cancer? *Radiother Oncol*. 1998;48(1):71-77. doi:10.1016/S0167-8140(98)00046-2

70. Erridge SC, Seppenwoolde Y, Muller SH, et al. Portal imaging to assess set-up errors, tumor motion and tumor shrinkage during conformal radiotherapy of non-small cell lung cancer. *Radiother Oncol*. 2003;66(1):75-85. doi:10.1016/S0167-8140(02)00287-6

71. Mikell JK, Kaza RK, Roberson PL, et al. Impact of 90 Y PET gradient-based tumor segmentation on voxel-level dosimetry in liver radioembolization. *EJNMMI Phys*. 2018;5(1). doi:10.1186/s40658-018-0230-y

72. Fedrigo R, Martineau P, Segars P, et al. Evaluation of Threshold and Gradient-Based PET Segmentation Algorithms using New Anthropomorphic XCAT Phantom with Scalable Lymphatic System: Application to Nodal Non-Hodgkin's Lymphoma. *J Nucl Med*. 2021;62(supplement 1):1402 LP - 1402.

73. Cappelletto N, Vlad R. Automated Segmentation of Lung Tumors on Diagnostic PET / CT with Accurate Propagation to the Planning CT.

Appendix A

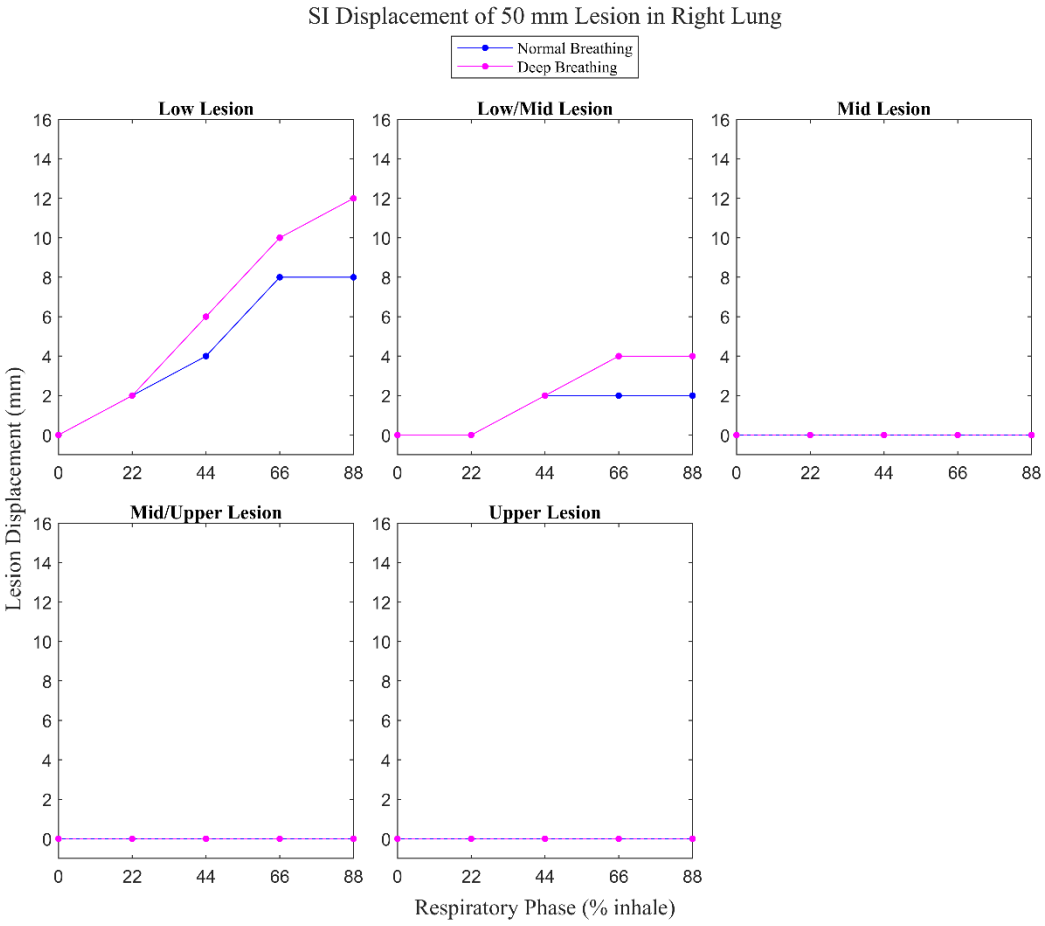

Figure A.1 Plot showing the inferior displacement of a 50 mm lesion from full exhale position in the right lung as a function of the respiratory phase of the phantom. Data is shown for lesions in five separate locations, ranging from lower to upper regions of the lung.

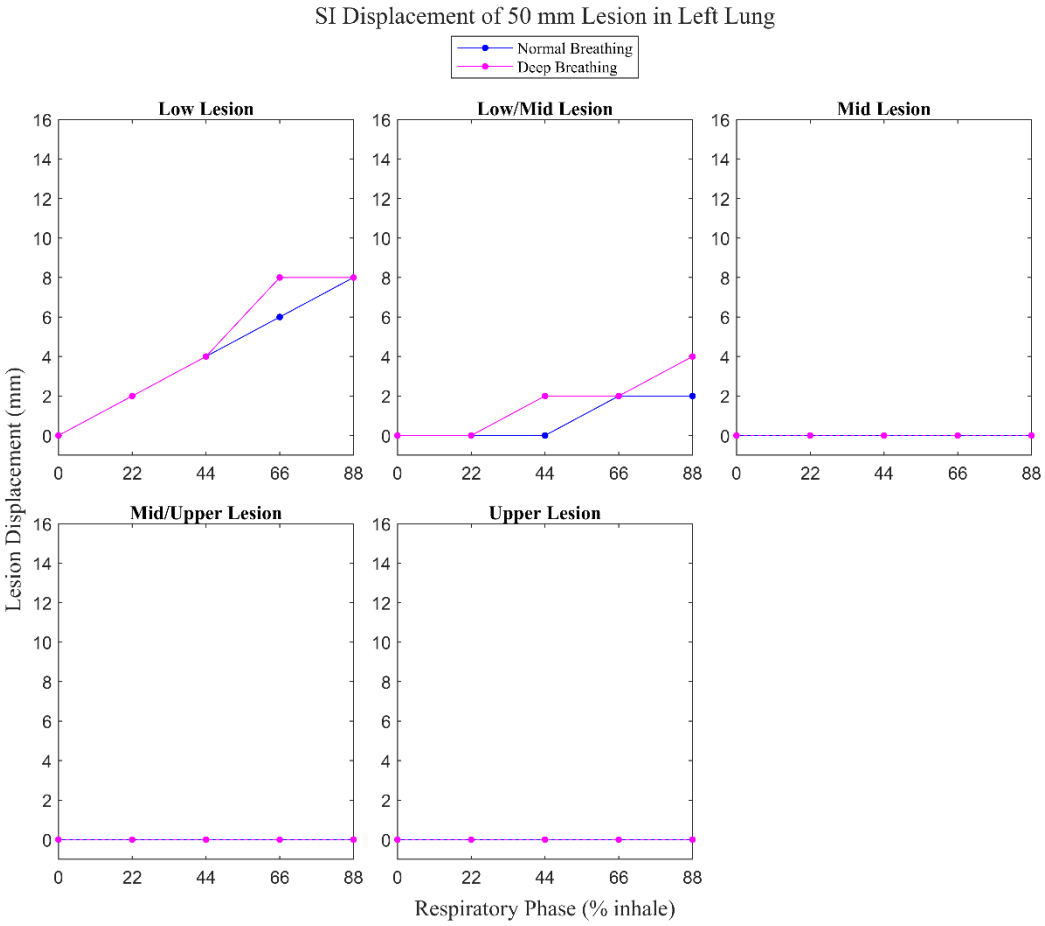

Figure A.2 Plot showing the inferior displacement of a 50 mm lesion from full exhale position in the left lung as a function of the respiratory phase of the phantom. Data is shown for lesions in five separate locations, ranging from lower to upper regions of the lung.

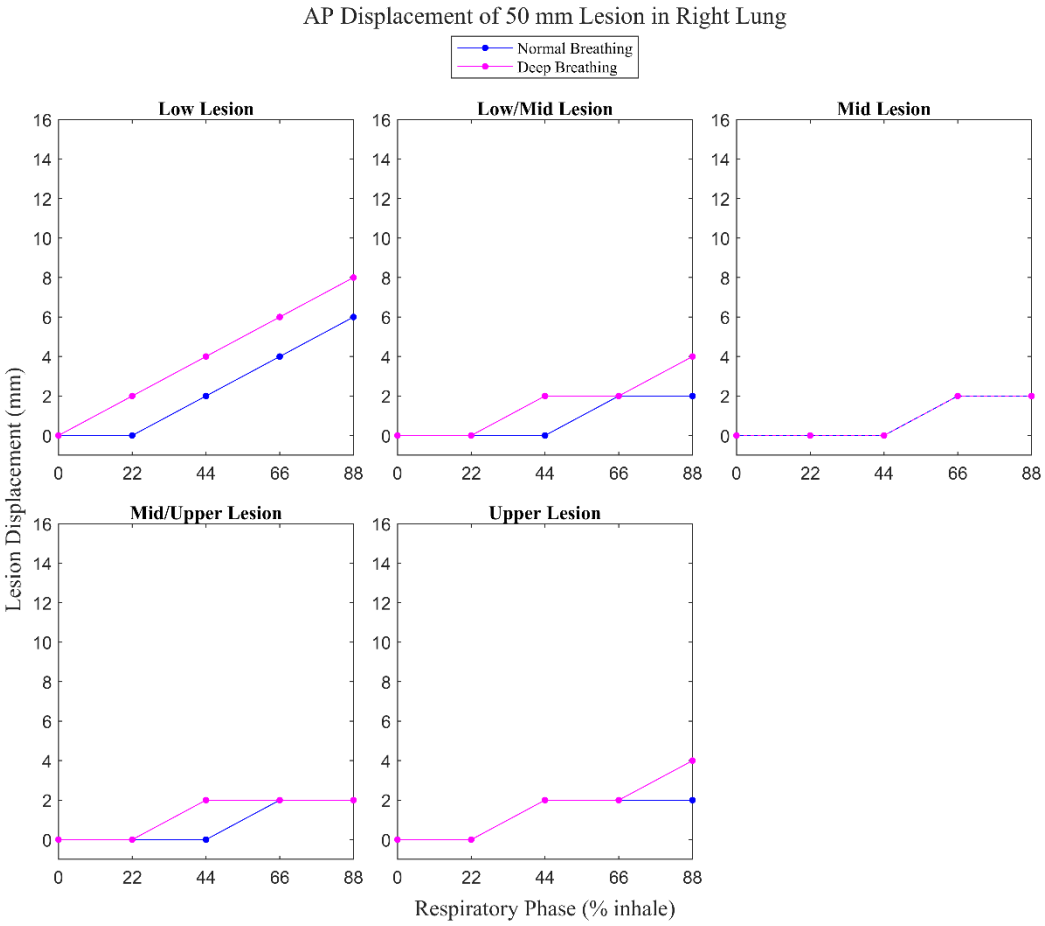

Figure A.3 Plot showing the anterior displacement of a 50 mm lesion from full exhale position in the right lung as a function of the respiratory phase of the phantom. Data is shown for lesions in five separate locations, ranging from lower to upper regions of the lung.

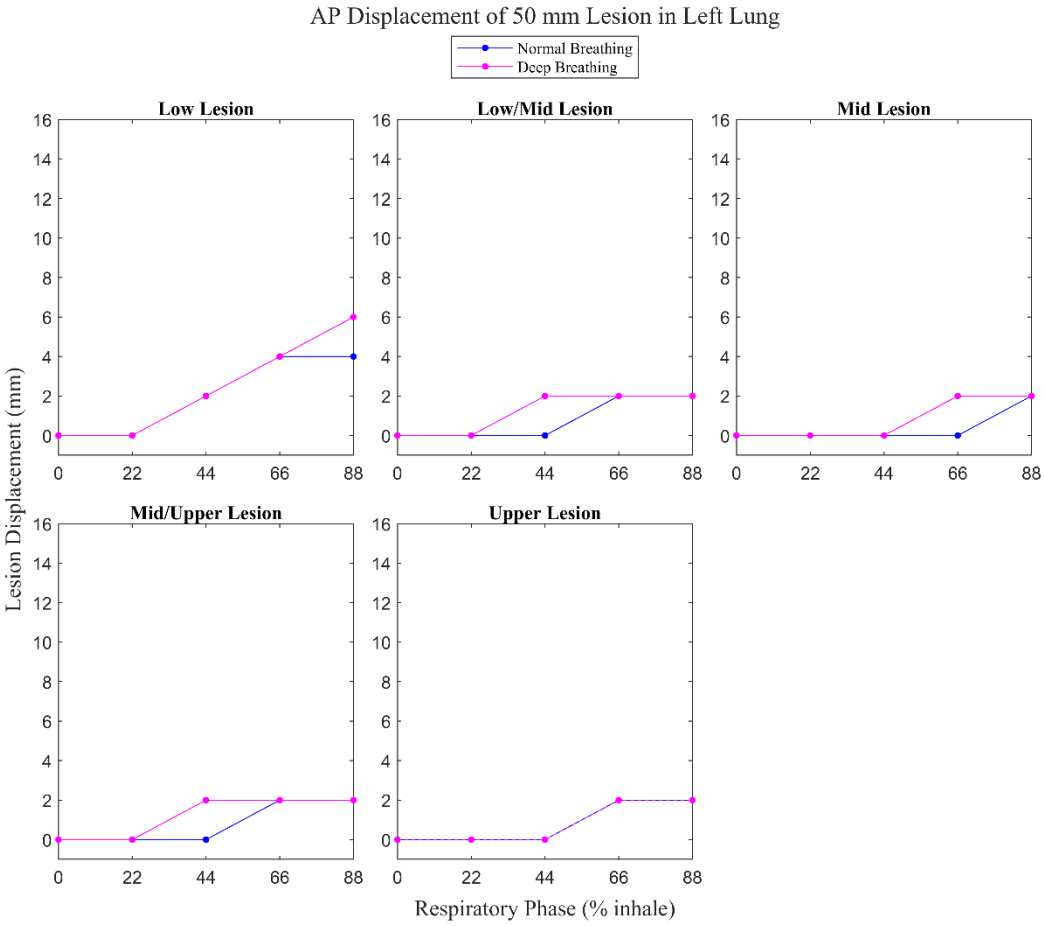

Figure A.4 Plot showing the anterior displacement of a 50 mm lesion from full exhale position in the left lung as a function of the respiratory phase of the phantom. Data is shown for lesions in five separate locations, ranging from lower to upper regions of the lung.

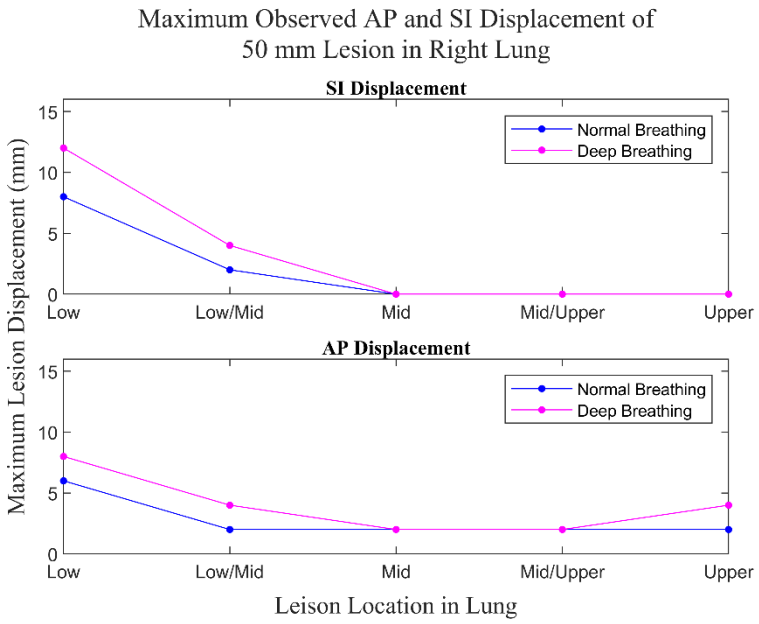

Figure A.5 Maximum displacement observed in the SI and AP directions of 50 mm lesions across five different locations in the right lung.

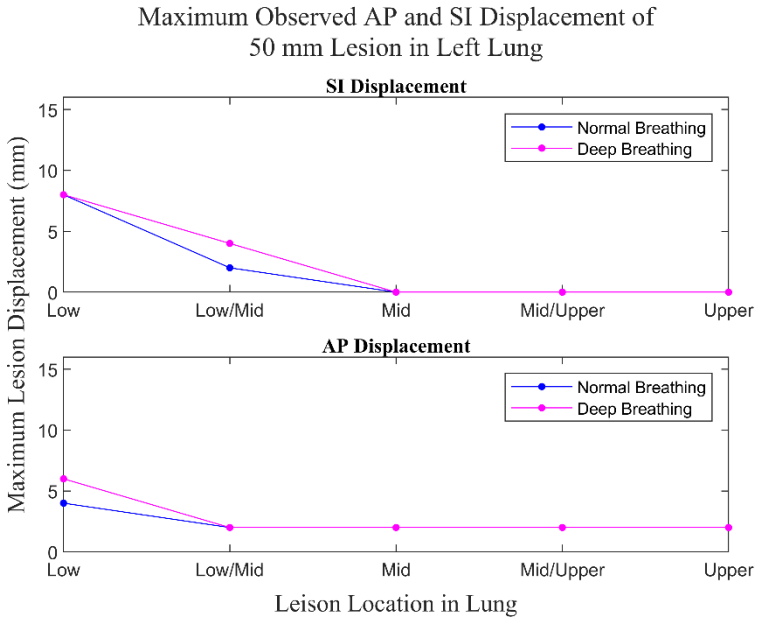

Figure A.6 Maximum displacement observed in the SI and AP directions of 50 mm lesions across five different locations in the left lung

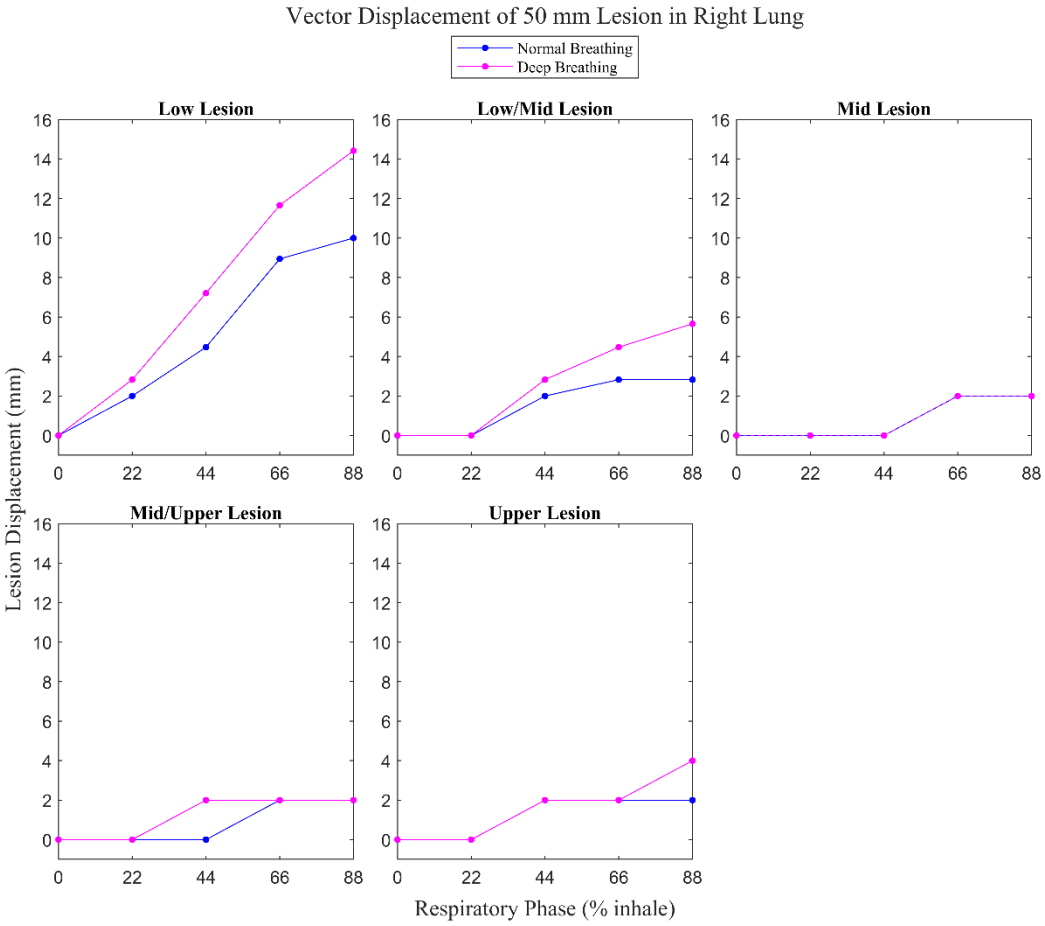

Figure A.7 Vector displacements of 50 mm lesions in the right lung as a function of respiratory phase.

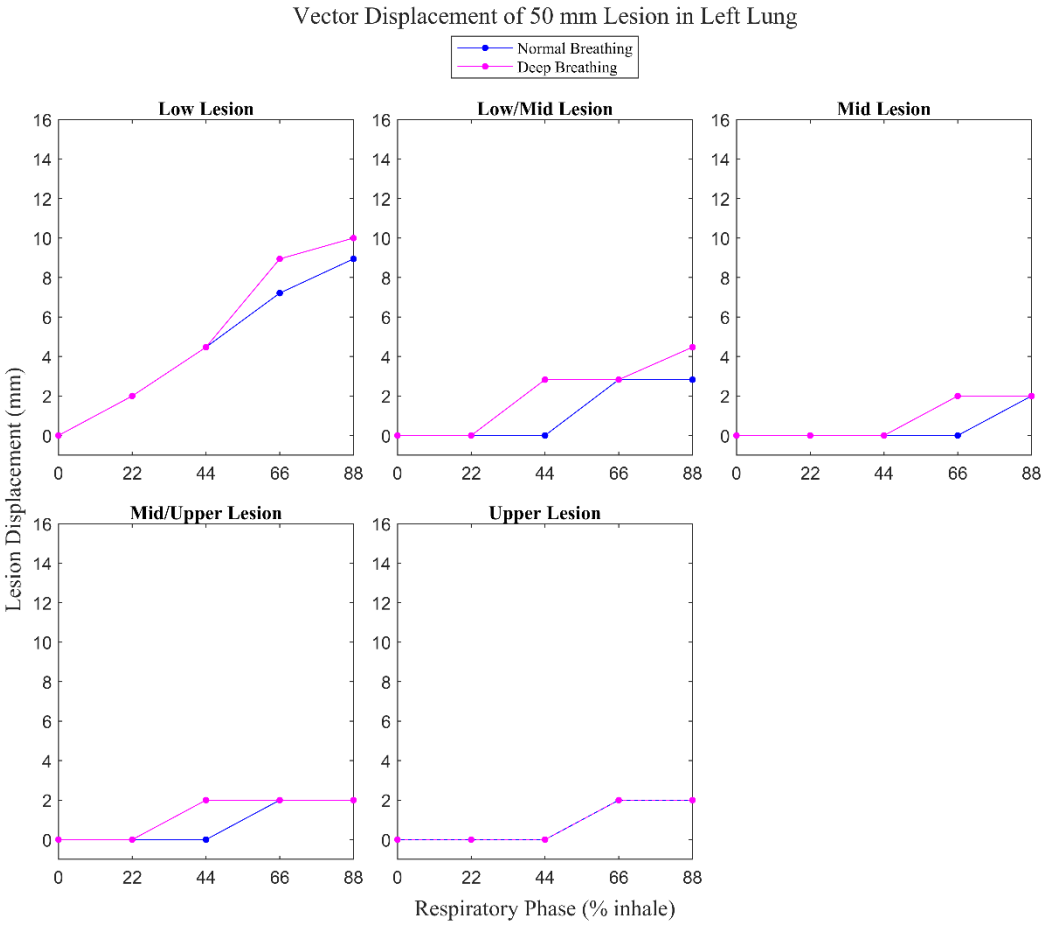

Figure A.8 Vector displacements of 50 mm lesions in the left lung as a function of respiratory phase.

Appendix B

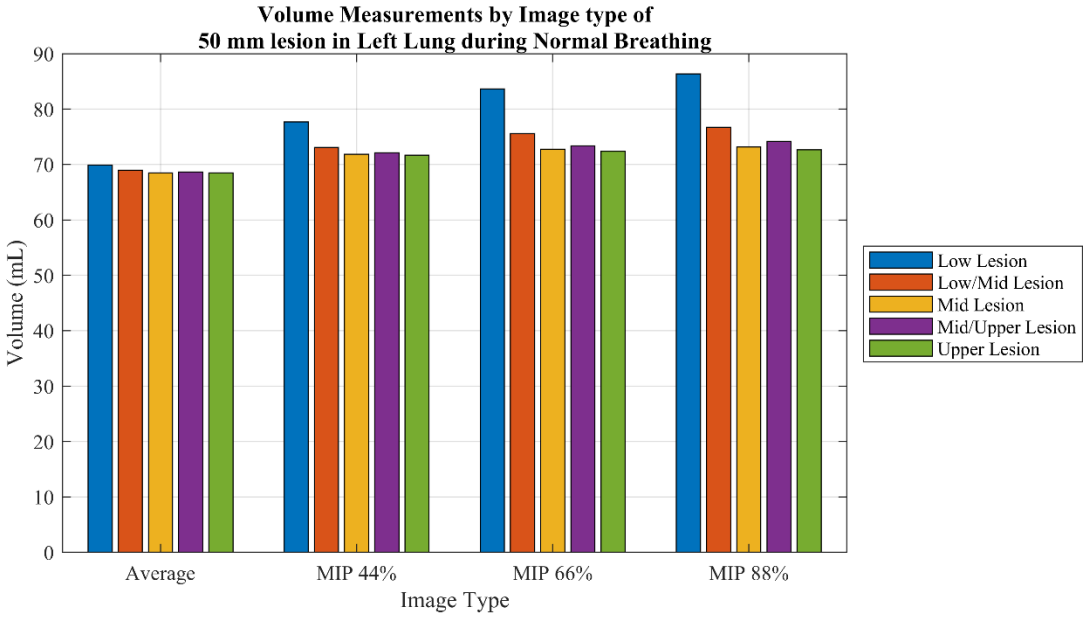

Appendix B.1 Average and MIP image set volume measurements for a 50 mm lesion in the left lung during normal breathing. Each bar represents a different vertical location in the lung.

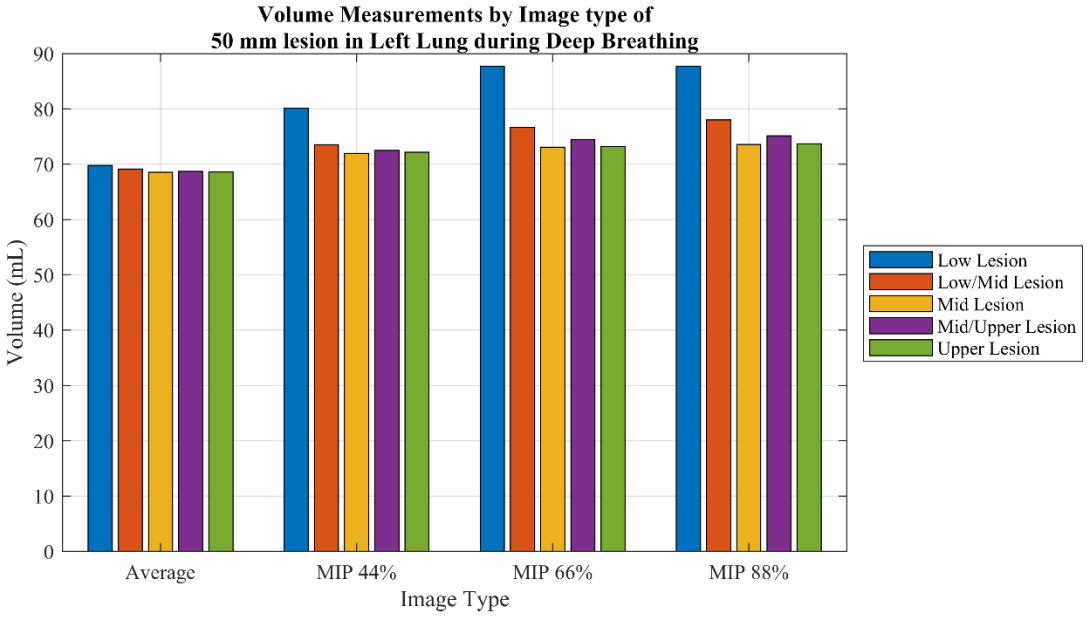

Appendix B.2 MIP image set volume measurements for a 50 mm lesion in the left lung during deep breathing. Each bar represents a different vertical location in the lung.